Stockholm University

Biomass-derived nanoscopic catalysts for water treatment

Structure-property relationship investigation

Jianhong Chen

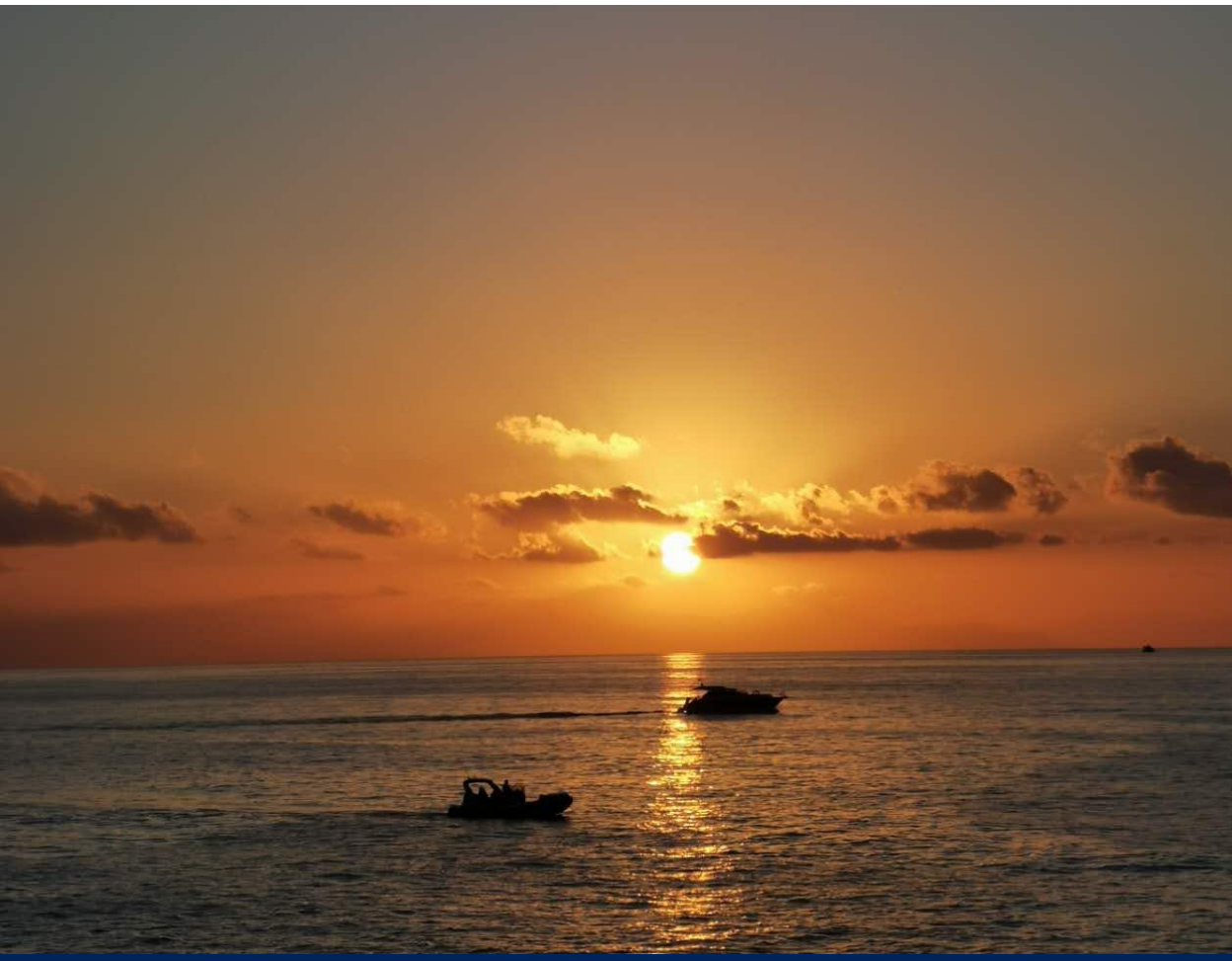

Doctoral Thesis in Inorganic Chemistry at Stockholm University, Sweden 2023

Biomass-derived nanoscopic catalysts for water treatment

Structure-property relationship investigation

Jianhong Chen

Academic dissertation for the Degree of Doctor of Philosophy in Inorganic Chemistry at Stockholm University to be publicly defended on Friday 31 March 2023 at 09.00 in Magnélisalen, Kemiska övningslaboratoriet, Svante Arrhenius väg 16 B Stockholm and digitally via Zoom, public link is available at the department website.

Abstract

Green Chemistry has received widespread interest due to its capacity to meet environmental and economic objectives. The Twelve Principles were proposed to better perform Green Chemistry and have become the guideline for solving many environmental issues. Water contamination has become a major global challenge in the 21st century. Millions of people die from diseases caused by drinking contaminated water. Nitrate, metal ions and dye are the most frequent contaminants. Nitrate in drinking water, after ingestion, is reduced to nitrite by the gastrointestinal tract and threatens human health. Dye-polluted water is usually nonbiodegradable and poisonous: the main criticism is that it is harmful to human health and hampers the photosynthesis rate of aquatic life. Metal ions generally lead to biological and physiological complications when they bind to cellular macromolecules. Therefore, efficient and eco-friendly purification technology is pressing to provide solutions for water purification.

This thesis is set out to investigate the electro-/photo- catalytical water purification techniques using different catalysts. Efficient nitrate electrochemical reduction was achieved by using NDC materials, and the active sites were determined with the help of a comprehensive solid-state NMR supported by theoretical calculation and DFT calculations. Furthermore, the photochemical dye degradation was performed using cellulose-based hybrid bio-inorganic catalysts. The intentional maintenance of the surface functional groups on cellulose-based materials can promote dye degradation performance and, most importantly, achieve simultaneous removal of heavy metal ions aside from photo dye degradation. Additionally, this thesis proposed two possible synthesis strategies to obtain electro-/photo- catalysts using cellulose-based materials as renewable resources. The Twelve Principles of Green Chemistry guided the optimization of the synthesis route and raw material selectivity. Notably, the low-temperature synthesis of hybrid photocatalysts maintained the surface functional groups and preserved the kinetic mechanism of contaminants' adsorption on bio-substrate. This research is likely to contribute to a deeper understanding of renewable materials with green synthesis methods for catalysts targeting water contamination treatment.

Keywords: *green chemistry, water purification, electrochemistry, photochemistry, biomass material, structure-property relationship.*

Stockholm 2023
http://urn.kb.se/resolve?urn=urn:nbn:se:su:diva-213988

ISBN 978-91-8014-168-0
ISBN 978-91-8014-169-7

Stockholm University

Department of Materials and Environmental Chemistry (MMK)

Stockholm University, 106 91 Stockholm

BIOMASS-DERIVED NANOSCOPIC CATALYSTS FOR WATER TREATMENT

Jianhong Chen

Stockholm
University

Biomass-derived nanoscopic catalysts for water treatment

Structure-property relationship investigation

Jianhong Chen

©Jianhong Chen, Stockholm University 2023

ISBN print 978-91-8014-168-0
ISBN PDF 978-91-8014-169-7

Printed in Sweden by Universitetsservice US-AB, Stockholm 2023

To my family.

"I must not fear. Fear is the mind-killer. Fear is the little-death that brings total obliteration. I will face my fear. I will permit it to pass over me and through me. And when it has gone past I will turn the inner eye to see its path. Where the fear has gone there will be nothing. Only I will remain"

–Frank Herbert, Dune

Abstract

Green Chemistry has received widespread interest due to its capacity to meet environmental and economic objectives. The Twelve Principles were proposed to better perform Green Chemistry and have become the guideline for solving many environmental issues. Water contamination has become a major global challenge in the 21st century. Millions of people die from diseases caused by drinking contaminated water.[1] Nitrate, metal ions and dye are the most frequent contaminants. Nitrate in drinking water, after ingestion, is reduced to nitrite by the gastrointestinal tract and threatens human health.[2,3] Dye-polluted water is usually nonbiodegradable and poisonous: the main criticism is that it is harmful to human health and hampers the photosynthesis rate of aquatic life. Metal ions generally lead to biological and physiological complications when they bind to cellular macromolecules. Therefore, efficient and eco-friendly purification technology is pressing to provide solutions for water purification.

This thesis is set out to investigate the electro-/photo- catalytical water purification techniques using different catalysts. Efficient nitrate electrochemical reduction was achieved by using NDC materials, and the active sites were determined with the help of a comprehensive solid-state NMR supported by theoretical calculation and DFT calculations. Furthermore, the photochemical dye degradation was performed using cellulose-based hybrid bio-inorganic catalysts. The intentional maintenance of the surface functional groups on cellulose-based materials can promote dye degradation performance and, most importantly, achieve simultaneous removal of heavy metal ions aside from photo dye degradation. Additionally, this thesis proposed two possible synthesis strategies to obtain electro-/photo- catalysts using cellulose-based materials as renewable resources. The Twelve Principles of Green Chemistry guided the optimization of the synthesis route and raw material selectivity. Notably, the low-temperature synthesis of hybrid photocatalysts maintained the surface functional groups and preserved the kinetic mechanism of contaminants' adsorption on bio-substrate. This research is likely to contribute to a deeper understanding of renewable materials with green synthesis methods for catalysts targeting water contamination treatment.

Sammanfattning

Green Chemistry har fått ett stort intresse på grund av sin förmåga att uppfylla miljömässiga och ekonomiska mål. De tolv principerna föreslogs för att bättre prestera grön kemi och har blivit riktlinjen för att lösa många miljöfrågor. Vattenförorening har blivit en stor global utmaning under 2000-talet. Miljontals människor dör av sjukdomar orsakade av att dricka förorenat vatten.[1] Nitrat, metalljoner och färgämnen är de vanligaste föroreningarna. Nitrat i dricksvatten, efter intag, reduceras till nitrit av mag-tarmkanalen och hotar människors hälsa.[2,3] Färgämnesförorenat vatten är vanligtvis icke biologiskt nedbrytbart och giftigt: den främsta kritiken är att det är skadligt för människors hälsa och hämmar fotosynteshastigheten av vattenlevande liv. Metalljoner leder i allmänhet till biologiska och fysiologiska komplikationer när de binder till cellulära makromolekyler. Därför är effektiv och miljövänlig reningsteknik pressande för att tillhandahålla lösningar för vattenrening.
Denna avhandling syftar till att undersöka de elektro-/fotokatalytiska vattenreningsteknikerna med användning av olika katalysatorer. Effektiv elektrokemisk reduktion av nitrat uppnåddes genom att använda NDC-material, och de aktiva platserna bestämdes med hjälp av en omfattande solid-state NMR stödd av teoretiska beräkningar och DFT-beräkningar. Dessutom utfördes den fotokemiska färgämnesnedbrytningen med användning av cellulosabaserade hybrida bio-oorganiska katalysatorer. Det avsiktliga underhållet av ytfunktionella grupper på cellulosabaserade material kan främja färgämnesnedbrytningsprestanda och, viktigast av allt, uppnå samtidig borttagning av tungmetalljoner förutom fotofärgnedbrytning. Dessutom föreslog denna avhandling två möjliga syntesstrategier för att erhålla elektro-/fotokatalysatorer med användning av cellulosabaserade material som förnybara resurser. De tolv principerna för grön kemi styrde optimeringen av syntesvägen och råmaterialselektiviteten. Framför allt bibehöll lågtemperatursyntesen av hybridfotokatalysatorer ytfunktionella grupper och bevarade den kinetiska mekanismen för föroreningars adsorption på biosubstrat. Denna forskning kommer sannolikt att bidra till en djupare förståelse av förnybara material med gröna syntesmetoder för katalysatorer som är inriktade på vattenförorenings behandling.

List of Publications

This thesis is written based on the following publications:

1. Electrochemical denitrification and oxidative dehydrogenation of ethylbenzene over N-doped mesoporous carbon: Atomic level understanding of catalytic activity by ^{15}N NMR spectroscopy
Ireneusz Szewczyk, Anna Rokicińska, Marek Michalik, Jianhong Chen, Aleksander Jaworski, Rihards Aleksis, Andrew J. Pell, Niklas Hedin, Adam Slabon, and Piotr Kuśtrowski, *Chemistry of Materials*, **2020**, 32, 7263-7273.

Scientific contributions: Data curation, Formal analysis – Raman spectroscopy, Investigation – Electrochemical nitrate removal experiments, Writing – review & editing.

2. Reaction pathways on N-substituted carbon catalysts during the electrochemical reduction of nitrate to ammonia
Zheng Chen‡, Jianhong Chen‡, Giovanni Barcaro, Tetyana M. Budnyak, Anna Rokicińska, Richard Dronskowski, Serhiy Budnyk, Piotr Kuśtrowski, Susanna Monti, and Adam Slabon, *Catalysis Science & Technology*, **2022**, 12, 3582.
‡Indicates shared first authorship

Scientific contributions: Conceptualization, Data curation, Formal analysis – Raman spectroscopy, TEM analysis, Investigation – ^{15}N isotope labelling experiments, Writing – original draft.

3. Converting cellulose nanocrystals into photocatalysts by functionalisation with titanium dioxide nanorods and gold nanocrystals
Santhosh S. Nair‡, Jianhong Chen‡, Adam Slabon, and Aji P. Mathew, *RCS Advances*, **2020**, 10, 37374.
‡Indicates shared first authorship

Scientific contributions: Conceptualization, Methodology, Data curation, Formal analysis – TEM, XRD, UV-Vis analysis, Investigation – material synthesis, photo dye degradation experiments, Writing – original draft.

4. CelluPhot: Hybrid cellulose−bismuth oxybromide membrane for pollutant removal

Joy Onwumere, Jędrzej Piątek, Tetyana Budnyak, Jianhong Chen, Serhiy Budnyk, Zoheb Karim, Thomas Thersleff, Piotr Kuśtrowski, Aji P. Mathew, and Adam Slabon, *ACS Applied Materials & Interfaces,* **2020**, 12, 42891-42901.

Scientific contributions: Data curation, Formal Analysis – XRD, TEM analysis, Writing – review & editing.

Publications not included in the thesis

1. Tailoring the surface properties of Bi_2O_2NCN by in situ activation for augmented photoelectrochemical water oxidation on WO_3 and $CuWO_4$ heterojunction photoanodes
Zheng Chen, Alex J. Corkett, Caspar de Bruin-Dickason, Jianhong Chen, Anna Rokicinska, Piotr Kuśtrowski, Richard Dronskowski, and Adam Slabon, *Inorganic Chemistry,* **2020**, 59, 13589−13597.

Scientific contributions: Data curation, Formal Analysis – TEM analysis, Writing – TEM part.

2. Structural evolution of CrN nanocube electrocatalysts during nitrogen reduction reaction
Zili Ma, Jianhong Chen, Dongbao Luo, Thomas Thersleff, Richard Dronskowski, and Adam Slabon, *Nanoscale*, **2020**, 12, 19276–19283.

Scientific contributions: Data curation, Formal Analysis – TEM analysis, Writing – TEM part.

3. Sensibilization of *p*-NiO with ZnSe/CdS and CdS/ZnSe quantum dots for photoelectrochemical water reduction
Can Lu, Andreas Drichel, Jianhong Chen, Florian Enders, Anna Rokicińska, Piotr Kuśtrowski, Richard Dronskowski, Klaus Boldt, and Adam Slabon, *Nanoscale*, **2021**, 13, 869–877.

Scientific contributions: Data curation, Formal Analysis – TEM analysis, Writing – TEM part.

4. LignoPhot: Conversion of hydrolysis lignin into the photoactive hybrid lignin/$Bi_4O_5Br_2$/BiOBr composite for simultaneous dyes oxidation and Co^{2+} and Ni^{2+} recycling

Tetyana M. Budnyak, Joy Onwumere, Ievgen V. Pylypchuk, Aleksander Jaworski, Jianhong Chen, Anna Rokicinska, Mikael E. Lindstrom, Piotr Kuśtrowski, Olena Sevastyanova, and Adam Slabon, *Chemosphere*, **2021**, 279, 130538.

Scientific contributions: Data curation, Formal Analysis – TEM analysis, Writing – TEM part.

5. Lignin-supported heterogeneous photocatalyst for the direct generation of H_2O_2 from seawater
Aswin Gopakumar, Peng Ren, Jianhong Chen, Bruno Vinicius Manzolli Rodrigues, H. Y. Vincent Ching, Aleksander Jaworski, Sabine Van Doorslaer, Anna Rokicinska, Piotr Kuśtrowski, Giovanni Barcaro, Susanna Monti, Adam Slabon, and Shoubhik Das, *Journal of the American Chemical Society*, **2022**, 144, 2603-2613.

Scientific contributions: Data curation, Formal Analysis – TEM and XRD analysis, Writing – TEM and XRD part.

6. Increased photocurrent of $CuWO_4$ photoanodes by modification with the oxide carbodiimide $Sn_2O(NCN)$
Zheng Chen, Manuel Löber, Anna Rokicińska, Zili Ma, Jianhong Chen, Piotr Kuśtrowski, Hans-Jürgen Meyer, Richard Dronskowski, and Adam Slabon, *Dalton Transactions*, **2020**, 49, 3450–3456.

Scientific contributions: Data curation, Formal Analysis – TEM and XRD analysis, Writing – TEM and XRD part.

7. Impact of Mn addition on catalytic performance of Cu/SiBEA materials in total oxidation of aromatic volatile organic compounds
Anna Rokicińska, Patrycja Majerska, Marek Drozdek, Sebastian Jarczewski, Laetitia Valentin, Jianhong Chen, Adam Slabon, Stanislaw Dzwigaj, and Piotr Kuśtrowski, *Applied Surface Science*, **2021**, 546, 149148.

Scientific contributions: Data curation, Formal Analysis – TEM analysis, Writing – TEM part.

8. Graphitic nitrogen in carbon catalysts is important for the reduction of nitrite as revealed by naturally abundant ^{15}N NMR spectroscopy
Zheng Chen, Aleksander Jaworski, Jianhong Chen, Tetyana M. Budnyak, Ireneusz Szewczyk, Anna Rokicińska, Richard Dronskowski, Niklas Hedin, Piotr Kuśtrowski, and Adam Slabon, *Dalton Transactions*, **2021**, 50, 6857.

Scientific contributions: Data curation, Formal Analysis – TEM and Raman spectroscopy, Writing – TEM and Raman part.

9. Glycine-functionalized silica as sorbent for cobalt(II) and nickel(II) recovery
Jędrzej Piątek, Caspar N. de Bruin-Dickason, Aleksander Jaworski, Jianhong Chen, Tetyana Budnyak, and Adam Slabon, *Applied Surface Science*, **2020**, 530, 147299.

Scientific contributions: Data curation, Formal Analysis – TEM analysis, Writing – TEM part.

10. Electrochemical depolymerization of lignin in a biomass-based solvent
Márcia G. A. da Cruz, Robin Gueret, Jianhong Chen, Jędrzej Piątek, Björn Beele, Mika H. Sipponen, Marcella Frauscher, Serhiy Budnyk, Bruno V. M. Rodrigues, and Adam Slabon, *ChemSusChem*, **2022**, 15, e202200718.

Scientific contributions: Data curation, Investigation – electrochemical depolymerization tests.

11. $CeTiO_2N$ oxynitride perovskite: paramagnetic ^{14}N MAS NMR without paramagnetic shifts
Zili Ma, Can Lu, Jianhong Chen, Anna Rokicińska, Piotr Kuśtrowski, Robert Coridan, Richard Dronskowski, Adam Slabon, and Aleksander Jaworski, *Zeitschrift fuer Naturforschung B*, **2021**, 76.

Scientific contributions: Data curation, Writing – original draft.

12. Atomic-level understanding for the enhanced generation of hydrogen peroxide by the introduction of an aryl amino group in polymeric carbon nitrides

Tong Zhang, Waldemar Schilling, Shahid Ullah Khan, H. Y. Vincent Ching, Can Lu, Jianhong Chen, Aleksander Jaworski, Giovanni Barcaro, Susanna Monti, Karolien De Wael, Adam Slabon, and Shoubhik Das, *ACS Catalysis*, **2021**, 11, 14087-14101.

Scientific contributions: Data curation, Formal Analysis – TEM analysis, Writing – TEM part.

Abbreviations

Boron-doped diamond (BDD)

Cellulose nanocrystals (CNCs)

Cellulose nanocrystals supported titanium dioxide nanorods (CNC/TiO_2-NRs)

Cellulose membrane (CM)

Chronoamperometry (CA)

Conduction band (CB)

Cyclic voltammetry (CV)

Density functional theory (DFT)

Energy dispersive X-ray spectroscopy (EDS)

Gold nanocrystals (Au NCs)

Highest occupied molecular orbital (HOMO)

High-resolution transmission electron microscopy (HRTEM)

High-angle annular dark-field (HAADF)

Hydrogen evolution reaction (HER)

Linear sweep voltammetry (LSV)

Local surface plasmon resonance (LSPR)

Lowest unoccupied molecular orbital (LUMO)

Magic-angle-spinning (MAS)

Nanorods (NRs)

Nitrate reduction reaction (NO_3RR)

Nitrite reduction reaction (NO_2RR)

Nitrogen-doped carbon (NDC)

Nuclear magnetic resonance (NMR)

Oxygen evolution reaction (OER)

Oxygen reduction reaction (ORR)

Powder X-ray diffraction (PXRD)

Reactive oxygen species (ROS)

Reactive molecular dynamics (RMD)

Reduced graphene oxide (RGO)

Rhodamine B (RhB)

Scanning electron microscopy (SEM)

Scanning transmission electron microscopy (STEM)

Selected area electron diffraction (SAED)

Thermogravimetric analysis (TGA)

Titanium dioxide (TiO_2)

Transmission electron microscopy (TEM)

Valence band (VB)

X-ray photoelectron spectroscopy (XPS)

Contents

Abstract i
Sammanfattning ii
List of Publications iii
Publications not included in the thesis v
Abbreviations ix
1. Introduction 1
1.1 Water contamination 3
1.1.1 Nitrate 3
1.1.2 Dye 3
1.1.3 Heavy metal ions 4
1.2 Water purification technique addressing different contaminants 5
1.2.1 Electrochemical reduction 5
1.2.2 Photodegradation 8
1.2.3 Adsorption 10
1.3 Scope of the thesis 13
2. Methodology 14
2.1 Sample preparation 14
2.1.1 The synthesis of nitrogen-doped carbon (NDC) in paper *I* and *II* 14
2.1.2 The cathodic electrode preparation in paper *I* and paper *II* 15
2.1.3 The synthesis of CNC/TiO_2-NRs 15
2.1.4 The synthesis of CNC/TiO_2-NRs(90)/Au NCs and CNC/TiO_2-NRs(150)/Au NCs 16
2.1.5 The synthesis of $Bi_4O_5Br_2$/BiOBr and CM/$Bi_4O_5Br_2$/BiOBr 16
2.2 Electrochemical characterization 17
2.2.1 Electrochemical measurement 17
2.2.2 Determination of nitrate, nitrite and ammonia concentration 17
2.2.3 ^{15}N isotope labelling experiment 18
2.2.4 Calculation of nitrate conversion, selectivity, Faradaic efficiency and ammonia yield 18
2.3 Photocatalytic experiments 18

2.4 Batch adsorption of Co and Ni ions 19
2.5 Characterization techniques 20
2.5.1 Raman spectroscopy 20
2.5.2 X-ray photoelectron spectroscopy (XPS) 20
2.5.3 Thermogravimetric analysis (TGA) 20
2.5.4 N_2 adsorption 20
2.5.5 UV-Vis spectroscopy 21
2.5.6 Powder X-ray diffraction (PXRD) 21
2.5.7 Solid-state nuclear magnetic resonance (NMR) 21
2.5.8 Chemical shifts calculations 21
2.5.9 Scanning electron microscopy (SEM) 22
2.5.10 Transmission electron microscopy (TEM) 22
2.5.11 Scanning transmission electron microscopy (STEM) 22
3. Results and discussions 23
3.1 Electrochemical nitrate reduction with NDC catalysts 23
3.1.1 The characterization of NDC catalysts 23
3.1.2 Solid-state NMR characterization on SK_N 26
3.1.3 Electrochemical removal of nitrates 27
3.2 Electrochemical nitrate reduction with cellulose-derived NDC catalysts 28
3.2.1 The characterization of cellulose-derived NDC catalysts 28
3.2.2 Electrochemical removal of nitrates 31
3.2.3 Reaction mechanisms deduced by multi-scale calculations 34
3.3 Cellulose nanocrystal supported TiO_2 with Au NCs decoration 36
3.3.1 Converting CNCs into photocatalysts 36
3.3.2 Photocatalytic performance of CNC/TiO_2-NRs(90)/Au NCs and CNC/TiO_2-NRs(150)/Au NCs 40
3.4 Cellulose-bismuth oxybromide membrane for water purification 43
3.4.1 Converting cellulose into photocatalysts with $Bi_4O_5Br_2$/BiOBr deposition 44
3.4.2 Photocatalytic performance of CM/$Bi_4O_5Br_2$/BiOBr 47
3.4.3 Adsorption of Co(II) and Ni(II) ions 48
4. Summary and outlook 51
Acknowledgements 53
References 55

1. Introduction

Chemistry has long been perceived as a hazardous science and is often related to toxic products. Designing sustainable chemicals and processes requires great striving to reduce the intrinsic hazards to a safe standard, limiting the risk of damage. The concept of Green Chemistry, the "design of chemical products and processes to reduce or eliminate the use and generation of hazardous substances", was established at the beginning of the 1990s and consummated in the following 30 years.[4] Green Chemistry is characterized by careful chemical synthesis and design planning to reduce adverse consequences.[4–6] This concept goes beyond the laboratory and has had a profound impact on fields like education, industry, and public society in recent years. Therefore, it has been applied to many industry sectors, including agriculture, electronics, energy, aerospace, etc. Paul Anastas and John Warner pointed out that the concept of design is the most important aspect of Green Chemistry. Hence, in 1998, they introduced The Twelve Principles of Green Chemistry as the intentional goal of sustainability, which has been considered as design rules or guidelines for new chemical products and processes (Figure 1.1). A number of studies have demonstrated that adopting The Twelve Principles helps to improve the economic benefits, such as less investment in effluent treatment and less indemnity for environmental damages.[7] One of the principles is concerned with the "use of renewable feedstocks" as it reveals the necessity of avoiding petroleum feedstock or natural gas as raw materials for chemical synthesis. Shifting raw materials to sustainable options can be costly, however, this will bring profound benefits to the environment and public health once the system is thoroughly established.

In terms of environmental pollution, water contamination is becoming a key concern around the world. Approximately 2 million tons of organic, inorganic, and biological waste are discharged into worldwide waters daily.[8] Over 1.2 billion people do not have access to safe drinking water, and millions of humans die from contamination-related diseases every year.[9] Water treatment system also has a pivotal role in economic growth. The agriculture, livestock and energy industries consume more than 80% of all water for human use.[1] Apart from this, the demand for clean water is expected to keep up with the rapid increase in the world's population growth. Due to the lack of a basic water treatment system in many countries, it should be foreseen that water

scarcity will worsen in the coming decades. Alarmingly, receding glaciers could cause rivers to become intermittent and imperil terrestrial creatures with drought.[10,11] Besides, water scarcity can also disrupt agriculture, hydroelectric and thermoelectric generation, and municipal water supplements.[12,13]
A considerable number of strategies are emerging for water purification and offer hope for mitigating the impact of contaminated water. Conventional water treatment methods like disinfection and decontamination are usually chemically involved, energetically intensive and large-scale, which requires considerable financial support. All these factors preclude the worldwide application of water purification techniques. Furthermore, intensive residuals from chemical treatments can cause additional problems with water contamination. In a word, there is an urgent need to address the water contamination problem and explore possible green techniques with limited resources.

This thesis navigates several water contamination treatment processes using bio-based materials. The removal of nitrate was achieved with the electrochemical method, and the photodegradation method was applied for dye decomposition. The Twelve Principles of Green Chemistry were considered as a guide during the procedure of the optimization of the synthesis route and the selectivity of catalysts.

Figure 1.1 The Twelve Principles of Green Chemistry pocket guide. Reproduced from ACS webpage with their permission. (https://www.acs.org/greenchemistry/principles/12-principles-of-green chemistry.html)

1.1 Water contamination

Water is the essential compound for life on Earth. More than 71% of the earth's surface is covered by water providing habitat for aquatic animals.[1] Among the water on the earth, only 1%, as per international standards, is safe potable water. Anthropogenic activity like industry, agriculture, and municipal wastewater introduces the most contaminants, of which nitrate, colourful dyes and heavy metal ions are commonly referred.

1.1.1 Nitrate

The nitrogen cycle is fundamental to the biosphere, and the existence of multiple chemical forms through the nitrogen cycle affects the ecosystem processes. However, human interference in the global nitrogen cycle negatively impacts the natural environmental system and threatens human health. For example, the wide application of nitrogen-based fertilizers in agriculture results in the nitrate pollution of water. Nitrate in drinking water after the ingestion process is reduced to nitrite by the gastrointestinal tract, causing methemoglobinemia which is also known as "blue baby syndrome".[2,3] In addition to this, reduced nitrite can also disable the oxygen transport mechanism of the red blood cells.[14] Besides, nitrate can lead to the eutrophication of natural water bodies which causes algal blooms that severely harm the water quality and the aquatic environment. The World Health Organization set a maximum recommended concentration level of nitrate in drinking water at 50 mg/L.[14] However, nitrate is still one of the most commonly reported contamination violations worldwide, and thus, efficient and sustainable nitrate removal strategies are utterly essential for large-scale water treatments.

1.1.2 Dye

Organic dyes have widespread applications in various industries, especially textile, paint and paper industries.[15] More than a thousand dyes are used to colour fabrics in the textile industry; about 20% is lost during synthesis and processing operations and eventually exposed to wastewater. Dye-polluted water is usually nonbiodegradable and poisonous, which is harmful to human health and negatively affects the photosynthesis rate of aquatic life.[16] Furthermore, dyes exhibit excellent solubility in water due to their aromatic organic structure, making it even more challenging to remove them thoroughly.

1.1.3 Heavy metal ions

Heavy metal pollution emerged from anthropogenic activities, especially in mining, smelting, and other industries involving the application of metals. Nowadays, heavy metal contamination generally refers to metallic chemical elements and metalloids that are toxic to the environment and humans, even though some heavy metals are typically nontoxic. Heavy metal ions tend to bond to organic groups covalently, resulting in toxicological properties. These covalent bonded ions or compounds are lipophilic and easily develop biological and physiological complications when binding to cellular macromolecules. For example, it has been noted that cellular organelles are sensitive to heavy metals, and the interaction may cause DNA damage or carcinogenesis. Therefore, the last several decades have seen a growing trend towards removing heavy metal pollutants.

1.2 Water purification technique addressing different contaminants

The presence of dyes, toxic heavy metals, and nitrate is detrimental to human health and the environment, even with trace amounts. The low concentration of these compounds makes the remediation process even more difficult. Many techniques besides industrial methods have been established to remove these compounds from water with a better efficiency or greener approach, such as electro-reductive/oxidative processes, photo electrochemistry, and adsorption. These techniques have demonstrated different degrees of remediation performance.

1.2.1 Electrochemical reduction

Electrochemical reduction reactions involve chemical transformations of molecular or ionic solutes derived by faradaic reactions at electrodes. They are primarily used for nonbiodegradable heavy metal ions, inorganic anions, and halogenated organic compounds.[17–19] Electrochemical reduction reactions have many advantages over conventional chemical reduction processes. For example, it can be operated at an ambient temperature and pressure without additional waste production; desired products can be selected by applying a controllable potential.[20] As a complementary process to electrochemical oxidation, the electrochemical reduction can either occur on the cathode electrode surface or be achieved indirectly by the generated reducing agent in the electrolyte.[21] Figure 1.2 shows an example of direct and indirect pathways of electrochemical nitrate reduction.

The electrochemical reduction efficiency can be affected by many parameters, of which electrode material, catalyst loading amount and applied potential are the most influential variables.[20] Generally, increasing the catalyst loading amount improves the reaction activity. However, this is only up to a limit beyond which reaction activity either steady or drops due to the increase of electron transfer distance.[22] For example, Chen et al. identified the effect of the loading amount of titanium nitride from nanosized titanium nitride-doped Pd/Ni electrodes for electrochemical reductive dichlorination of 2,4-dichlorophenoxy acetic acid. The results showed an improvement in 2,4-dichlorophenoxy acetic acid removal efficiency from 25.56 % to 72.01 %, with the nanosized TiN increase from 0 mg to 2 mg. However, it was followed by a reduction to only 54.63 % in removal efficiency when the TiN further increased to 5 mg. In this case, the aggregation of nanosized TiN at high concentrations covered the available Pd active sites. Eventually, it prevented them from contacting reactants and the replacement reaction with Pd^{2+}.[23]

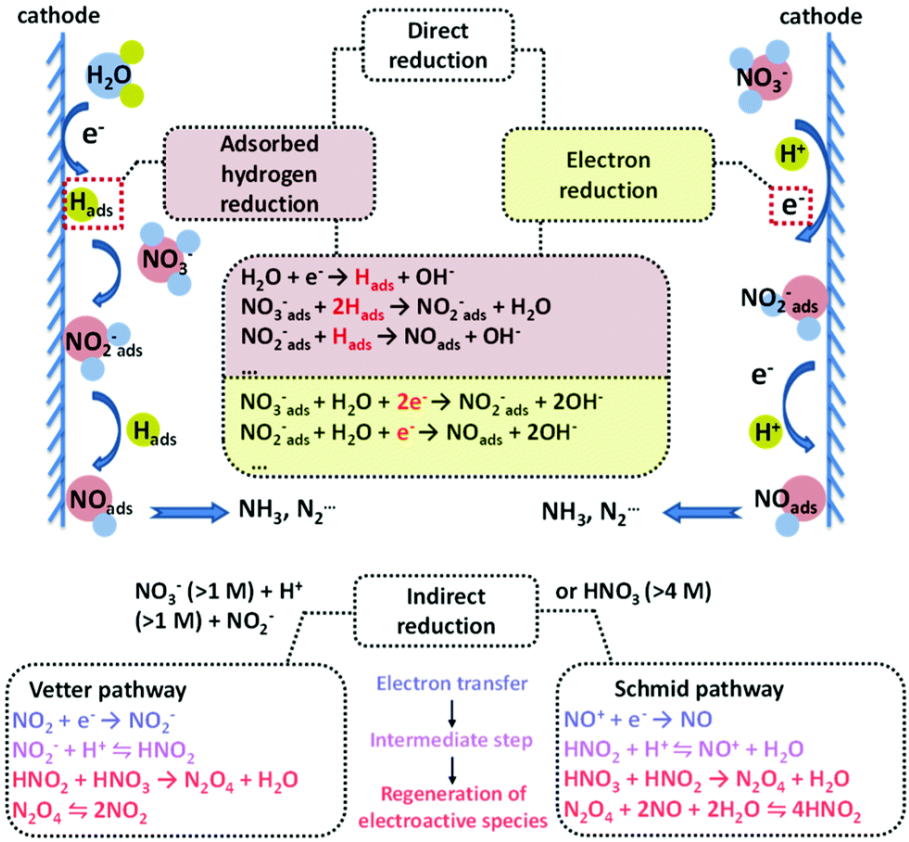

Figure 1.2 The proposed direct and indirect nitrate electrochemical reduction pathway. Reproduced from [24] with permission.

Cathodic potential significantly influences the thermodynamics and kinetics of electro-reduction reactions.[20] One can assume that the applied current density is much higher than the optimized conditions. Then the side reaction products could impede the adsorption of reactants on the electrode and thus retard the reaction activity due to mass transport limitation. In most cases, the side reaction products are hydrogen bubbles from hydrogen evolution reaction (HER).[25–27]

The choice of electrode materials is also critical for the electrochemical reduction efficiency, selectivity and reaction pathways.[20,21] Many studies have been working on different electrode materials for nitrate electroreduction, such as mono metal electrodes: Cu, Pd, Pt, Pb, Ti etc.[28] Among these, Cu shows the highest activity but is usually accompanied by harmful ammonium and nitrite as by-products in alkaline and acidic media.[29–32] The electrochemical nitrate reduction with Sn as cathode has been reported by Katsounaros et al., and it showed 70 % selectivity to nitrogen with a 95 % degradation efficiency from a 100 mg/L initial concentration of nitrate.[33] However, the corrosion of the Sn cathode introduces a second contamination

into the electrolyte. A synergic effect of bimetallic electrodes can improve monometallic electrodes' corrosion resistance and stability. For example, Cu-Ni, Cu-Sn, Sn-Pd, and Cu-Pd have been widely studied and show significant improvement.[34–49] A maximum nitrogen selectivity of 70 % has been reported by Pd-Cu modified graphite electrode with 1M NaOH electrolyte.[44]
In addition, various transition metal compounds and transition metal composite electrodes have been studied for the electrochemical reduction of nitrate in water.[50–57] Several attempts have been made to use metal-free materials as cathodes for electrochemical nitrate reduction because of their low cost, remarkable mechanical performance, and highly tuneable electronic structures compared with metallic electrodes.[29,58–61] It should be noted that applying metal-free electrodes can avoid secondary pollution. The electrochemical performance of the conductive diamond, silicon carbide, and graphite was explored, among which graphite showed the highest activity, efficiency, and even better corrosion resistance than a bimetallic alloy (CuNi).[29] Rao et al. compared the electrochemical performance of carbon paper with Ti, Fe, Cu and Al cathodes for nitrate reduction. Carbon paper in this work exhibited the highest removal rate (47.7%). The defective graphene electrode showed higher nitrate electro-reduction activity and better organic poisoning tolerance than the Pt electrode, proving that introducing defects significantly improves the reduction activity and reaction stability.[62] Besides, the high corrosion resistance and wide potential window of boron-doped diamond (BDD) make it a possible material for the cathode material. The nitrate removal rate was over 90% by using BDD as both cathode and anode regardless of initial nitrate concentration.[59] The same group subsequently improved to 91% nitrate removal performance in 2 hours with negligible nitrite and ammonia by-products.[60] Furthermore, the highest Faradaic efficiency of 45.2% for N_2 was reported by using BDD as the cathode.[61]

The high-energy efficiency, advantages of controllable selectivity, and the environmental compatibility of electrochemical reduction make it a promising method for aqueous nitrate remediation. The electrochemical reduction of nitrate usually involves N_2, NO_2^- and NH_4^+ as the leading products, as well as NO_2, NO and N_2O as by-products. Among these, N_2 is an ideal desired product which can purely eliminate the nitrogen source by emitting to the atmosphere and thus achieving a green elimination and remediation of nitrate from water. On the other hand, ammonium is another popular nitrate reduction product since it can be further recovered and re-utilized. As mentioned above, the application of metal-free cathode as an electrochemical reduction of nitrate can be very promising by combining excellent activity, outstanding stability and environmentally friendly perspectives as long as they can be competitive with metallic electrodes.

1.2.2 Photodegradation

Conventional methods such as precipitation, adsorption, and floatation are difficult to completely remove organic pollutants, especially challenging for dyes because of their complex structures. The photocatalytic degradation of persistent organic pollutants is an effective and sustainable strategy to reduce contamination under light illumination and ambient conditions. Photocatalytic dye degradation is usually performed by producing hydroxyl and superoxide radicals as internal oxidizing agents. The oxidation potentials required for hydroxyl and superoxide radicals are 2.7 eV and –2.3 eV, respectively. More significant than the range of oxidation potential of dyes (–1 to 2 eV), thus resulting in the immediate electron transfer of dyes with oxidation species.[63] The mechanism of single-component semiconductor photocatalytic degradation usually involves the excitation of valence band (VB) electrons into the semiconductor's conduction band (CB) with light illumination, which leaves holes in the valence band and is the potent oxidizing agent. Meanwhile, the promoted electrons react with dissolved oxygen species to produce superoxide ions. The oxidizing agent and superoxide ions are responsible for the degradation of pollutants and the redox reactions, respectively.[64] As a result, the charge separation and electron-hole combination are crucial for photocatalytic performance, and usually, single-component semiconductor suffers from fast electron-hole recombination. Heterojunction materials were developed to improve the photocatalytic performance of single-component photocatalysts. Based on the band gap theory, three mechanisms between heterojunction semiconductors have been proposed and widely accepted for electron-hole formation and transfer. (See Figure 1.3)

Hybrid semiconductors (e.g., SnO_2/ZnO, WO_3/$NiWO_4$, and Sb_2S_3/TiO_2) can boost photocatalytic performance by suppressing electron-hole recombination, as explained by heterogeneous pairing theory.[65,66] The theory suggested that electrons from the conduction band with a higher Fermi level shift to the CB of a second material with a lower Fermi level. By contrast, the holes move from the valence band with a lower Fermi level to a second material with a higher Fermi level.[67]

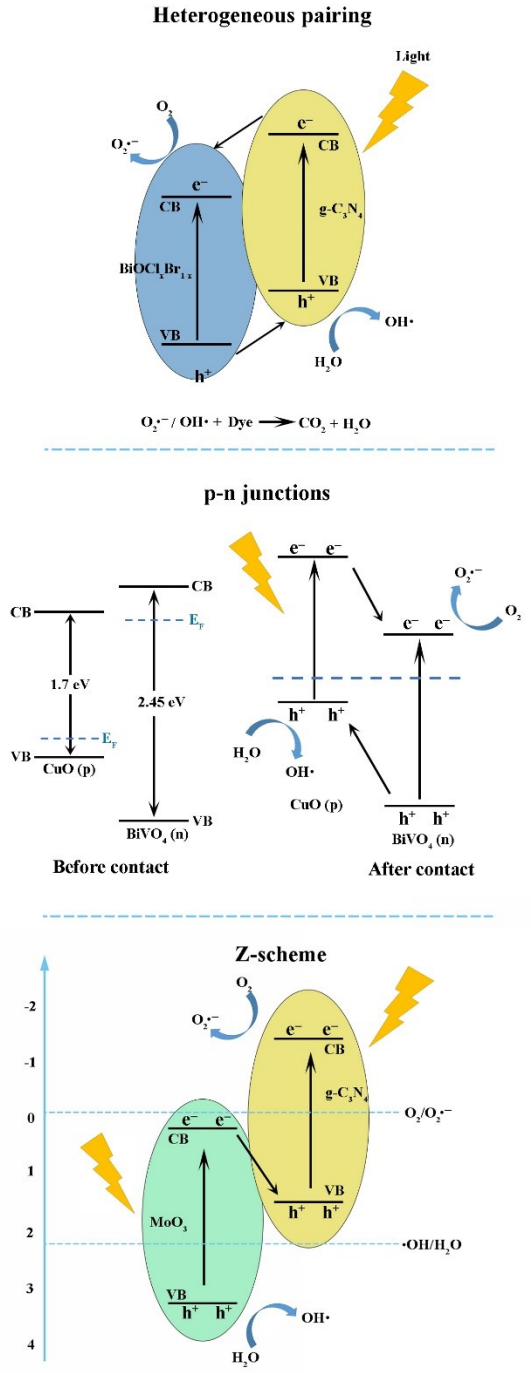

Figure 1.3 Schematic diagram of electron-hole formation and transfer between heterojunction semiconductors: heterogeneous pairing theory; p-n junction theory; and Z-scheme theory. Adapted with permission from [68].

A p-n junction facilitates the charge carrier separation by electrostatic forces. The formation of junctions establishes an internal electric field across two semiconductors, forcing the electron transfer until equilibrium. In other words, the band gaps of p-n junction photocatalysts initially overlapped. Then the electron transfer between the p-n junction results in a virtual staggered band alignment.[68] Typically, the semiconductor with a lower Fermi level acts as the p-type semiconductor, and another semiconductor acts as the n-type. The light illumination activates the transfer of electrons to move from p- to n-type of the conduction band; meanwhile, holes are transferred from n- to the p-type of the valence band. Therefore, the heterojunction effectively separates charge carriers and reduces electron-hole recombination.[69]
The Z-scheme mechanism supplemented the p-n junctions theory by focusing on oxidation/reduction during the light-introduced reaction. As z-scheme theory describes, the electrons in the Highest occupied molecular orbital (HOMO) of the semiconductor transfer to a second semiconductor's HOMO; then, electrons are promoted to the Lowest unoccupied molecular orbital (LUMO) of the second semiconductor. Eventually, the reactive oxygen species (ROS) generated at LUMO and HOMO work on degrading organic pollutants.

Besides the heterojunction semiconductors mechanisms, the local surface plasmon resonance (LSPR) effect over Titanium dioxide (TiO_2) should also be mentioned. TiO_2 has received much attention in the past few years among various types of photocatalysts regarding its non-toxicity, unique optical properties and chemical stability. However, the wide band gap of TiO_2 (3.2 eV for anatase) and low quantum efficiency limited the practical application within the UV region. Many strategies have been used to expand the light adsorption performance of TiO_2 for efficient solar light utilization. Besides the heterojunction materials mentioned above, the LSPR effect has attracted much interest. The LSPR effect arises from the local electric field and magnetic field interfering at the surface of Au, Ag, Pd and Bi particles under light illumination. Meanwhile, the energetic electrons are known as 'hot electrons' generated from the plasmon decay and pass the Schottky barrier into the CB of the semiconductor, eventually participating in the photocatalytic reaction under light illumination. The LSPR effect can extend the light response properties of TiO_2 into the visible light region.

1.2.3 Adsorption

Adsorption occurs when a liquid or a gas solute accumulates on the surface of an adsorbent (solid or liquid), forming a molecular or atomic film (adsorbate) (See Figure 1.3). Generally, the adsorption process proceeds in four consecutive steps: (*I*) bulk diffusion, (*II*) external mass diffusion or film

diffusion, (*III*) pore diffusion, and (*IV*) chemical/physical reactions of adsorbate with active sites from the adsorbent.[70] Typically, the adsorption kinetics is mainly controlled by film diffusion and/or pore diffusion since the chemical/physical usually reacts fast. The film diffusion rate depends on the liquid concentration and boundary layer of phases; however, the structure of adsorbent and adsorbate also affects the pore diffusion rate.

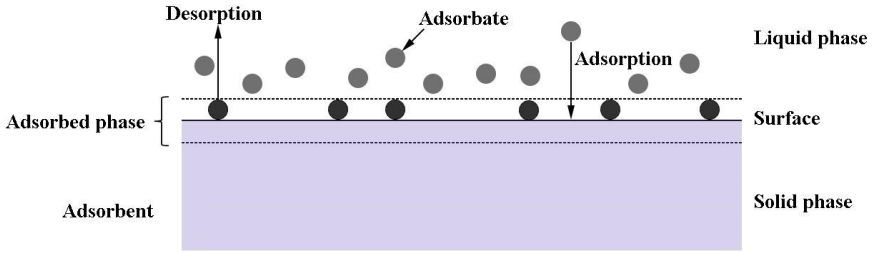

Figure 1.4 Adsorption diagram and basic terms. Adapted with permission from [71].

Many factors affect the adsorption performance, whereas this thesis mainly discusses pH, temperature and the effect of coexisting pollutants. The solution pH affects the interactions between adsorbents and pollutants, by interfering with the protonation of adsorbents' functional groups and the ionization of adsorbates. Figure 1.4 shows a pH-dependent anionic adsorption process schematic diagram. The adsorption of cationic adsorbates follows a similar pattern. As a result, the pH value should be optimized to avoid the electrostatic repulsion between adsorbate and adsorbent. Temperature is another critical parameter for adsorption capacity and pollutants removal rate due to the influence on the activation energy of the adsorption process.[72] However, increasing the temperature can either promote or impede the adsorption performance depending on whether the system is endothermic or exothermic. In reality, pollutant usually coexists with other contaminants. Hence, competitive adsorption could occur between contaminants with the same surface charge status. For instance, it has been proved that the coexisting carbonate, sulphate and phosphate significantly reduce the adsorption capacity of halogen anions and oxyanions.[73] The coexisting of SO_4^{2-} with Cr(*VI*) minimizes the uptake of performance on Cr(*VI*) by consuming the surface binding sites from the adsorbent.[74]

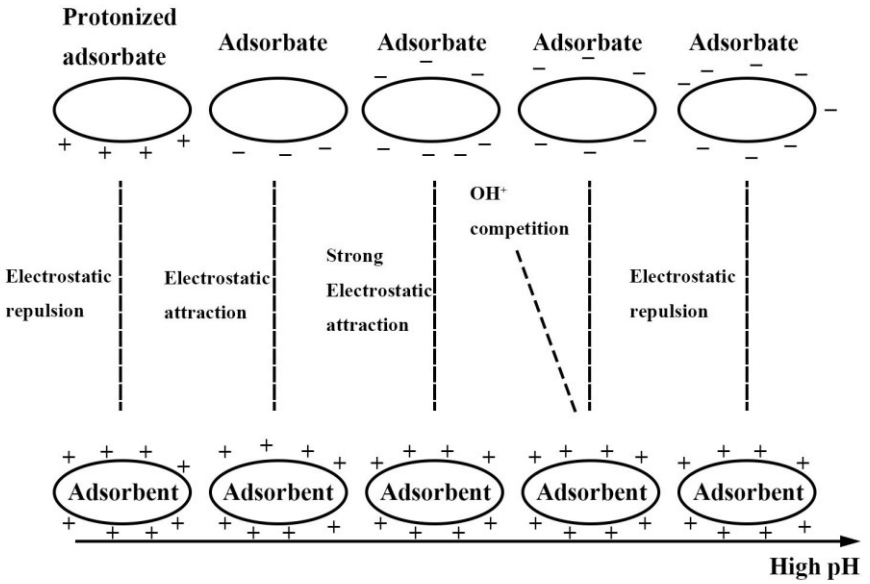

Figure 1.5 Schematic diagram of a typical pH-dependent adsorption process. Adapted with permission from [72].

The adsorption technique has been considered suitable for water purification due to its simplicity, high removal capacity and low operating cost.[75] Generally, the adsorbents for water treatment can be divided into five categories, biomass adsorbents, natural adsorbents, synthetic adsorbents, agricultural wastes and industrial wastes. Among different types of adsorbents, agricultural wastes and biomass adsorbents have been considered to possess great potential for contamination removal after specific processing.[76] Especially in recent years, biodegradable adsorbents such as cellulose-based sorbents have attracted much attention for heavy metals removal since cellulose is abundant, low cost, nontoxic, and biodegradable.[77] Notably, the removal of various contaminations is expedited by functionalizing with specific functional groups such as alcohol, phenol, aldehyde, carboxyl and ketone.[78] Moreover, the porous structure of cellulose-based sorbents can even increase the capacity of active agents for adsorption, which further promotes the adsorption performance of functionalized cellulose. Aji et al. reported the functional biomass membranes of micro-fibrillated cellulose with mixed and layered architectures showed effective removal performance on metal ions.[79] The carboxyl moieties play a crucial role in the capture of metal ions.[80,81] The liquid phase reduction method achieved a combination of sawdust cellulose with zero-valent iron, and the hybrid material reveals a high adsorption capacity of Cr^{3+} up to 268.7 mg/g.[82] Cellulose-based adsorbents show great potential for heavy metal contaminant removal.

1.3 Scope of the thesis

The main goal of this thesis was to find efficient techniques and sustainable catalysts that navigate water contaminants treatment, as well as understand the structure-property relationships of the catalysts.

The first part of this thesis aims at electrochemical nitrate reduction. Nitrogen-doped carbon (NDC) materials were selected as catalysts to avoid secondary pollution during the reaction processes. Furthermore, the contribution of different nitrogen species, such as pyridinic-N, pyrrolic-N and graphitic-N, was investigated with solid-state nuclear magnetic resonance (NMR). A correlation on selectivity can be established by comparing the nitrate electro-reduction products with the nitrogen species, which would be fundamental to understanding the nitrate electrochemical reduction mechanism and further guide this technique in the future. Most importantly, a sustainable cellulose-derived NDC synthesis method by ammonolysis was applied, and the NDC prepared by this method showed excellent activity and selectivity in electrochemical nitrate reduction.

The second objective was to prove the feasibility of combining biomass functional templates with semiconductors as hybrid catalysts for photocatalytic dye degradation. In this work, cellulose nanocrystals (CNCs) and cellulose membranes (CM) functioned as the template for the growth of TiO_2 nanorods (NRs) and $Bi_4O_5Br_2$/BiOBr, respectively. The cellulose-based template can provide mechanical support for semiconductors and even contribute to dye or heavy metal ions adsorption.

2. Methodology

2.1 Sample preparation

Throughout the work, two different categories of catalysts were used for water contaminants remediation. 1) The NDC was applied to electrochemical nitrate reduction, and 2) hybrid bio-inorganic material was used for dye photodegradation with simultaneous heavy metal ions adsorption. The NDC material from paper *I* was provided by the Faculty of Chemistry of Jagiellonian University, Poland, and fabricated subsequently as a composite electrode on a carbon substrate. The NDC material used in paper *II* was synthesised in the Institute of Inorganic Chemistry, RWTH Aachen University, Germany, and used for the preparation of composite electrodes on a carbon substrate. For papers *III* and *IV*, CNCs and CM materials were supplied by our collaborator Prof. Aji P. Mathew's group, Stockholm University, and chemically modified to obtain bio-inorganic hybrid materials. The following parts explain the procedure to obtain NDC, CNC/TiO_2-NRs/Au NCs and CM/$Bi_4O_5Br_2$/BiOBr catalysts.

2.1.1 The synthesis of nitrogen-doped carbon (NDC) in paper *I* and *II*

For paper *I*, NDC materials were synthesised by our collaborators. Briefly, spherical silica gel (40–75 μm particle size, Supelco) and acidified sucrose solution were used as a template and carbon precursor for preparing the carbon replica, respectively. The silica gel was modified by a simple impregnation method with a procedure of 1) 100 ℃ for 6 h; 2) 160 ℃ for 6 h. Then the material was carbonized with a contentious flow of N_2 at 650 ℃ for 4 h. Subsequently, the as-obtained material was washed by HF solution, DI water, and ethanol stepwise before drying at 50 ℃ and denoted as S0. A sample named SK can be obtained by the modification of S0 with an aqueous solution of HNO_3. S0 and SK were further modified with N_2 and a mix of NH_3/He at elevated temperatures, and the samples after the reaction were marked as S0_N and SK_N, respectively. Detailed information can be found in paper *I*.

For paper *II*, NDC was prepared with cellulose (microcrystalline, Sigma Aldrich) as the initial material as follows. Firstly, 3 g of cellulose was dried in a tube furnace at 250 ℃ for 6 h with a continuous N_2 flow at 40 mL min^{-1}; afterwards, the sample was soaked in 30 mL of 40 wt% HNO_3 solutions at 50 ℃ for 3 h. The materials were dried overnight at 120 ℃ after centrifuging and washing with deionized water. Next, the dried materials were carbonized with a 20 mL min^{-1} flow of NH_3 and H_2 mixture with a 3:1 ratio based on previous experiments.[83,84] The carbonization was carried out at temperatures ranging from 500–900 ℃ for 2 h. The resulting modified NDC were marked according to carbonization temperature as NDC-500, NDC-600, NDC-700, NDC-800 and NDC-900, respectively.

2.1.2 The cathodic electrode preparation in paper *I* and paper *II*

For paper *I*, the electrodes for electrochemical nitrate reduction were prepared as follows. Firstly, a precursor solution was prepared by mixing 5 mg NDC (from the Faculty of Chemistry of Jagiellonian University) with 30 μL of Nafion (D-520 dispersion 5% w/w in water and 1-propanol, Alfa Aesar) and 970 μL of ethanol (≥99 %, VWR Chemicals). The solution was dispersed by Ultrasonic Cleaner (USC 300T, VWR) for 5 min before dropping on the carbon paper support. For the preparation of the electrode, 200 μL of uniform precursor solution was dropped on each side of the carbon paper substrate (Toray carbon-paper TP-030, Quintech), followed by drying for 1 h at room temperature.

The preparation of electrode in paper *II* was similar to the methods in paper *I* but slightly modified. A similar precursor solution was prepared by mixing 6 mg of NDC sample with 30 μL Nafion (D-520 dispersion 5 wt%, Alfa Aesar) and 270 μL ethanol. The solution was dispersed by ultra-cleaner before dropping 100 μL on each side of the pre-cleaned carbon paper substrate (Toray carbon-paper TP-030, Quintech). Subsequently, the electrode was obtained after drying for 2 h at room temperature.

2.1.3 The synthesis of CNC/TiO_2-NRs

For paper *III*, the cellulose nanocrystals supported titanium dioxide nanorods (CNC/TiO_2-NRs) were provided by Prof. Aji P. Mathew's group. The CNCs functionalized with carboxylic acid were synthesised and extracted as the method reported in the literature.[85–87] Afterwards, 0.01 g of CNCs were ultrasonically dispersed in 10 mL ethanol and stirred for 1 h to form a homogeneous suspension. Titanium butoxide (0.01 mL) was injected into the resulting suspension and stirred magnetically for 1 h before being aged at

60 ℃ for 3 h. To implement the *in situ* growth of TiO_2 NRs on CNCs, the TiO_2 seeds were first produced by annealing the filtered above-mentioned suspension at 100 ℃. The as-prepared seeds deposited CNCs were mixed with DI water and conc. HCl, then heated at 90 ℃ under ambient pressure and atmosphere for 5 h, adding 1 mL $TiCl_4$. The as-prepared CNC/TiO_2-NRs(90) were cleaned stepwise with DI water and ethanol.

For the preparation of CNC/TiO_2-NRs(150), carboxylic acid functionalized CNCs were used as the template. Seed-coated CNCs were uniformly mixed with 25 mL DI water, 25 mL conc. HCl and 1 mL of $Ti(OBu)_4$. Subsequently, the resulting solution was heated at 150 ℃ for 4 h in a Teflon-line autoclave. Then, the obtained product was cleaned sufficiently with DI water and ethanol to remove the residual ionic species.

2.1.4 The synthesis of CNC/TiO_2-NRs(90)/Au NCs and CNC/TiO_2-NRs(150)/Au NCs

As reported in the literature, the gold nanocrystals (Au NCs) were synthesised by the colloidal method.[88] Briefly, 20 mL of 1-octadecene (90%, Aldrich) was degassed under nitrogen flow at 130 ℃ for 30 min in a three-neck flask. After cooling down to room temperature, 4 mmol oleylamine (90 %, Aldrich), 4 mmol 1,2-hexadecanediol (90 %, Aldrich) and 0.8 mmol anhydrous gold (III) acetate (99 %, Alfa Aesar) were added into the flask. Followed by heating at 200 ℃ under continuous nitrogen flow for 2 h. After cooling to room temperature, 35 mL of ethanol was added into the solution to precipitate the NCs with centrifuged at 12000 rpm. The final Au NCs were dispersed in hexane after being washed with ethanol.

For the preparation of Au NCs decorated catalysts, as-obtained CNC/TiO_2-NRs(90) and CNC/TiO_2-NRs(150) were added to Au NCs dispersion, respectively. The hybrid materials were obtained after drying under an ambient atmosphere for 24 h.

2.1.5 The synthesis of $Bi_4O_5Br_2$/BiOBr and CM/$Bi_4O_5Br_2$/BiOBr

For paper *IV*, $Bi_4O_5Br_2$/BiOBr and cellulose membranes (CM) supported with $Bi_4O_5Br_2$/BiOBr were obtained, and cellulose membrane was synthesised by Prof. Aji, P. Mathew's group. For the synthesis of $Bi_4O_5Br_2$/BiOBr, 20.6 mmol of $Bi(NO_3)_3$ and 16.8 mmol of KBr were dissolved in 10 mL of DI water first; then pH was adjusted to 13 with NaOH (1 M). The mixture was heated at 115 ℃ for 20 h in a Teflon-lined stainless-steel autoclave. In the end, the products were collected after washing with DI water until pH 7 was observed.

For the synthesis of CM/$Bi_4O_5Br_2$/BiOBr, the same procedure was implemented but with adding a cellulose membrane fragment (5 × 3) to the basic solution and followed by the heating in the Teflon-lined stainless-steel autoclave. In the end, the product was collected after washing with DI water until pH 7 was observed.

2.2 Electrochemical characterization

2.2.1 Electrochemical measurement

A typical three-electrode system was applied to study the electrocatalytic performance of NDC-deposited electrodes in paper *I*. A platinum wire and 1 M Ag/AgCl electrode were used as the counter and reference electrodes, respectively. The NDC electrode was used as the working electrode, while all three electrodes were connected to a BioLogic potentiostat. The electrochemical nitrate reduction was tested in an open cell with 0.1 M Na_2SO_4 electrolyte with 200 ppm of NO_3^- in Milli-Q water (18.3 Ω cm) as electrolyte. The linear sweep voltammetry (LSV) was performed at a scan rate of 10 mV s^{-1}, and the chronoamperometry (CA) test for 3 h was recorded.

The electrochemical measurements of paper *II* were carried out using a Gamry Instruments potentiostat and operated in a three-electrode system. The reactor was a relatively sealed H-type cell separated by a Nafion 117 membrane. Milli-Q water (18.3 Ω cm) was used to prepare 0.1 M Na_2SO_4 with 100 ppm of NO_3^- electrolyte, which was bubbled with N_2 for 1 h before the test. Cyclic voltammetry (CV) and LSV were performed at a scan rate of 10 mV s^{-1}; CA was recorded for a 48 h reaction. All the applied potentials in paper *II* were against 1 M Ag/AgCl to avoid the effects of pH changing during the process.

2.2.2 Determination of nitrate, nitrite and ammonia concentration

For paper *I*, the method described by Robarge et al.[89] was used to evaluate the nitrate concentration after the reaction; the concentration of nitrite was determined by the Merck Spectroquant 114773 test kit (Merck KGaA), and the concentration of ammonia was analysed by means of the Nessler method.[90] For paper *II*, another technique, as reported in the literature, was applied to quantify the nitrate concentration. The concentration of nitrate can be calculated according to the absorbance at 220 nm and 275 nm of a mixed solution with electrolyte, 0.1 mL of HCL (1 mol l^{-1}) and 0.01 mL sulfamic acid (0.8 wt%). Nitrite concentration was determined by MColortestTM test kits (114658, MColortestTM), and the concentration of ammonia was

analyzed by Merck Spectroquant test kits (114423, Merck Spectroquant). Detailed information can be found on paper *I* and paper *II*.

2.2.3 ^{15}N isotope labelling experiment

The isotope labelling nitrate reduction experiments were carried out to clarify the source of N in ammonia. The above-mentioned electrochemical measurement was used, except for the replacement of NO_3^- with $^{15}NO_3^-$ (≥99 %, Sigma Aldrich). The pH of the electrolyte after the reaction was adjusted to weakly acidic with diluted sulfuric acid. Subsequently, the obtained solution was quantified by ^1H NMR (400 MHz) after adding D_2O as the internal standard.

2.2.4 Calculation of nitrate conversion, selectivity, Faradaic efficiency and ammonia yield

The nitrate conversion, selectivity, Faradaic efficiency and ammonia yield were calculated according to the equations:

$$NO_3^- \ reduction \ efficiency = \Delta C_{NO_3^-}/C_0 \ \times 100\%$$

$$NH_4^+ \ selectivity = (C_{NH_4^+}/18) \times (\Delta C_{NO_3^-}/62) \ \times 100\%$$

$$NH_4^+ \ Faradaic \ efficiency = (8F \times C_{NH_4^+} \times V) \times 18Q \ \times \ 100\%$$

$$NH_4^+ \ yield = (C_{NH_4^+} \times V) \times (18 \times t \times m \ ) \times 100\%$$

Where C_0 is the initial concentration of nitrate; $\Delta C_{NO_3^-}$ represents the concentration difference of nitrate before and after the reaction (ppm); $C_{NH_4^+}$ is the detected concentration of ammonia after reaction; V is the electrolyte volume (50 mL); F is the Faradaic constant; Q represents the total charge; t is the time of electrolysis in an hour; and m is the mass of catalyst (2 mg).

2.3 Photocatalytic experiments

For paper *III*, rhodamine B (RhB, pure, Acros) was employed as a contaminant to study the photocatalytic degradation performance of the hybrid bio-inorganic catalysts. In detail, 200 mg of the sample was placed in 50 mL of an aqueous solution of 8 ppm RhB, adding hydrogen peroxide (35 wt%, ACROS)

as the electron scavenger. The mixture was stirred magnetically in darkness for 30 min before light illumination to achieve the adsorption-desorption balance. To evaluate the degradation rate of catalysts, the solution was illuminated with 100 mW cm^{-2} AM 1.5 G light (1 sun) generated by a solar light simulator (class-AAA 94023A, Newport) with an ozone-free 450 W xenon short-arc lamp with continuous magnetic stirring. The experiment was carried out in the darkness with the solar light simulator as the only light source to avoid any other irradiation on the sample. For every 20 min, an appropriate amount of solution was taken and filtered to remove the solid catalyst particles. Subsequently, the degradation rate of RhB was determined by the intensity of the main absorbance band at the wavelength of 555 nm as a function of irradiation time by UV-vis spectroscopy (WPA, S800+ Biochrom).

For paper *IV*, the same RhB (8 ppm) solution with hydrogen peroxide as paper *III* was used to study the photocatalytic degradation performance of CM/$Bi_4O_5Br_2$/BiOBr. The hybrid membrane was added to the solution, and the mixture was irradiated by blue light (405 nm, 20 W). As a comparison experiment, the degradation performance $Bi_4O_5Br_2$/BiOBr (17 mg) semiconductor was studied with the same condition. The experiments were carried out in darkness in order to avoid any other irradiation deviation. The mixtures were magnetically stirred under darkness for 30 min before the irradiation to achieve the adsorption-desorption balance. Subsequently, 5 mL aliquots were taken and studied by spectrometer every 20 min. The absorbance value eventually determined the degradation rate of RhB at the central band of 555 nm.

2.4 Batch adsorption of Co and Ni ions

For paper *IV*, the adsorption ability of CM and CM/$Bi_4O_5Br_2$/BiOBr on Co(II) and Ni(II) were implemented. Detailed information can be found in the publication.[91] Briefly, the adsorption kinetics of Co(II) and Ni(II) were measured using a static method. The flasks contained 25 mL solutions of 0.03 g CM or CM/$Bi_4O_5Br_2$/BiOBr, 20 mg L^{-1}/50 mg L^{-1} Co(II) and Ni(II) separately were shaken in Heidolph Unimax 1010 incubating shaker for 5, 24, 48, 72 and 94 h at 180 rpm and 22 °C. The concentration of metal ions after shaking was studied by photometrical method with a UV-3100PC spectrophotometer (VWR, Radnor, PA). The deviation was optimized by repeating the experiments three times, and the obtained results were taken as mean values.

2.5 Characterization techniques

2.5.1 Raman spectroscopy

For paper *I–III*, the Raman spectra were recorded with LabRAM HR 800 spectrometer equipped with an 800 nm focal length spectrograph. The back-thinned CCD detector with 1024 × 256 pixels was air-cooled at –70 °C. The air-cooled double frequency Nd: YAG laser (532 nm/50 mW), edge, and interference filters for measurements < 100 cm^{-1} were used. The intensity was adjusted by the software-controlled filter wheel with 6ND filters.

2.5.2 X-ray photoelectron spectroscopy (XPS)

For paper *I* and paper *II*, the XPS measurements were performed in Prevac photoelectron spectrometer equipped with a hemispherical analyser (VG, SCIENTA R3000). The spectra were recorded using a monochromatized aluminium source Al K_α (E=1486.6 eV). The surface composition was analysed, taking into account the areas and binding energies of C 1s, O 1s, and N 1s core levels.
For paper *IV*, the measurement was performed by Theta Probe (Thermo Fisher Scientific) with a monochromated Al K_α source at 1386.6 eV. The binding energy scale was calibrated with a C–C component at 285.0 eV.

2.5.3 Thermogravimetric analysis (TGA)

The loading amount of TiO_2 on CNC/TiO_2-NRs(90) and CNC/TiO_2-NRs(150) was studied by the TGA (Perkin Elmer TGA 7) in the air between 30–650 °C with a heating rate of 10 °C min^{-1}.

2.5.4 N_2 adsorption

For paper *II*, the N_2 adsorption was implemented by using the ASAP 2020 instrument (Micrometrics) at –196 °C. The samples were degassed under a dynamic vacuum at 250 °C for 4 h before the measurement. The obtained data were analysed with the following models: Bruauer-Emmett-Teller surface area (S_{BET}), Langmuir surface area ($S_{Langmuir}$), t-plot micropore volume (V_{micro}), and Barrett–Joyner–Halenda mesopore volume (V_{meso}). The total pore volume (V_{total}) was determined by the single-point method ($p/p_0 \sim 0.99$). For paper *III*, the BET-specific surface area of CNC/TiO_2-NRs(90) and CNC/TiO_2-

NRs(150) was studied with Micromeritics ASAP 2020 instrument. All samples were degassed at 90 ℃ for 5 h before the measurement. For paper *IV*, the BET specific surface area was studied by Micromeritics ASAP 2020 instrument after degassing at 80 ℃ for 5 h.

2.5.5 UV-Vis spectroscopy

For paper *III*, The optical properties of CNC/TiO_2-NRs(90), CNC/TiO_2-NRs(150), CNC/TiO_2-NRs(90)/Au NCs and CNC/TiO_2-NRs(150)/Au NCs were studied by UV-Vis spectrophotometer (Agilent Cary 5000) in the spectral range of 250–800 nm.

2.5.6 Powder X-ray diffraction (PXRD)

For paper *I*, XRD patterns were collected by Bruker D2 phaser diffractometer equipped with a LYNXEYE detector using Cu K_α radiation (1.54184 Å). The 2θ range was set between 10–60° with a step of 0.02°. For paper *II*, the diffraction patterns were recorded on STOE STADI-P diffractometer using a Cu $K_{\alpha1}$ radiation. The measured 2θ range was detected from 10-60° with a scanning rate of 1° min^{-1}. For paper *III* and *IV*, the diffraction patterns were performed on Panalytical X' Pert Alpha 1 using Cu $K_{\alpha1}$ radiation, with the 2θ range from 10 to 70° and 10 to 80°, respectively.

2.5.7 Solid-state nuclear magnetic resonance (NMR)

For paper *I*, magic-angle-spinning (MAS) NMR experiments were performed on Bruker Avance-*III* spectrometer, with a magnetic field at 14.1 T. (^1H, ^{13}C, ^{15}N Larmor frequency of 600.12, 150.92, and 60.83 MHz, respectively) Proton acquisitions involved a rotor-synchronized, double-adiabatic spin-echo sequence with 90° and 1.25 μs excitation pulse pairing 50.0 μs tanh/tan high-power adiabatic pulse (SHAPs) with 5 MHz frequency sweep.[92,93] Directly excited ^{13}C and ^{15}N MAS NMR spectra were recorded with the single-pulse ("Bloch-decay") protocol using a 7 mm probe head and 7 kHz MAS rate. The ^{15}N NMR chemical shifts are reported with respect to nitromethane. All NMR experiments were performed at natural isotope abundance.

2.5.8 Chemical shifts calculations

All calculations were performed with the ORCA code (4.1.2) using a Hartree. Models of different nitrogen in the carbon structure were simulated by

geometry optimization with density functional theory (DFT) OLYP-D3 approximation.[94–97] ^{13}C and ^{15}N nuclear shieldings were calculated by DFT corrected with DSD-PBEP86 approximation and a segmented basis set with electrons included in correlation.[98] Calculated ^{13}C and ^{15}N isotropic nuclear shieldings were converted to ^{13}C and ^{15}N NMR isotropic chemical shifts using gas phase CO_2 and N_2 molecules as secondary references at 125.0 and –75.3 ppm, respectively.[99] Detailed information can be checked in the literature.[100]

2.5.9 Scanning electron microscopy (SEM)

For paper *II*, SEM was performed on Leo Supra 35VP SMT with thermal field emission and on a JEOL JSM-7000F microscope. For paper *III*, CNC/TiO_2-NRs(90) and CNC/TiO_2-NRs(150) were studied by a JEOL-7000F microscope with 15 kV accelerating voltage. For paper *IV*, the topography of CM and CM/$Bi_4O_5Br_2$/BiOBr was evaluated by JEOL JSM-7000F.

2.5.10 Transmission electron microscopy (TEM)

For paper *II*, the morphology of NDC-800 as-obtained sample was recorded by JEOL-2100F at 200 kV accelerating energy. For paper *III*, the TiO_2 nanosheets, nanoseeds and corresponding selected area electron diffraction (SAED) pattern, as well as the high-resolution transmission electron microscopy (HRTEM) images of CNC/TiO_2-NRs(150)/Au NCs were recorded by JEOL-2100F field emission TEM with 200 kV accelerating energy. For paper *IV*, the morphology, HRTEM images and SAED patterns of $Bi_4O_5Br_2$/BiOBr, CM/$Bi_4O_5Br_2$/BiOBr were operated on JEOL-2100F with 200 kV.

2.5.11 Scanning transmission electron microscopy (STEM)

For paper *III* and paper *IV*, STEM and STEM energy dispersive X-ray spectroscopy (EDS) studies were carried out to evaluate the morphology and elemental distribution of hybrid photocatalysts. In detail, for paper *III,* the high-angle annular dark-field (HAADF) STEM micrograph was obtained by JEOL-2100F field emission microscope. For paper *IV*, the EDS analysis of CM/$Bi_4O_5Br_2$/BiOBr was acquired with an aberration-corrected Themis Z (Thermo Fisher) at 300 kV under STEM mode, with moderately low-dose conditions (estimated to be 60 e^-/ Å). The low-dose condition was applied to avoid any potential beam damage on the bio-substrate.

3. Results and discussions

3.1 Electrochemical nitrate reduction with NDC catalysts

Doping carbon materials with nonmetal atoms has attracted attention as one possible way to improve carbon's electronic and chemical properties.[101] It has been reported that the doping of nitrogen can effectively tailor the physiochemical properties of carbon substrates, for example, surface wettability, electron donor properties, conductivity and reactivity.[102–109] Additionally, selective doping of nitrogen atoms in the form of specific nitrogen species is highly important to improve the electrocatalytic properties of different reactions and beneficial for understanding the reaction mechanism with active sites.[110,111] For instance, pyridinic N is considered as the most active catalytic site for oxygen reduction reaction (ORR) among different N species.[110] However, the selectivity of N species or the active site for nitrate reduction reaction (NO_3RR) with NDC materials is still under debate. Herein, NO_3RR was carried out with two types of NDC materials. The selectivity of different N species on NO_3RR is discussed in detail in correlation with understanding the N atoms' position of NDC materials in paper *I*. Furthermore, paper *II* uncovered a potential synthesis route for NDC with renewable natural resources. The cellulose-derived NDC materials show an efficient electrocatalytic performance for NO_3RR. The defective regions containing nitrogen atoms were identified as the active sites for NO_3RR towards NH_3 by DFT calculations.

3.1.1 The characterization of NDC catalysts

The morphology of as-obtained samples was studied by SEM, as shown in Figure 3.1A. It is clear that the modification of HNO_3 resulted in the formation of numerous vast craters on the spherical particles of sample SK. With the treatment of NH_3 on S0 at elevated temperatures, deeper pits can be observed from S0_N. Significantly, the surface of carbon particles in SK_N was cracked after the treatment of HNO_3 and NH_3. The destructed and cracked spheres can potentially be advantageous for the catalytic properties by opening access to the micro and mesopores in the interior of the particles.

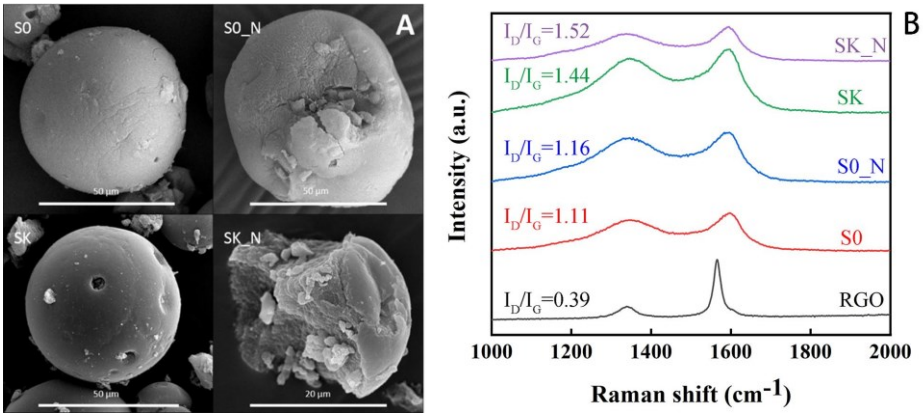

Figure 3.1 (A) SEM images of; and (B) Raman spectra of S0, SK, S0_N, SK_N, and RGO as the baseline. Adapted with permission from paper *I*.[100]

The improved pore system was confirmed by the low-temperature N_2 adsorption, as shown in Table 1. The starting material S0 exhibited over 1200 m^2/g of specific surface area. It should be noted that single activation of HNO_3 did not improve the S_{BET}. Nevertheless, the modification of NH_3 on both S0 and SK showed significant improvement in BET surface area with an appearance of pore size distributions (as high as 2.56 cm^3/g for S0_N).

Table 1. Bulk N content and textural parameters of the pristine and modified mesoporous carbon replicas. Adapted with permission from paper *I*.[100]

Sample	N content [wt%]	S_{BET} [m^2/g]	V_{micro} [cm^3/g]	V_{meso} [cm^3/g]	V_{total} [cm^3/g]
S0	-	1239	0.01	0.52	1.01
S0_N	0.6	1490	0.04	2.03	2.56
SK	2.0	1205	0.01	1.15	1.51
SK_N	3.2	1415	0.01	1.33	1.80

Raman spectroscopy from Figure 3.1 B shows distinct two featured bands at 1340 and 1590 cm^{-1}, which are assigned as the D and G bands, respectively. The D band is associated with the disordered sp^2 hybridized carbon, while the G band arises from the crystalline graphitic carbon.[112] The ratio of the D band and G band (I_D/I_G) was used to evaluate the graphitization degree of porous carbon materials.[113] The baselines were fitted by 2nd Derivative (zeros) method with adjacent averaging smoothing. The peaks were manually added at the wavelength with the local strongest intensity and further fitted by Gaussian functions. The integral of fitted Gaussian peaks was calculated and used for I_D/I_G study. All the samples show a higher I_D/I_G ratio compared with

the reference reduced graphene oxide (RGO), indicating the introduction of defects and disordered structures. These structural defects could be beneficial for electrochemical performance by providing more potential active sites from defects.

The surface chemical compositions of as-prepared samples were determined by XPS, as shown in Table 2, and the quantitative analysis was based on C 1s, O 1s, and N 1s regions. For the oxygen species, the HNO_3 treatment significantly increased the oxygen content, as can be seen from SK compared with S0. However, a drop in oxygen content can be observed from S0 to S0_N, and SK to SK_N, respectively. The reduction in oxygen content was linked to the reducing properties of NH_3.[83] A detailed study of the contents of oxygen and nitrogen species was obtained by deconvolution of XPS O 1s and N 1s spectra (Figure 3.2). Primarily, in the N 1s core region, three central components at 398.9 eV (±0.1 eV), 400.2 eV (±0.1 eV), and 401.6 eV (±0.2 eV) were distinguished as pyridinic, pyrrolic and, quaternary nitrogen, respectively.[104,114] Regarding the modification effects on N content, a

Table 2. Content of O and N species on the surface of carbon materials. Adapted with permission from paper *I*.[100]

	Oxygen species (atom %)					Nitrogen species (atom %)				
sample	C=O	O=C–O	C–O	N–O	total O	pyridinic	pyrrolic	graphitic	oxidized	total N
S0	0.73	1.37	2.44	0.00	4.5					
S0_N	0.51	0.25	1.52	0.00	2.3	0.27	0.22	0.18	0.00	0.7
SK	3.01	4.32	2.49	3.54	13.4	0.17	0.53	0.09	1.81	2.6
SK_N	2.06	0.41	3.16	0.00	5.6	2.40	1.02	0.28	0.00	3.7

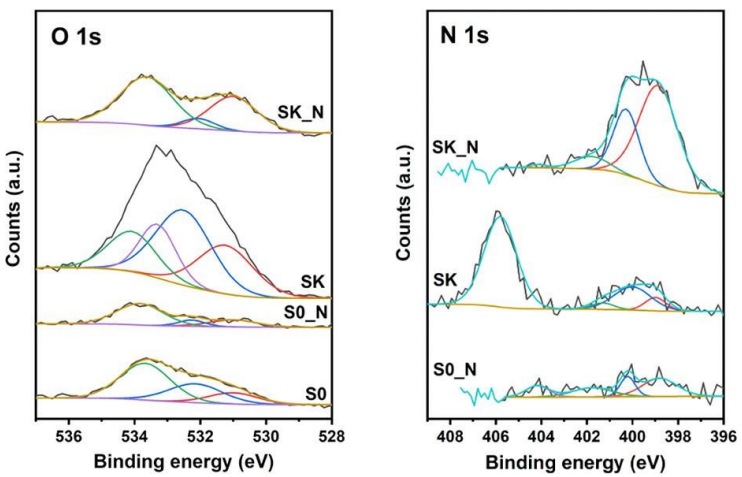

Figure 3.2 XPS O 1s and N 1s spectra of the pristine and modified mesoporous carbon replicas. Reproduced from paper *I*[100] with permission.

significant increase of N content in sample SK can be observed compared with S0, which can be attributed to the modification of HNO_3. Simultaneously,

during the process of NH_3 at elevated temperature on SK, the nitro species were completely reduced, forming mainly pyridinic and pyrrolic N species in SK_N. As a result, it is clear that the treatment of NH_3 efficiently reduced the O and N content in SK_N. The nitrogen species are mainly in the form of pyridinic, pyrrolic and graphitic N content.

3.1.2 Solid-state NMR characterization on SK_N

The XPS analysis provided the pioneer chemical composition information of carbon samples. However, the resolution is limited to further understand the position of N atoms in NDC materials. Herein, solid-state NMR was implemented to obtain more profound insight into the surface composition of the SK_N sample with the help of our collaborator. Direct excitation of the sample at 7 kHz MAS was employed to observe the full ^{13}C and ^{15}N range of the SK_N (Figure 3.3). The ^{15}N MAS NMR spectrum from Figure 3.3b identified two distinct ^{15}N resonances at −74 ppm and −258 ppm. These values fall in the characteristic shift ranges of pyridinic and pyrrolic nitrogen sites.[115] To corroborate the NMR signal assignments, ^{13}C and ^{15}N NMR chemical shifts were calculated with quantum chemistry methods on various structural models. The calculated ^{13}C chemical shift in the graphene model (red line, Figure 3.3a) is in excellent coherence with the experimental values obtained from the SK_N spectrum. As a result, it can be concluded that the graphene local environment represents the majority of carbon atoms, and in the SK_N

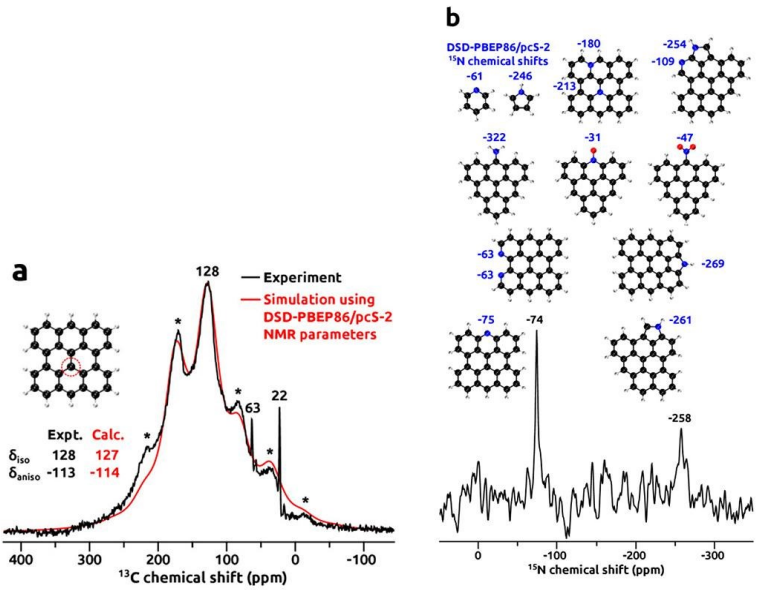

Figure 3.3 Directly excited ^{13}C (a); and ^{15}N (b) MAS NMR spectra of the SK_N sample; together with hypothetical structural motifs chemical shift calculation. Adapted with permission from paper *I*.[100]

sample, the broadening can be attributed to the structural disorder with packing/π-π stacking effects. The simulated nitrogen local environments reported in the literature on NDC materials were constructed and evaluated in Figure 3.3b.[116,117] The experimental ^{15}N spectrum is well aligned with pyridinic nitrogen and pyrrolic nitrogen simulation signals. Specifically, the practical shift at −74 ppm is consistent with pyridinic-N sited at the edge of the carbon sheet with a simulated shift at −75 ppm. On the other hand, the relatively weak and broad resonance at −258 ppm is consistent with the model of pyrrolic nitrogen, which showed a wide resonance range from −254 ppm to −269 ppm. However, the resonance can be solely ascribed to external pyrrolic nitrogen with a calculated shift at –261 ppm. The conclusion derived from solid-state NMR in agreement with XPS further indicates that nitrogen atoms are predominantly present at the edge area of the SK_N sample with a low amount of graphitic nitrogen. Detailed experimental and modelling parameters can be found in paper *I*.

The nitrogen species as well as the precise position of nitrogen atoms in the SK_N were clearly investigated, and this information can be instructive in understanding the active sites in NO_3RR. In particular, the influence of edging nitrogen on the selectivity of nitrate reduction toward either molecular nitrogen or NH_3 was investigated. Herein, the NO_3RR with S0 and SK_N as catalysts were carried out using the methods described in the former session.

3.1.3 Electrochemical removal of nitrates

The LSV curves of Both S0 and SK_N in 0.1 M Na_2SO_4 with the absence and presence of 200 ppm nitrate are shown in Figure 3.4A. A declined geometric current density can be observed when no nitrate was added to the electrolyte. In the presence of nitrate, cathodic peaks in LSV curves drop at −0.9 V vs RHE and −0.8 V vs RHE for S0 and SK_N electrodes. The same trend can be noticed from CA in Figure 3.4B. However, the almost identical current density of −4 mA cm^{-2} at −0.84 V vs RHE suggests no relevant influence of the (i) nitrogen positions within the carbon structure or (ii) the general presence of nitrogen in the carbon samples on the electrocatalytic activity.

To study the selectivity and nitrate reduction efficiency of NDC catalysts, the nitrate, nitrite and NH_3 concentration after a 3 h reaction at −0.84 V vs RHE were studied by the specific method mentioned in section 2, as shown in Table 3. It can be noticed from S0 and SK_N that nitrogen doping can effectively increase the current density. However, the reduction efficiency on NO_3^- are at the same level. Indicating the nitrogen doping potentially be active on HER instead of NO_3RR. In combination with the ^{15}N solid-state NMR at atomic

resolution, the electrochemical results proved that nitrate reduction was independent of the presence and structural positions of the nitrogen atoms in the carbon material. Additionally, nitrogen doping showed no effect on the selectivity of NO_3RR.

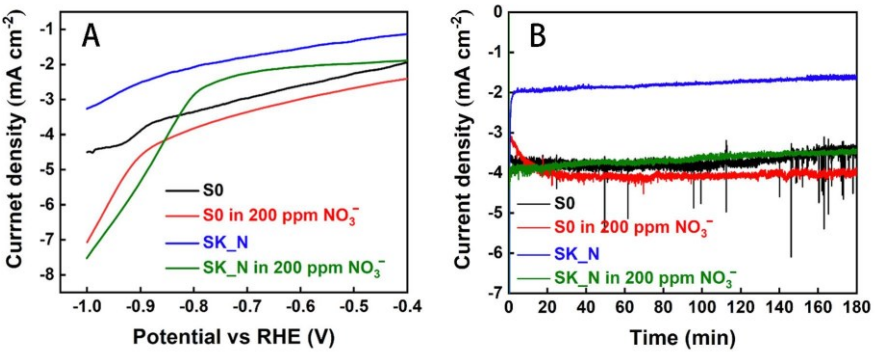

Figure 3.4 (A) LSV curves of S0 and SK_N in 0.1 M Na_2SO_4 with the absence and presence of 200 ppm nitrate; and (B) Constant potential electrolysis of S0 and SK_N at –0.84 V vs RHE in 0.1 M Na_2SO_4 with the absence and presence of 200 ppm nitrate. Adapted with permission from paper *I*.[100]

Table 3. Electrochemical reduction of nitrate with S0 and SK_N electrodes. Adapted with permission from paper *I*.[100]

electrode	CA conditions	initial concentration of NO_3^- (ppm)	final concentration of NO_3^- (ppm)	reduction efficiency of NO_3^- (%)	final concentration of NO_2^- (ppm)	final concentration of NH_4^+ (ppm)	NO_3^- + NO_2^- + NH_4^+ (ppm)
S0	–0.843 V vs RHE	200	105	47.5	5.8	11.0	121.8
SK_N	–0.843 V vs RHE	200	103	48.5	8.4	9.7	121.1

3.2 Electrochemical nitrate reduction with cellulose-derived NDC catalysts

3.2.1 The characterization of cellulose-derived NDC catalysts

In the previous part of the work, the effects of nitrogen species and nitrogen atoms' positions on the catalytic performance of NO_3RR were disclosed. Herein, the impact of defects in NDC materials on NO_3RR towards ammonia was studied. Most importantly, optimized synthesis procedures of NDC in a sustainable direction by using cellulose as the carbon source was proposed.

The cellulose-derived NDC materials were prepared by oxidation and carbonization route, and the as-obtained samples were marked as NDC-500, NDC-600, NDC-700, NDC-800, and NDC-900 according to the carbonization temperature. Detailed information can be found in session two or paper *II*.
The surface area and porosity of as-obtained samples were studied by N_2 adsorption-desorption isotherms (Figure 3.5a), and corresponding information is listed in Table 4. The NDC-800 shows the highest total pore volume and BET surface area among the samples. However, the surface area and porosity decrease at 900℃ can be testified and attributed to the material shrinkage at high temperatures.[118] The observations were supported by the atomic model from carbonization doping reactive molecular dynamics (RMD) simulations with the help of our collaborators. The graphitization degree could be estimated from the simulated planar motifs, and the ratio of graphitic and diamond carbon was 1.44, confirming the dominant graphitic character of the ensemble. Furthermore, the chemical composition of as-obtained samples was studied by elemental analysis, and the results listed in Table 5 showed the materials mainly consisted of C, N and H. Among the samples, an upward trend of C content can be observed with increasing the carbonization temperature from NDC-500 to NDC-800 (71.9–84.0%).On the contrary, a downward trend of N and H was also shown with increasing carbonization temperatures to 800℃. The increase in N on NDC-900 can be explained by the reaction with ammonia at high temperatures.[119,120]

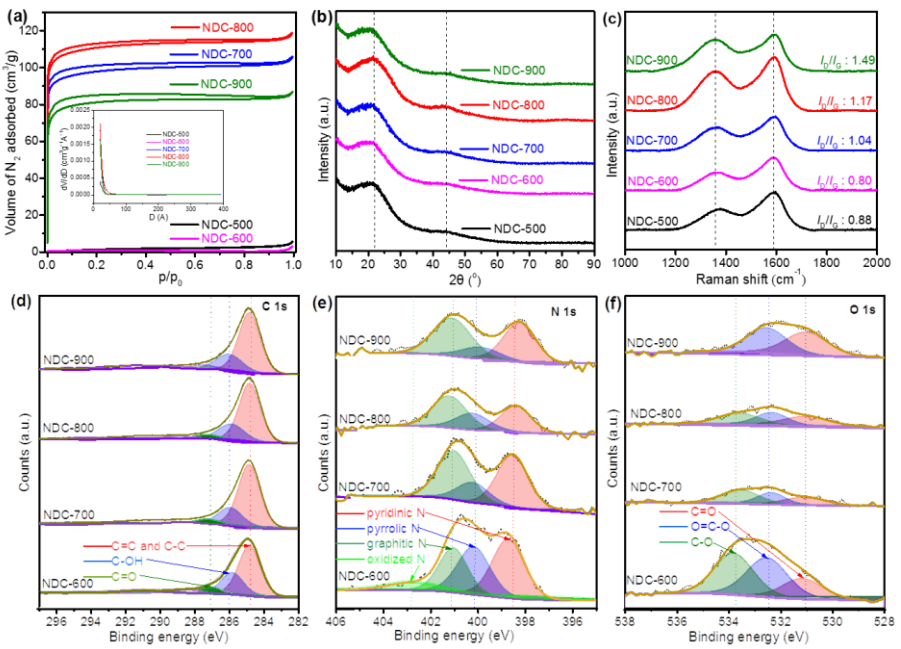

Figure 3.5 (a) N_2 adsorption-desorption isotherms, (b) PXRD patterns and (c) Raman spectra of NDC-500, NDC-600, NDC-700, NDC-800 and NDC-900

materials; XPS (d) C 1s, (e) N 1s and (f) O 1s spectra of as-prepared materials. Reproduced from paper *II*[121] with permission.

The structure was further characterized by PXRD, as shown in Figure 3.5b. The PXRD pattern presents typical graphite (002) facets and carbon (101) facets with broad diffraction features at 23°and 44°, respectively.[122] Raman spectroscopy (Figure 3.5c) captured a trend of higher I_D/I_G ratio upon increasing the carbonization temperature, whilst NDC-900 showed the highest I_D/I_G ratio at 1.49, implying the highest defects and disordered structures among the samples. XPS further disclosed the surface composition of the as-prepared materials, as shown in Figure 3.5d–f. The XPS suggested the resultant pyrrolic N species decreased while total graphitic and pyridinic N increased with the elevated carbonization temperature. Graphitic N and pyridinic N have been proven to exhibit excellent stability and have been considered as efficient active sites.[109,123]

Table 4. Porosity of the five NDC materials after carbonation at different temperatures. Adapted with permission from paper *II*.[121]

Sample	S_{BET} [m^2/g]	$S_{Langmuir}$ [m^2/g]	V_{micro} [cm^3/g]	V_{meso} [cm^3/g]	V_{total} [cm^3/g]
NDC-500	6	12	0.001	0.006	0.009
NDC-600	3	5	0.001	0.001	0.005
NDC-700	357	437	0.017	0.136	0.164
NDC-800	413	494	0.019	0.154	0.184
NDC-900	304	362	0.012	0.113	0.135

Table 5. C, H and O contents in NDC materials. Adapted with permission from paper *II*.[121]

Sample	C%	N%	H%
NDC-500	71.9	8.0	3.6
NDC-600	76.5	9.0	2.6
NDC-700	82.4	7.7	1.8
NDC-800	84.0	5.7	1.4
NDC-900	82.1	6.3	1.4

3.2.2 Electrochemical removal of nitrates

It can be concluded that the carbonization temperature affects the NDC structure from the structural characterization. Then, the structure-property relationship can be identified by comparing the electrochemical nitrate reduction experimental activities. The electrodes for electrochemical NO_3RR were prepared with cellulose-derived NDC samples with the method mentioned in section 2. Then, the electrochemical NO_3RR was carried out in 0.1 M Na_2SO_4 electrolyte with 100 ppm NO_3^-. The LSV curves of five NDC materials are depicted in Figure 3.6a. Among the electrodes, NDC-800 achieved the highest electrocatalytic activity. The as-prepared NDC-800 electrode also showed the highest HER activity at negative potentials and the most significant oxygen evolution reaction (OER) activity at positive potentials in 0.1 M NaOH electrolyte (Figure 3.7). Figure 3.6b depicted the NH_4^+ Faradaic and NO_3^- reduction efficiencies of five samples studied under a condition of 2 h CA at −1.5 V vs. Ag/AgCl. The NDC-800 showed the highest NH_4^+ Faradaic and NO_3^- reduction efficiencies.
From the electrochemical performance in Figure 3.6a, b referring to the structural information of the samples, it can be speculated that the outstanding activity of NDC-800 for NO_3RR is related to the high microporosity with a substantial number of active sites rather than a higher amount of nitrogen. As a result, the ammonolysis at 800 °C can create an optimum NDC structure for an efficient electrochemical NO_3RR to ammonia.

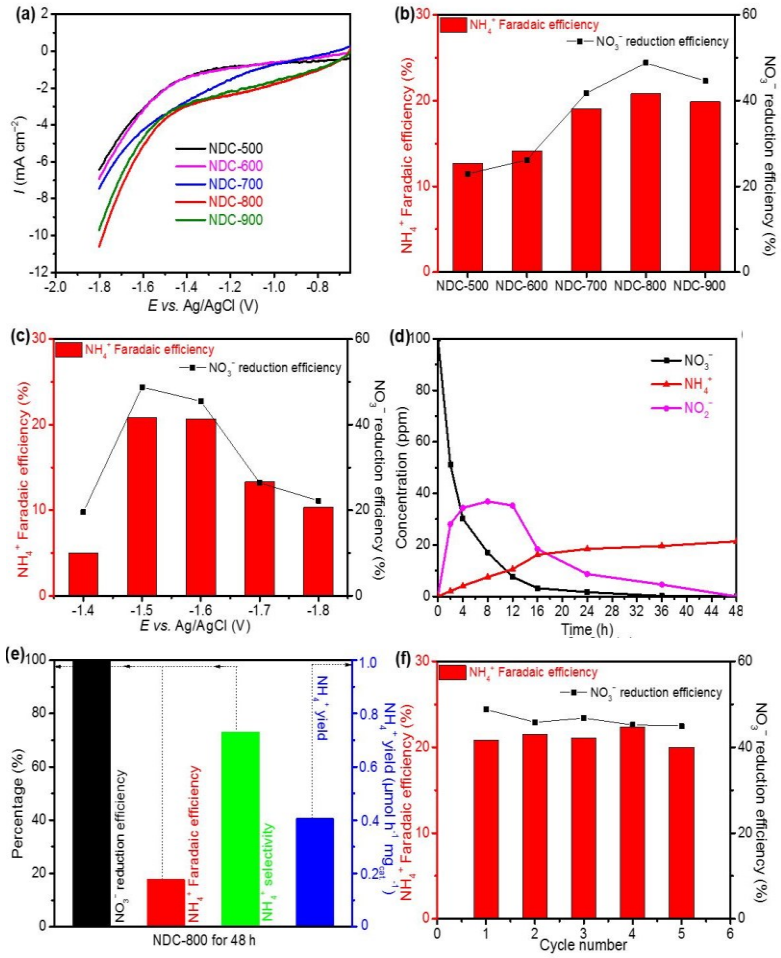

Figure 3.6 (a) LSV curves of NDC-500, NDC-600, NDC-700, NDC-800 and NDC-900 for the NO_3RR; (b) NH_4^+ Faradaic and NO_3^- reduction efficiencies of NDC-500, NDC-600, NDC-700, NDC-800 and NDC-900 at −1.5 V *vs.* Ag/AgCl for 2 h CA; (c) NH_4^+ Faradaic and NO_3^- reduction efficiencies of NDC-800 at various applied potentials for 2 h CA; (d) time-dependent concentrations of NO_3^-, NO_2^- and NH_4^+ over NDC-800 CA at −1.5 V *vs.* Ag/AgCl; (e) NO_3^- reduction efficiency, NH_4^+ Faradaic efficiency, NH_4^+ selectivity and NH_4^+ yield of NDC-800 at −1.5 V *vs.* Ag/AgCl for 48 h CA; (f) NO_3^- reduction and NH_4^+ Faradaic efficiencies of NDC-800 at −1.5 V *vs.* Ag/AgCl for 2 h CA after consecutive recycling test. Measurements were performed in a 0.1 M Na_2SO_4 aqueous electrolyte with 100 ppm of NO_3^-. Adapted with permission from paper *II*.[121]

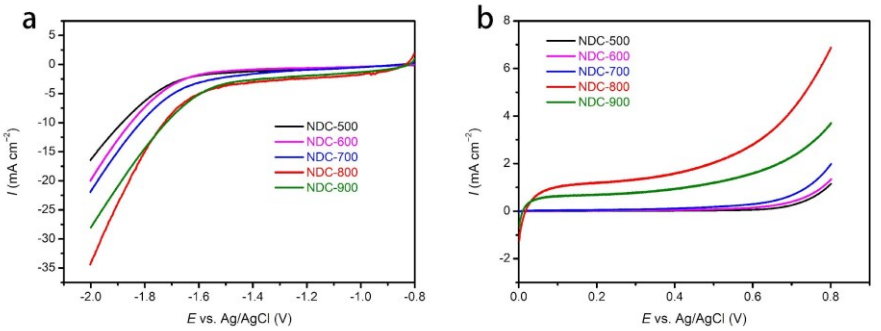

Figure 3.7 (a) LSV curves of NDC-500, NDC-600, NDC-700, NDC-800 and NDC-900 for HER in a 0.1 M NaOH (pH 13) electrolyte; and (b) LSV curves of NDC-500, NDC-600, NDC-700, NDC-800 and NDC-900 for OER in a 0.1 M NaOH (pH 13) electrolyte. Adapted with permission from paper *II*.[121]

Then, this thesis further identified the optimum potential of NDC-800 for the catalytic activity by applying constant potentials at −1.4, −1.5, −1.6, −1.7, and −1.8 V vs. Ag/AgCl for 2 h CA (Figure 3.6c). Both NH_4^+ faradaic efficiency and NO_3^- reduction efficiencies peaked at −1.5 vs. Ag/AgCl within a volcanic shape curve due to the effects of competitive reactions, such as HER and nitrite reduction reaction (NO_2RR). Then, a long-term 48 h reaction was carried out at the optimum voltage, −1.5 V vs. Ag/AgCl, and the time-dependent NO_3^-, NO_2^-, and NH_4^+ concentrations were studied at 2, 4, 8, 12, 16, 24, 36, and 48 h (Figure 3.6d). The decay rate of NO_3^- reached nearly 100% after 48 hours, while the intermediate by-product NO_2^- concentration increased first but completely electrochemically reduced to NH_4^+ after 48 h. After a 48h reaction, the NDC-800 sample showed 17.8% of NH_4^+ faradaic efficiency, 73.1% of NH_4^+ selectivity and 0.42 μmol h^{-1} $mg_{cat.}^{-1}$ of NH_4^+ yielding rate (Figure 3.6e). All the electrochemical performances suggested that NDC-800 exhibits high selectivity toward ammonia with excellent reduction efficiency in NO_3RR.

Additionally, the stability of NDC-800 was estimated by consecutive recycling tests with the same experiment condition and electrode. A 2 h CA at −1.5 V vs. Ag/AgCl in a 0.1 M Na_2SO_4 electrolyte with 100 ppm NO_3^- was carried out for each cycle. Notably, as can be seen from Figure 3.6f, the NH_4^+ faradaic efficiency and NO_3^- reduction efficiencies showed only a slight fluctuation but no apparent performance sluggish. These results imply good catalytic stability during the NO_3RR for the NDC-800 catalyst.

The source of nitrogen in ammonia is critical for NO_3RR. Herein, the source of nitrogen was proved by comparing a test control experiment with and without NO_3^-. As shown in Figure 3.8a, the electrochemical NO_3RR measured in a blank electrolyte yielded a negligible concentration of NH_4^+. Meanwhile,

^{15}N isotope labelling ^{1}H NMR spectra was performed to verify the source of nitrogen further. The ^{1}H NMR spectra of the electrolyte after NO_3RR with $Na^{15}NO_3$ at –1.5 V vs. Ag/AgCl for 2 h show typical double peaks of $^{15}NH_4^+$, which is different from the typical triple peaks of $^{14}NH_4^+$ from the 1H NMR spectra with $Na^{14}NO_3$ as reactants.[124]

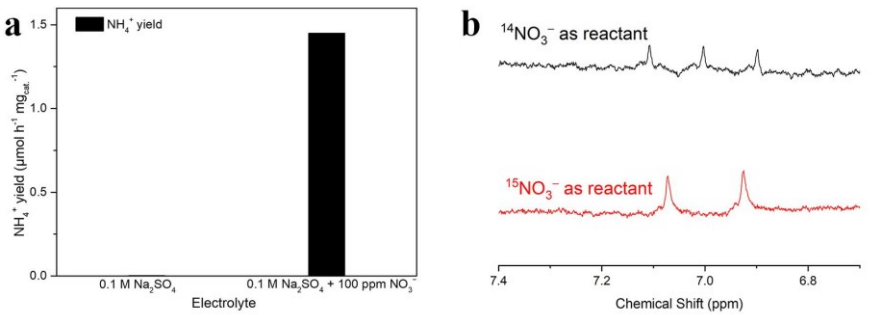

Figure 3.8 (a) NH_4^+ yield of NDC-800 in 0.1 M Na_2SO_4 electrolyte with and without 100 ppm NO_3^- for 2 h CA; (b) ^{1}H NMR spectra of the electrolyte after electrocatalytic NO_3RR using $^{15}NO_3^-$ and $^{14}NO_3^-$ as the nitrogen source. Adapted with permission from paper *II*.[121]

3.2.3 Reaction mechanisms deduced by multi-scale calculations

The DFT calculations start from the RMD supramolecular model with the help of our collaborators. Detailed information can be found in paper *II*. The analysis of corresponding energy profiles identifies the potential reaction pathway at −1.5 V vs. Ag/AgCl accompanied by eight proton/electron transfers. Figure 3.9 shows the detailed steps of NO_3RR towards NH_3 and the corresponding configuration. Notably, the initially two O atoms of HNO_3 showed a strong interaction with the defects and dissociated nitric acid to NO spontaneously, which does not directly interact with the surface. Simultaneously, the O atom and OH group anchored to the defect borders, as can be seen from step 1. Then, adding a proton/electron pair leads to releasing water molecules (step 2). Subsequently, the oxygen atom firmly bound to the defect generates a second water molecule by adding two further proton/electron pairs as in steps 3 and 4 with an uphill variation. From configuration 5, NO adsorption occurred first, followed by an N-first mechanism. In detail, NO adsorbed two H atoms, resulting in the adsorbed HNO and H_2NO species; step 6 is energetical downhill followed by a relatively low limiting potential. Further proton/electron addition results in the formation of ammonia and an adsorbed O atom from step 8. The reaction in steps 9 and 10 for the generation of the water molecule is very similar to steps 3 and 4 but with a decreased limiting potential of about −0.8 eV.

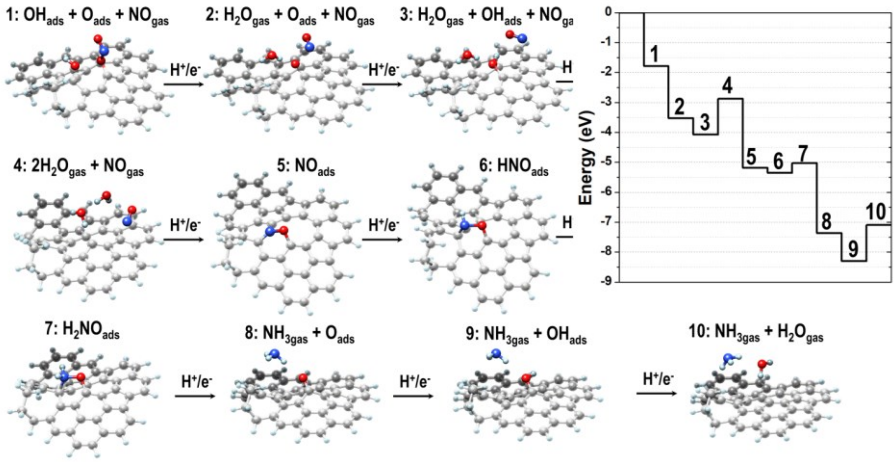

Figure 3.9 Energy profile of the NO_3RR mechanism leading to the formation of NH_3 and three water molecules and the corresponding configurations. C gray, N blue, O red, H light blue. Reproduced from paper *II*[121] with permission.

A defect borders modified mechanism was proposed by inserting a nitrogen atom, which can decrease (in absolute value) the limiting potential of such a step to about −0.6 eV. The reduction proceeds were simulated by considering the adsorption of NO on the defective region's most strongly interacting carbon atom (the atom with only two first neighbours). It should be critical that both N atom and O atom can achieve the adsorption; thus, predicting the possible reaction pathways were complicated. The mechanism through O atom adsorption was discussed above. The discussion and reaction mechanism *via* the N atoms as O-distal, O-alternating, N-distal, and N-alternating can be found in paper *II*.

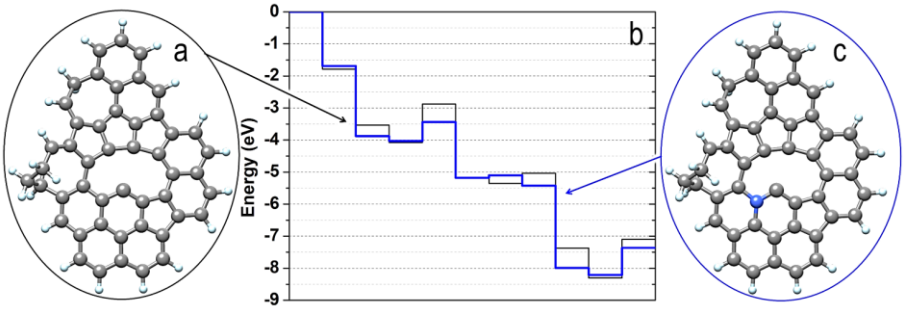

Figure 3.10 (a) Structure of the bare defect sampled as the catalytic site in the mechanism shown in Figure 3.9; (b) energy profiles for the NO_3RR mechanism characterizing site (a) and (c); (c) same structure of panel (a)

where one C atom next to the defect border has been replaced with a nitrogen atom. Reproduced from paper *II*[121] with permission.

It should be clarified that the mechanism proposed above does not show the precise topology of the defect as the only candidate for promoting NO_3RR. Instead, the localized defects' limiting potentials involved mechanisms agree with the experimental onset potentials. As a result, it can be concluded that the defective regions containing N atoms can modulate the catalytic performance of the neighbouring sites. Furthermore, it could be speculated that the active site can not only bind oxygen or nitrogen but also optimize the reaction pathway and hinder the by-products reaction.

3.3 Cellulose nanocrystal supported TiO_2 with Au NCs decoration

Hybrid bio-inorganic materials are promising for energy and environmental applications that simultaneously enable green degradation toward a circular economy.[125] CNCs with high surface area, tuneable surface charge and functional groups have been considered promising building blocks for water purification. Recently, CNCs-TiO_2 interfaces have drawn much attention to photocatalytic water treatment. However, the main drawback of TiO_2 is the wide electronic band gap (3.0–3.2 eV) which confines the application of CNCs-TiO_2 in the UV region.[126–128] Surface modification with plasmonic nanostructures, such as Au, can strongly enhance photocatalytic activity in the visible light region. In this part of the thesis, CNCs substrate was applied for *in situ* growth of TiO_2 nanomaterials with further decoration with Au nanocrystals. The hybrid material showed excellent photocatalytic dye degradation performance under simulated solar light illumination.

3.3.1 Converting CNCs into photocatalysts

Seed-mediated synthesis is a common method for binary metal oxide synthesis; however, TiO_2 usually requires high annealing temperatures above 500 °C. The high annealing temperature is essential to achieve sufficient crystallinity/orientation in promoting low dimensional crystal growth. The TGAs from Figure 3.11 indicated none of the functionalized CNCs can maintain its structure above 500 °C annealings, which also has been reported in the literature.[129] Thus, to avoid destroying the CNCs substrate, a mild TiO_2 growth routine was achieved. Initially, the TiO_2 seeds (30 nm of mean particle

size) were synthesised on CNCs with the sol-gel method by slowly hydrolysing $Ti(OBu)_4$,

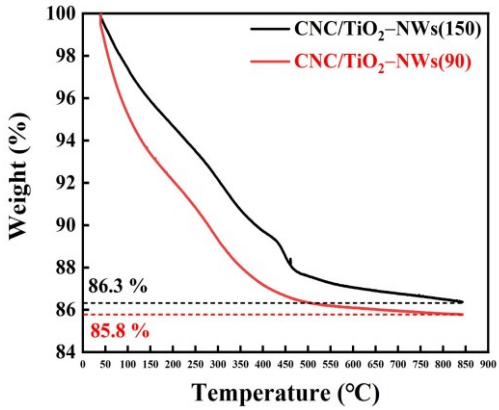

Figure 3.11 TGA curves of the CNC/TiO_2-NRs (90), CNC/TiO_2-NRs(150) (ramp 10 ºC/min, 35–850 ºC, in air. Reproduced from paper *III*[130] with permission.

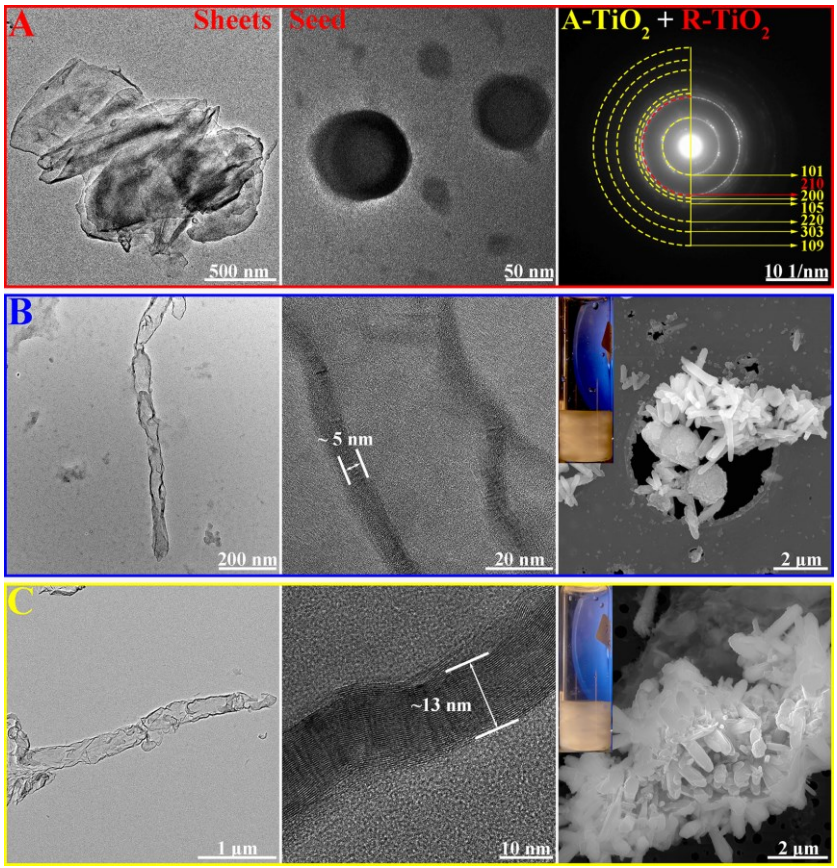

Figure 3.12 TEM images of (A) TiO_2 nanosheets, nanoseeds and corresponding SAED pattern of TiO_2 nanoseeds, (B) TEM images of TiO_2-NRs(90) and HRTEM image of the walls of TiO_2 NRs (90), SEM images of CNC/TiO_2-NRs(90) and the flow birefringence of the hybrid (inset) (C) TEM image of TiO_2-NRs(150) and HRTEM image of the boundary of TiO_2 NRs (150), SEM images of CNC/TiO_2-NRs(150) and the inset image showing the birefringence of the hybrids. Reproduced from paper *III*[130] with permission.

followed by ageing at 50 ℃ to achieve sufficient crystallinity. As shown in Figure 3.12A, the SAED pattern indicates the polycrystalline particles crystallize with mixed phases of predominately anatase-TiO_2 with a detectable rutile phase. In the following step, the seed-coated CNCs were exposed to two media, resulting in two different growth mechanisms. Low temperatures growth was carried out at 90 ℃ with conc. HCl and water with $TiCl_4$. As can be seen from the HRTEM images in Figure 3.12B, the low-temperature synthesised TiO_2 NRs have an average length of 1.5 μm and 48 nm in diameter. The second route of growth was implemented at 150 ℃ in an autoclave. The as-obtained NRs had 250 nm diameter and >2 μm length (Figure 3.12C). Detailed information can be found in paper *III*. The loading amounts of TiO_2 were defined at around 86% for CNC/TiO_2-NRs by TGA analysis from Figure 3.11.

PXRD was carried out to confirm the phase information of CNC/TiO_2-NRs(90) and CNC/TiO_2-NRs(150). As shown in Figure 3.13A, the CNC showed characteristic reflections of cellulose *I* at 15.4 ° and 22.6 °.[85] From the PXRD pattern of as-obtained samples, it can be concluded that the CNC/TiO_2-NRs(90) show a higher degree of crystallinity dominated by the anatase phase; and CNC/TiO_2-NRs(150) sample shows a higher degree of rutile phase than anatase phase. Raman patterns in Figure 3.13B supported the phase information of two as-obtained samples. The existence of the anatase phase can be confirmed with the appearance of a sharp peak at 147 cm^{-1} and the shoulders at 192 cm^{-1}, 624 cm^{-1} for CNC/TiO_2-NRs(90). For CNC/TiO_2-NRs(150), the rutile phase can be confirmed with peaks at 238 cm^{-1}, 438 cm^{-1}, and 604 cm^{-1}.

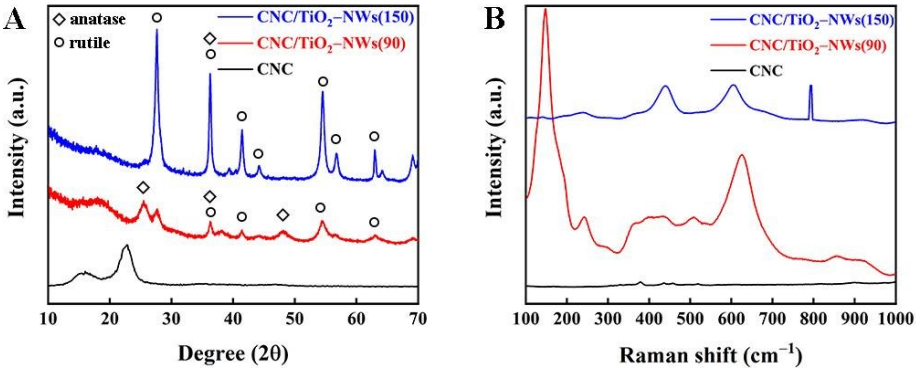

Figure 3.13 (A) XRD patterns of CNC, CNC/TiO_2-NRs(90) and CNC/TiO_2-NRs(150) and (B) Raman patterns of CNC, CNC/TiO_2-NRs(90) and CMC/TiO_2-NRs(150). Adapted with permission from paper *III*.[130]

TiO_2 offers many advantages, such as chemical inertness, cost-effectiveness, non-toxicity and long-term stability.[131–133] However, as mentioned, the wide electronic band gap confines the application of C NC/TiO_2-NRs(90) and CNC/TiO_2-NRs(150) in the UV region. In this work, surface decoration with plasmonic Au NCs has been applied to expand the light adsorption performance into the visible light region via the LSPR effect.[134–136]

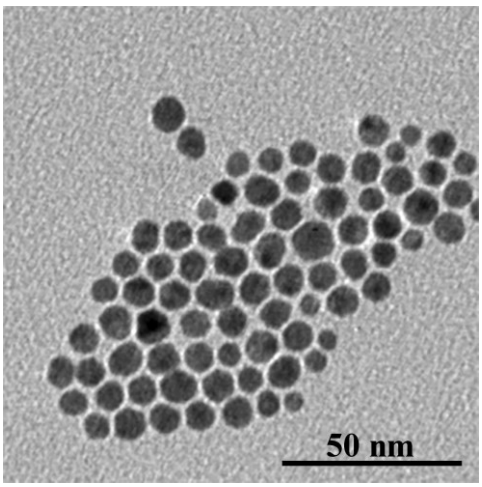

Figure 3.14 TEM image of Au NCs. Reproduced from paper *III*[130] with permission.

The CNC/TiO_2-NRs(90)/Au NCs and CNC/TiO_2-NRs(150)/Au NCs were prepared with the method mentioned in section 2. The mean particle size of the Au NCs before the deposition was 8 nm, as shown in Figure 3.14. The surface characteristic and elemental maps of Au decorated hybrids were studied by TEM and STEM EDS.

The HAADF STEM micrograph from Figure 3.15B reveals the deposition of Au NCs with an 8–40nm diameter. The vast size distribution can be attributed to the aggregation of the monodispersed Au NCs. Additionally, the spatial elemental distribution was performed by EDS mapping, as shown in Figure 3.15C. The Au NCs are well distributed along the TiO_2 NRs.

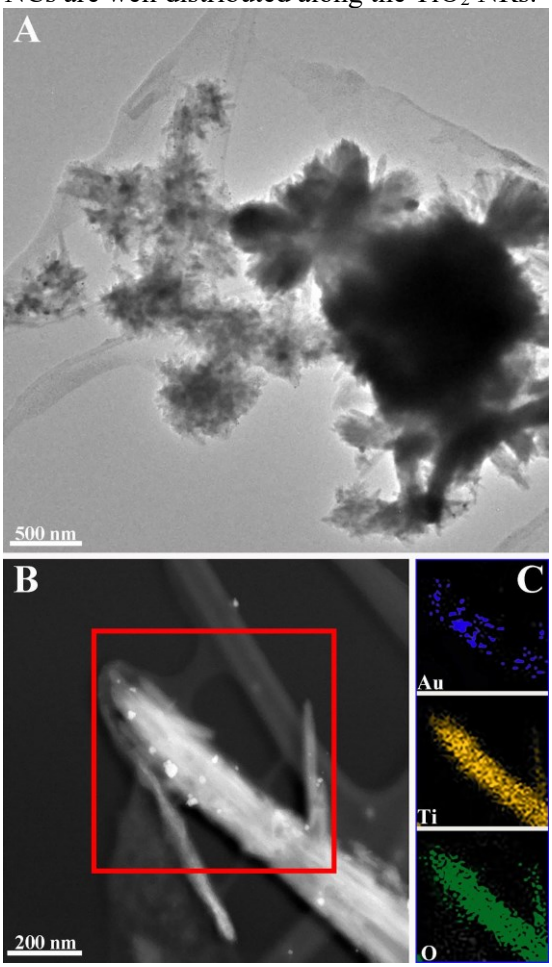

Figure 3.15 TEM images of Au NCs deposited TiO_2-NRs(150): (A) morphology of CNC/TiO_2-NRs(150)/Au NCs; (B) HAADF STEM micrograph of TiO_2-NRs(150)/Au NCs and corresponding (C) EDS mapping of Au, Ti and O. Reproduced from paper *III*[130] with permission.

3.3.2 Photocatalytic performance of CNC/TiO_2-NRs(90)/Au NCs and CNC/TiO_2-NRs(150)/Au NCs

Subsequently, the optical properties of CNC/TiO_2-NRs(90), CNC/TiO_2-NRs(150), CNC/TiO_2-NRs(90)/Au NCs and CNC/TiO_2- NRs(150)/Au NCs

were characterized by UV-VIS spectroscopy (Figure 3.16). The broad absorption peaks in the range of 500–600 nm are attributed to the LSPR effect.[137,138] The broadening originated from 1) the wide size distribution of Au NCs and 2) the intercoupling of Au NCs.[137–139]

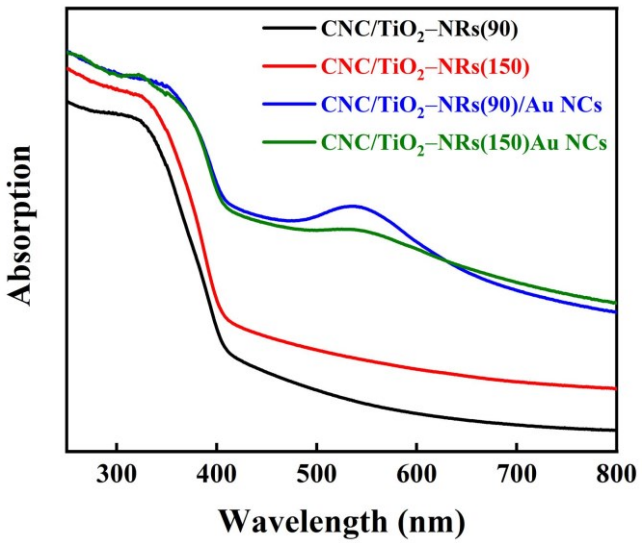

Figure 3.16 UV-Vis light absorption spectra of CNC/TiO_2-NRs(90), CNC/ TiO_2-NRs(150), CNC/TiO_2-NRs(90)/Au NCs and CNC/TiO_2-NRs(150)/Au NCs. Reproduced from paper *III*[130] with permission.

The band gaps of as-prepared samples were estimated with the Tauc plot (Figure 3.17), i.e. the band gap can be extracted from the $(\alpha h\upsilon)^{1/n}$ vs $h\upsilon$ plot intercept.[140] In which the n value was selected as ½ for the rutile phase. Furthermore, the Kubelka-Munk function (K-M) was substituted for α in the calculation.[141,142] Therefore, the band gap of CNC/TiO_2-NRs(90), CNC/TiO_2-NRs(150), CNC/TiO_2-NRs(90)/Au NCs and CNC/TiO_2-NRs(150)/Au NCs was estimated to be 3.15 eV, 2.98 eV, 3.11 eV and 3.00 eV, respectively as shown in Figure 3.17. As a result, the decoration of Au NCs can slightly decrease the band gaps of CNC/ TiO_2-NRs hybrids. The reduced band gap indicates improved light absorption toward larger wavelengths, matching the experimental results. The promoted light absorption properties were performed by RhB degradation under solar light simulator illumination.

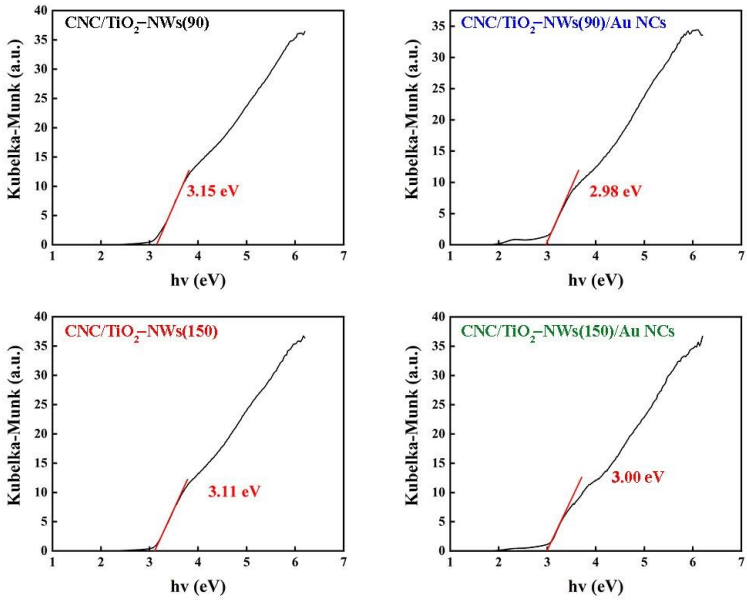

Figure 3.17 Tauc plot images of CNC/TiO_2-NRs(90), CNC/TiO_2-NRs(150), CNC/TiO_2-NRs(90)/Au NCs and CNC/TiO_2-NRs(150)/Au NCs. Reproduced from paper *III*[130] with permission.

The RhB degradation experiment was implemented following the procedures in section 2. H_2O_2 was used as an electron scavenger which can also help with the formation of reactive oxygen species. As a result, the RhB degradation under simulated sunlight with adding H_2O_2 was set as the baseline, as shown in Figure 3.18. Photocatalytic activities of different samples were studied in the same condition with adding H_2O_2 with an initial concentration of RhB at 8 ppm. The results proved that the Au NCs decoration of hybrid catalysts could ameliorate the CNC/TiO_2-NRs.

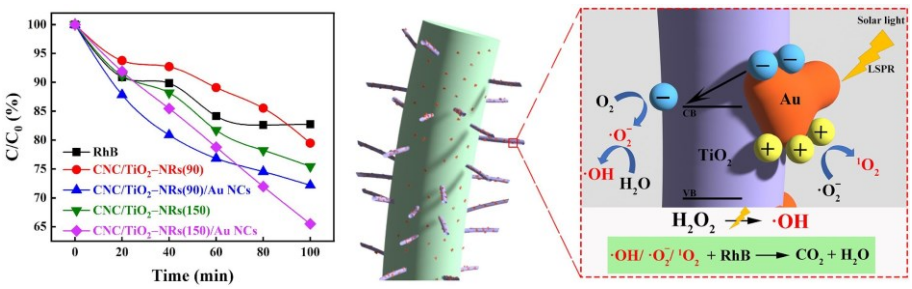

Figure 3.18 Photodegradation of RhB (8 ppm in 50 ml of aqueous solution) under simulated sunlight on different photocatalysts (200 mg, powder) supported by H_2O_2; and corresponding RhB photodegradation mechanism. Adapted with permission from paper *III*.[130]

The possible mechanisms for the plasmon-enhanced CNC/TiO_2-NRs photocatalysts are shown in Figure 3.18. During the solar simulator illumination, LSPR-induced hot electrons in Au NCs on the surface of TiO_2 NRs with energies higher than the Schottky barrier energy can jump into the CB of TiO_2.[143] This process significantly promotes the separation of electron-hole pairs. The injected electrons in CB are trapped by absorbed O_2 molecules and then participate in the photoreduction reaction to get $\cdot O_2^-$. However, $\cdot O_2^-$ is relatively unstable in an aqueous solution, so it would readily decompose into hydroxyl radicals.[144,145]

$$O_2 + e^- \rightarrow \cdot O_2^-$$

$$\cdot O_2^- + 2H^+ + 2e^- \rightarrow \cdot OH + OH^-$$

After the transfer of hot electrons, the holes on Au NCs are supposed to participate in a photo-oxidation reaction with superoxide anion radicals $\cdot O_2^-$, yielding singlet oxygen ($^1O_2$).[146]

$$\cdot O_2^- + h^+ \rightarrow {}^1O_2$$

The photolysis of hydrogen peroxide in aqueous to hydroxyl radicals happened simultaneously, following the reaction:

$$H_2O_2 + hv \rightarrow 2\cdot OH$$

Finally, the reactive oxygen species, including $\cdot OH$, $\cdot O_2^-$ and $^1O_2$, can quickly degrade RhB into CO_2 and H_2O.[147,148]

3.4 Cellulose-bismuth oxybromide membrane for water purification

Mixed-anion bismuth compounds BiOX (X=Cl, Br, I) are two-dimensional layered semiconductors whose charge carrier separation can be improved by the use of semiconductor heterostructures.[102,103] BiOBr is a typical p-type semiconductor that displays high chemical stability under photocatalytic reactions.[149–154] The lamellar structure ensures BiOBr high charge carrier separation efficiency compared to bulk materials.[83,155–159] Bismuth oxybromides are commonly used to combine with BiOBr to form heterostructures, as discussed in the literature.[160–162] In this part of the work, the fabrication of a bioinorganic hybrid that combines photocatalytic

performance with adsorption activity is reported. Cellulose was functionalized as a substrate for $Bi_4O_5Br_2$/BiOBr photocatalyst growth.

3.4.1 Converting cellulose into photocatalysts with $Bi_4O_5Br_2$/BiOBr deposition

The phase of the as-obtained samples without cellulose membrane (CM) was characterized by XRD, as shown in Figure 3.19. The patterns of BiOBr (JCPDS-01-085-0862) and $Bi_4O_5Br_2$ (JCPDS-37-0699) were simulated to confirm the phase of the composite.

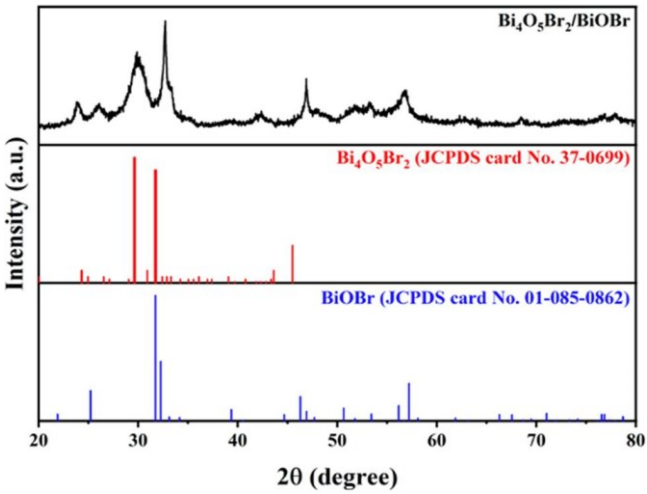

Figure 3.19 Comparison of experimental and simulated PXRD patterns of synthesised photocatalyst without nanocellulose. Reproduced from paper *IV*[91] with permission.

The successful functionalization of CM with a two-dimensional photocatalyst was confirmed by SEM, as shown in Figure 3.20. Figure 3.20a, b depicted the original CM with intergrown fibres. The synthesis of CM-supported photocatalyst was described in section 2. Figure 3.20c, d clearly shows the bioinorganic interface, which verified the successful growth of a two-dimensional photocatalyst on CM.

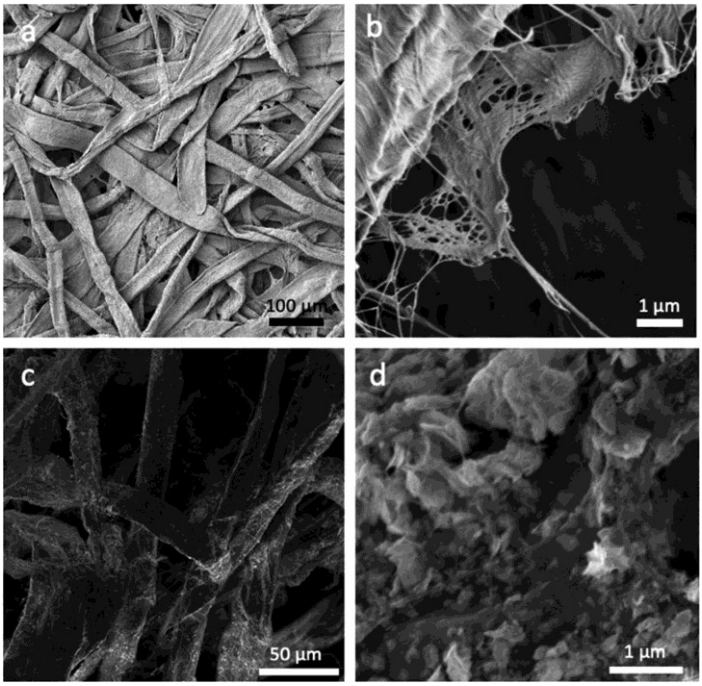

Figure 3.20 SEM micrographs of (a,b) pristine CM and (c,d) hybrid membranes CM/$Bi_4O_5Br_2$/BiOBr. Reproduced from paper *IV*[91] with permission.

Figure 3.21 summarizes the TEM analysis performed for $Bi_4O_5Br_2$/BiOBr and CM/$Bi_4O_5Br_2$/BiOBr. Figure 3.21a–c depicts the as-obtained $Bi_4O_5Br_2$/BiOBr containing a monodisperse mixture of crystalline nanosheets with an average size of 10 nm. The SAED pattern of pristine nanosheets suggests that the BiOBr is the dominant phase. The HRTEM and SAED patterns of CM/$Bi_4O_5Br_2$/BiOBr are shown in Figure 3.21d, e. Figure 3.21d showed a clear morphology of cellulose-supported $Bi_4O_5Br_2$/BiOBr, which was confirmed simultaneously by the SAED pattern.

The STEM EDS analysis was carried out under moderately low-dose conditions (~ 60 e^-/Å) to minimize any potential beam damage on the cellulose substrate. The HAADF survey presents an overview micrograph of an agglomerate containing suspected cellulose coated with $Bi_4O_5Br_2$/BiOBr. The yellow box highlighted the region for the HAADF scan, from which the individual lattice fringes can be observed. The EDS maps of C, O, Br and Bi are shown in Figure 3.21h but with very few counts due to the low probe current. An estimate for the missing counts was obtained by employing a solid smoothness assumption with the help of my co-supervisor. The spectral dimension of the hyperspectral data cube was convolved with a Gaussian kernel prior to integration under EDS peaks. The maps were blurred along spatial dimensions resulting in precise localization of Bi and Br on

agglomerate next to cellulose. The average EDS spectrum from each pixel is presented in Figure 3.21h, the C peak originated from the grid supporting film, and Cu arose from the grid.

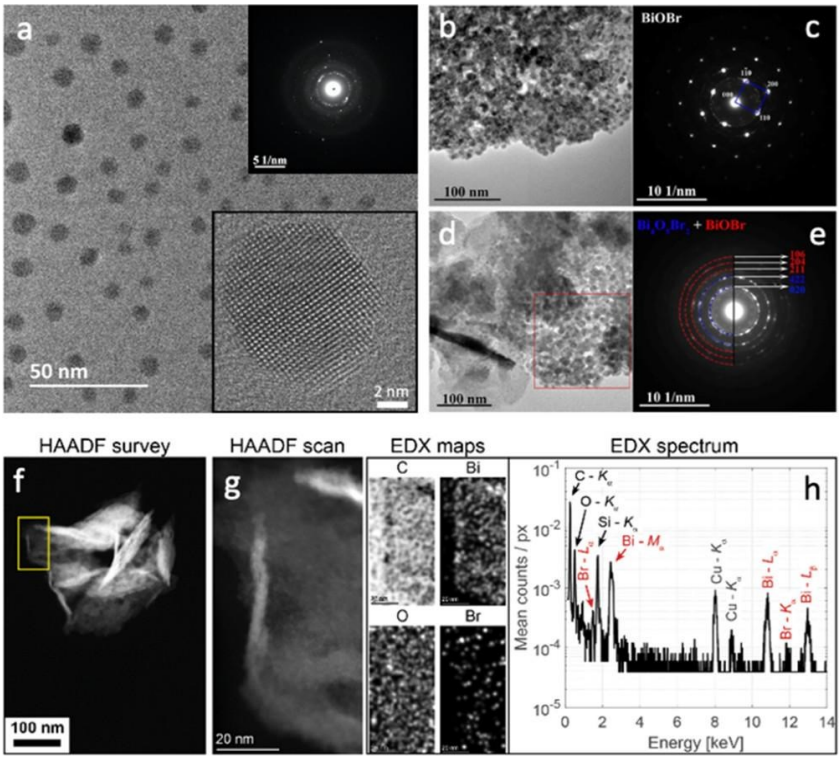

Figure 3.21 (a) Overview TEM image of $Bi_4O_5Br_2$/BiOBr nanosheets. The inset shows a high magnification of the nanosheets in the ED patterns. (b,c) TEM images and corresponding SAED patterns for $Bi_4O_5Br_2$/BiOBr nanosheets and (d-e) CM/$Bi_4O_5Br_2$/BiOBr. (f) HAADF survey of CM/$Bi_4O_5Br_2$/BiOBr and (g) selected area for elemental mapping. Note the cellulose fibre wrapped within agglomerated sheets of the inorganic counterpart. (h) STEM EDS elemental map for CM/$Bi_4O_5Br_2$/BiOBr. Reproduced from paper *IV*[91] with permission.

The XPS determined the surface composition of CM/$Bi_4O_5Br_2$/BiOBr (Figure 3.22). The most intensive signals of C−O and O−C−O from C1s correspond to the cellulose glucose units. Most importantly, the Bi 4f analysis proved the growth of $Bi_4O_5Br_2$/BiOBr: $Bi_4O_5Br_2$ is manifested by the doublet at 158.7 eV (4f 7/2) and 164.1 eV (4f 5/2), whereas the photoemission confirms BiOBr at 159.5 eV (4f7/2) and 164.9 eV (4f 5/2).[163,164] The pentavalent Bi can also be observed and originate from the surface region.

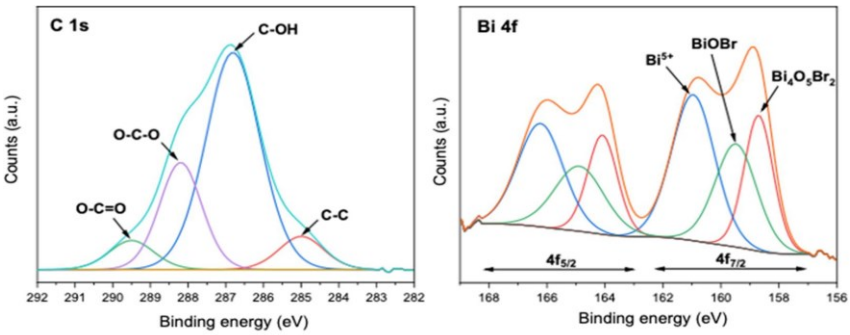

Figure 3.22 XPS spectra of CM/ $Bi_4O_5Br_2$/BiOBr membrane. Adapted with permission from paper *IV*.[91]

3.4.2 Photocatalytic performance of CM/$Bi_4O_5Br_2$/BiOBr

The RhB degradation experiment was carried out with the procedures described in the experimental part with 405 nm (20 W) lamp illumination. The RhB with hydrogen peroxide was set as the baseline. The RhB photodegradation with $Bi_4O_5Br_2$/BiOBr and CM was implemented separately with the same condition to investigate the comprehensive photocatalytic activities of different materials. The pure cellulose membrane slightly decreases the concentration of dye in the solution and can be attributed to the sorption capacity of cellulose toward organic substances (Figure 3.23). The bare $Bi_4O_5Br_2$/BiOBr show a similar degradation performance with cellulose membrane. However, CM/$Bi_4O_5Br_2$/BiOBr show a superior RhB degradation performance under light illumination, reaching almost 100 % removal in 100 min, indicating a synergistic effect between CM with inorganic semiconductor constituents.

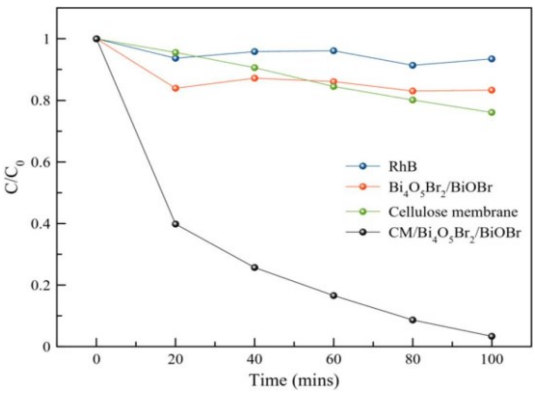

Figure 3.23 Photocatalytic degradation of RhB. Experiments were carried out under 405 nm illumination (20 W) with addition of hydrogen peroxide. Reproduced from paper *IV*[91] with permission.

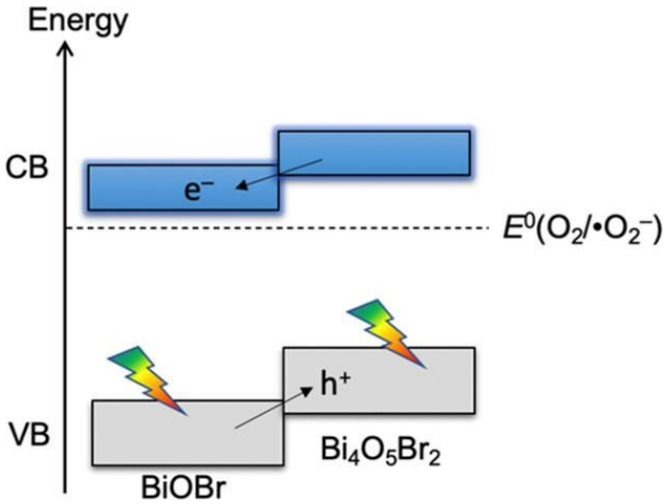

Figure 3.24 Mechanism of charge separation at $Bi_4O_5Br_2$/BiOBr heterojunction upon illumination. Reproduced from paper *IV*[91] with permission.

Figure 3.24 illustrates the band alignment of the $Bi_4O_5Br_2$/BiOBr heterojunction semiconductor and the suggested mechanism for photo RhB degradation. The augmented photocatalytic behaviour can be attributed to minimized agglomeration of the nanosheets, specifically, minimized loss of photochemically exposed surface area.

3.4.3 Adsorption of Co(II) and Ni(II) ions

The adsorption of Co(II) and Ni(II) was tested on CM and CM/$Bi_4O_5Br_2$/BiOBr composite with the help of our colleague. Specifically, the influence of phase contact time on the adsorption efficiency of membranes with and without catalyst targeting Co(II) and Ni(II) was characterized as shown in Figure 3.25. The metal ions solutions were prepared with 20 $mg \cdot L^{-1}$ and 50 $mg \cdot L^{-1}$ as the initial concentration. It was then adsorbed by modified CM and pure CM separately for 5 h, 24 h, 48 h, 72 h and 96 h in order to reach 100 % removal efficiency. The removal efficiency on Co(II) ions for both samples achieved over 70 % for the first 5 h with an initial concentration of both 20 $mg \cdot L^{-1}$ and 50 $mg \cdot L^{-1}$. As for the adsorption performance on Ni(II), the adsorption occurs slowly for both membranes; only 47.5 %–48 % can be removed in the first 5 h with an initial concentration of 20 $mg \cdot L^{-1}$. It should be noted that 94–100% of Both Co(II) and Ni(II) could be adsorbed during the 5–96 h. It could be concluded that the adsorption capacity toward Co(II) was 28.7 $mg \cdot g^{-1}$ for CM and 37.3 $mg \cdot g^{-1}$ for CM/$Bi_4O_5Br_2$/BiOBr; and 29.7

mg·g^{-1} for CM and 30.2 mg·g^{-1} for CM/$Bi_4O_5Br_2$/BiOBr toward Ni(II). As a result, CM/$Bi_4O_5Br_2$/BiOBr showed higher affinity to Co(II) than Ni(II). However, a direct comparison of the adsorption activity of the modified membrane with other adsorbents is difficult because the CM had a smaller surface area.

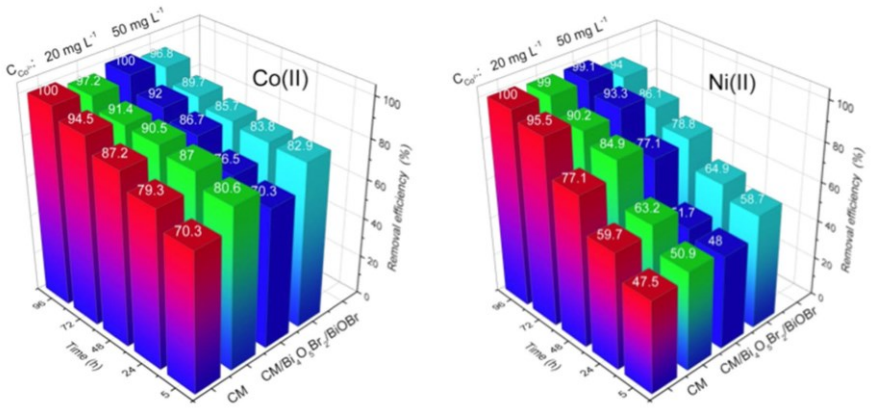

Figure 3.25 Influence of phase contact time on Co(II) and Ni(II) ions adsorption using CM and CM/$Bi_4O_5Br_2$/BiOBr composites. Adapted with permission from paper *IV*.[91]

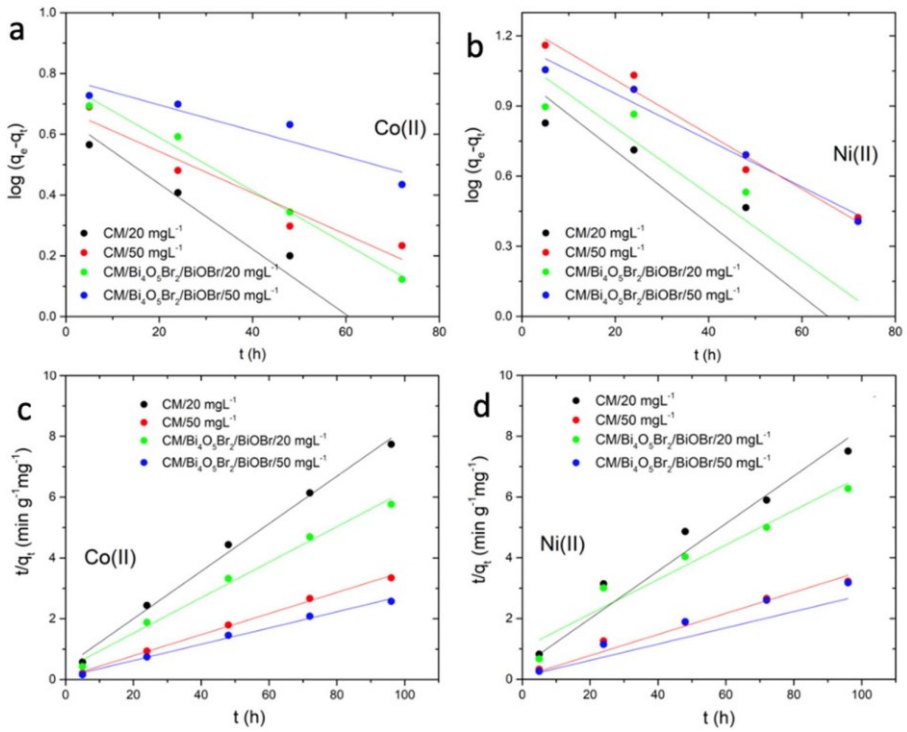

Figure 3.26 Influence of phase contact time on Co(II) and Ni(II) ions adsorption using CM and CM/$Bi_4O_5Br_2$/BiOBr composites. Adapted with permission from paper *IV*.[91]

The kinetic of Co(II) and Ni(II) adsorption with membranes was studied by pseudo-first and pseudo-second-order equations to understand the mechanisms and the rate-controlling step. The results indicate the adsorption capacity of the CM is independent of the modification of the photocatalyst but could be attributed to the carboxylic groups on the surface. The high correlation coefficients confirm pseudo-second-order equation model fits better with experimental results and could be applied to describe Co(II) and Ni(II) removal.

4. Summary and outlook

This research focused on water contaminants treatment by using sustainable materials-derived catalysts. Two different types of catalysts were proposed targeting nitrate, dye, and heavy metal ions decontaminated using either electric or optical energy.

In paper *I* and paper *II*, nitrate removal with the electrochemical method was achieved by using NDC materials as catalysts. Most importantly, the reaction mechanism and active sites were identified with different techniques.

- In paper *I*, NDC catalysts were prepared from silica gel and sucrose solution. Then the electrochemical NO_3RR was carried out after understanding the pyridinic and pyrrolic N species with spatial resolution. In combination with the ^{15}N solid-state NMR at atomic resolution, the electrochemical results proved that nitrate reduction was independent of the presence and structural positions of the nitrogen atoms in the carbon material. Moreover, nitrogen doping showed no effect on selectivity.
- In paper *II*, the synthesis was optimized by using cellulose as the starting material for NDC preparation with a simple stepwise carbonization procedure. The NDC-800 exhibited 73.1 % NH_4^+ selectivity toward ammonia and nearly 100 % nitrate removal efficiency with outstanding electrochemical stability. With the help of a complete computational description of NDC materials, the defective regions containing nitrogen atoms are fundamental to improving the material's response on NO_3RR toward NH_4^+.

In paper *III* and paper *IV*, photocatalytic dye degradation was carried out by using hybrid bio-inorganic materials. This research shows the possibility of converting cellulose-based materials to photocatalysts without sacrificing their abundant surface functional groups.

- In paper *III*, a combination of cellulose nanocrystals with TiO_2 nanorods was achieved with a low-temperature synthesis method to preserve the surface functional group. The decoration of Au nanocrystals promoted the light absorption performance of the catalyst in the visible light region. The hybrid catalyst shows an excellent performance with RhB degradation under solar light simulator illumination.

- In paper *IV*, cellulose-supported $Bi_4O_5Br_2$/BiOBr membrane was fabricated at a relatively low temperature. The hybrid material showed an outstanding RhB degradation performance under blue light illumination. Additionally, the hybrid catalyst simultaneously removes heavy metal ions due to the surface functional group of cellulose. A comprehensive effect between cellulose substrate and inorganic catalysts supports each other and promotes every part's performance. These results show an inspiring and promising potential for hybrid catalysts application.

Notably, ^{15}N solid-state NMR spectroscopy was proven to be an excellent tool for characterizing the type of N species on the surface of mesoporous carbon material. Furthermore, theoretical calculation showed the detailed location of the N atoms in the carbon structure. The combination of ^{15}N solid-state NMR spectroscopy with theoretical analysis showed the potential for catalyst characterization on an atomic level.

In conclusion, this thesis proves that cellulose as a biomass material can be used as raw materials for metal-free catalysts synthesising and the substrate of bio-inorganic hybrid photocatalysts. The performance of both electro/photo catalysts is comparable and/or even better compared with pure inorganic catalysts. The application of cellulose or other biomass materials in environmental applications can make tremendous contributions to environmental governance, which is a severe problem for humans. However, it should be clarified that applying biomass materials for hybrid catalysts is still challenging. The maintenance of surface functional groups is one of the most critical factors for synthesising bio-inorganic hybrid catalysts. The surface functional groups from biomass materials play crucial roles in the adsorption of contaminants. This thesis preserved the surface functional groups by a low-temperature synthesis method, and this could be a promising strategy for future work. Additionally, how to scale up the synthesising of biomass material-derived catalysts without destroying biomass substrates is another problem. This work only shows the possibility of using cellulose for preparing catalysts on a laboratory scale.

Acknowledgements

First of all, I would like to thank the "Excellence Centre of Tribology" AC^{2}T research GmbH (COMET InTribology Project, FFG No. 872176, project coordinator: AC2T research GmbH). I want to express gratitude to my esteemed supervisor Prof. Adam Slabon for giving me this chance to study as a Ph.D. student in this wonderful group, and thank you for your kind guidance and all the inspiring discussions on projects. I am very grateful for your trust and the freedom you provided in my research, which developed great independence in my career. Also, I want to thank my co-supervisor, Dr. Thomas Thersleff, thanks for all your help and guidance on my research projects. I really enjoyed our discussions. You are an outstanding researcher, and I am sure you will find a good position in which you will be able to pursue your career goals! Lots of thanks to Dr. Serhiy Budnyk from AC^{2}T research GmbH, Austria; and Prof. Piotr Kuśtrowski from Jagiellonian University, Poland. Thanks for your help and fruitful discussions.

Working with so many intelligent and amazing people from MMK has been a great pleasure. I really appreciate your support during the past three and a half years. Thanks to Xiaodong, Gunnar, and Niklas for guiding the direction of the MMK and have provided such a fantastic working environment. Thanks to Tom, Ken, Ulrich, Lennart, Mats, Kjell, Mirva, Hongyi, and Tamara for sharing your knowledge, and I really enjoyed a lot from the lectures. Thanks to Aji and Mika for the very nice collaborations. I admire your professional attitude and patience. Also, I would like to thank Cheuk-wai and Anumol, thank you so so much for the training and your patience in picking up my endless call on reporting issues about the instruments. To all the administration staff, especially Helmi, Zesi and Tatiana, thank you for your support and assistance.

I would consider myself being very lucky to meet all my team members. I had a wonderful three and half years with you guys, and I really enjoyed the atmosphere in the group and office. Thank you Jedrzej. It is my great pleasure to meet you and start my Ph.D. on the same day as you. Also, as the backbone of the Three Js, I want to thank you, Joy, for making our life and work colourful. Big thanks to all the present and former group members: Robin, Bruno, Gaby, Charlie, Bernadette, Maria, Casper, Kerem, Istven, Sina and

Tetyana. Words can not express how much I cherish this experience, and I do wish you all the best for your future.

I appreciate the awesome colleagues and friends in MMK: Andrea, Alek, Aji, Andi, Atefeh, Carina, Dimi, Elnaz, Ehsan, Erik, Fengyang, Houssine, Ievgen, Jiayin, Jingjing, Jinrong, Jungyoun, Jian, Kanglei, Kosta, Maja, Martin, Mika, Miao, Mohammad, Natalia, Naeem, Paolo, Pierre, Sadaf, Shiqi, Shihui, Taimin, Varvra, Vahid, Wenming, Xia, Ximena, Zhehao and many others. Please forgive me if I forget any names. Thank you all for sharing lunch, conversation, and your knowledge!

I would give my parents the noblest thanks for supporting me and encouraging me all the time. I could only meet my parents and my family once during the past three years because of the pandemic. We could only talk on video calls, and I know they missed me so much, but they decided to keep this in their deep mind not to stress me. There is a special family member, the willful princess–Oudi. Thank you for spending your entire life with us, and thank you for being my growth partner. I am delighted that I could see you again before you passed away; I will always miss you.

To Wensi, my dear love, thank you so much for everything. You are the reason that I decided to be here, and you are the mainstay that I could finish my Ph.D. Thank you for your comfort when I am sad, for sharing my happiness, and for being your companion.

References

(1) Shannon, M. A.; Bohn, P. W.; Elimelech, M.; Georgiadis, J. G.; Marĩas, B. J.; Mayes, A. M. Science and Technology for Water Purification in the Coming Decades. *Nature*. Nature Publishing Group March 20, 2008, pp 301–310. https://doi.org/10.1038/nature06599.

(2) Archna; Sharma, S. K.; Sobti, R. C. Nitrate Removal from Ground Water: A Review. *E-Journal of Chemistry*. 2012. https://doi.org/10.1155/2012/154616.

(3) Kapoor, A.; Viraraghavan, T. Nitrate Removal From Drinking Water—Review. *Journal of Environmental Engineering* **1997**, *123* (4). https://doi.org/10.1061/(asce)0733-9372(1997)123:4(371).

(4) Anastas, P. T.; Williamson, T. C. Green Chemistry: Designing Chemistry for the Environment. *Choice Reviews Online* **1996**, *34* (03). https://doi.org/10.5860/choice.34-1555.

(5) Anastas, P.; Eghbali, N. Green Chemistry: Principles and Practice. *Chem Soc Rev* **2010**, *39* (1), 301–312. https://doi.org/10.1039/b918763b.

(6) Anastas, P. T.; Warner, J. C. Green Chemistry: Theory and Practice. *Green Chemistry: Theory and Practice, Oxford University Press, New York* **1998**.

(7) Prado, A. G. S. Green Chemistry, the Chemical Challenges of the New Millenium. *Quim Nova* **2003**, *26* (5). https://doi.org/10.1590/s0100-40422003000500018.

(8) Bolisetty, S.; Peydayesh, M.; Mezzenga, R. Sustainable Technologies for Water Purification from Heavy Metals: Review and Analysis. *Chemical Society Reviews*. Royal Society of Chemistry January 21, 2019, pp 463–487. https://doi.org/10.1039/c8cs00493e.

(9) Montgomery, M. A.; Elimelech, M. Water And Sanitation in Developing Countries: Including Health in the Equation. *Environ Sci Technol* **2007**, *41* (1). https://doi.org/10.1021/es072435t.

(10) Singh, P.; Bengtsson, L. Impact of Warmer Climate on Melt and Evaporation for the Rainfed, Snowfed and Glacierfed Basins in the Himalayan Region. *J Hydrol (Amst)* **2005**, *300* (1–4). https://doi.org/10.1016/j.jhydrol.2004.06.005.

(11) Liu, S.; Sun, W.; Shen, Y.; Li, G. Glacier Changes since the Little Ice Age Maximum in the Western Qilian Shan, Northwest China, and Consequences of Glacier Runoff for Water Supply. *Journal of Glaciology* **2003**, *49* (164). https://doi.org/10.3189/172756503781830926.

(12) Barnett, T. P.; Adam, J. C.; Lettenmaier, D. P. Potential Impacts of a Warming Climate on Water Availability in Snow-Dominated Regions. *Nature*. 2005. https://doi.org/10.1038/nature04141.

(13) Bradley, R. S.; Vuille, M.; Diaz, H. F.; Vergara, W. Threats to Water Supplies in the Tropical Andes. *Science*. 2006. https://doi.org/10.1126/science.1128087.

(14) Garcia-Segura, S.; Lanzarini-Lopes, M.; Hristovski, K.; Westerhoff, P. Electrocatalytic Reduction of Nitrate: Fundamentals to Full-Scale Water Treatment Applications. *Applied Catalysis B: Environmental*. Elsevier B.V. November 15, 2018, pp 546–568. https://doi.org/10.1016/j.apcatb.2018.05.041.

(15) Varjani, S.; Rakholiya, P.; Ng, H. Y.; You, S.; Teixeira, J. A. Microbial Degradation of Dyes: An Overview. *Bioresource Technology*. Elsevier Ltd October 1, 2020. https://doi.org/10.1016/j.biortech.2020.123728.

(16) Ajaz, M.; Shakeel, S.; Rehman, A. Microbial Use for Azo Dye Degradation—a Strategy for Dye Bioremediation. *International Microbiology*. 2020. https://doi.org/10.1007/s10123-019-00103-2.

(17) Sillanpää, M.; Shestakova, M. *Electrochemical Water Treatment Methods: Fundamentals, Methods and Full Scale Applications*; 2017.

(18) Peng, H.; Guo, J. Removal of Chromium from Wastewater by Membrane Filtration, Chemical Precipitation, Ion Exchange, Adsorption Electrocoagulation, Electrochemical Reduction, Electrodialysis, Electrodeionization, Photocatalysis and Nanotechnology: A Review. *Environmental Chemistry Letters*. Springer Science and Business Media Deutschland GmbH November 1, 2020, pp 2055–2068. https://doi.org/10.1007/s10311-020-01058-x.

(19) Yang, Q.; Yao, F.; Zhong, Y.; Wang, D.; Chen, F.; Sun, J.; Hua, S.; Li, S.; Li, X.; Zeng, G. Catalytic and Electrocatalytic Reduction of Perchlorate in Water – A Review. *Chemical Engineering Journal*. 2016. https://doi.org/10.1016/j.cej.2016.08.041.

(20) Mousset, E.; Doudrick, K. A Review of Electrochemical Reduction Processes to Treat Oxidized Contaminants in Water. *Current Opinion in Electrochemistry*. Elsevier B.V. August 1, 2020, pp 221–227. https://doi.org/10.1016/j.coelec.2020.07.008.

(21) Comninellis, C.; Chen, G. *Electrochemistry for the Environment*; 2010. https://doi.org/10.1007/978-0-387-68318-8.

(22) Alkhadra, M. A.; Su, X.; Suss, M. E.; Tian, H.; Guyes, E. N.; Shocron, A. N.; Conforti, K. M.; de Souza, J. P.; Kim, N.; Tedesco, M.; Khoiruddin, K.; Wenten, I. G.; Santiago, J. G.; Hatton, T. A.; Bazant,

M. Z. Electrochemical Methods for Water Purification, Ion Separations, and Energy Conversion. *Chemical Reviews*. American Chemical Society August 24, 2022, pp 13547–13635. https://doi.org/10.1021/acs.chemrev.1c00396.

(23) Sun, C.; Baig, S. A.; Lou, Z.; Zhu, J.; Wang, Z.; Li, X.; Wu, J.; Zhang, Y.; Xu, X. Electrocatalytic Dechlorination of 2,4-Dichlorophenoxyacetic Acid Using Nanosized Titanium Nitride Doped Palladium/Nickel Foam Electrodes in Aqueous Solutions. *Appl Catal B* **2014**, *158–159*, 38–47. https://doi.org/10.1016/j.apcatb.2014.04.004.

(24) Wang, Y.; Wang, C.; Li, M.; Yu, Y.; Zhang, B. Nitrate Electroreduction: Mechanism Insight,: In Situ Characterization, Performance Evaluation, and Challenges. *Chemical Society Reviews*. Royal Society of Chemistry June 21, 2021, pp 6720–6733. https://doi.org/10.1039/d1cs00116g.

(25) Křišťál, J.; Kodým, R.; Bouzek, K.; Jiřičný, V. Electrochemical Microreactor and Gas-Evolving Reactions. *Electrochem commun* **2008**, *10* (2). https://doi.org/10.1016/j.elecom.2007.11.029.

(26) Mousset, E.; Puce, M.; Pons, M. N. Advanced Electro-Oxidation with Boron-Doped Diamond for Acetaminophen Removal from Real Wastewater in a Microfluidic Reactor: Kinetics and Mass-Transfer Studies. *ChemElectroChem* **2019**, *6* (11). https://doi.org/10.1002/celc.201900182.

(27) Mao, R.; Zhao, X.; Lan, H.; Liu, H.; Qu, J. Efficient Electrochemical Reduction of Bromate by a Pd/RGO/CFP Electrode with Low Applied Potentials. *Appl Catal B* **2014**, *160–161* (1). https://doi.org/10.1016/j.apcatb.2014.04.040.

(28) Martínez, J.; Ortiz, A.; Ortiz, I. State-of-the-Art and Perspectives of the Catalytic and Electrocatalytic Reduction of Aqueous Nitrates. *Applied Catalysis B: Environmental*. Elsevier B.V. 2017, pp 42–59. https://doi.org/10.1016/j.apcatb.2017.02.016.

(29) Ding, J.; Li, W.; Zhao, Q. L.; Wang, K.; Zheng, Z.; Gao, Y. Z. Electroreduction of Nitrate in Water: Role of Cathode and Cell Configuration. *Chemical Engineering Journal* **2015**, *271*. https://doi.org/10.1016/j.cej.2015.03.001.

(30) Dash, B. P.; Chaudhari, S. Electrochemical Denitrificaton of Simulated Ground Water. *Water Res* **2005**, *39* (17). https://doi.org/10.1016/j.watres.2005.07.032.

(31) Lacasa, E.; Cañizares, P.; Llanos, J.; Rodrigo, M. A. Effect of the Cathode Material on the Removal of Nitrates by Electrolysis in Non-Chloride Media. *J Hazard Mater* **2012**, *213–214*. https://doi.org/10.1016/j.jhazmat.2012.02.034.

(32) Bouzek, K.; Paidar, M.; Sadílková, A.; Bergmann, H. Electrochemical Reduction of Nitrate in Weakly Alkaline Solutions. *J Appl Electrochem* **2001**, *31* (11). https://doi.org/10.1023/A:1012755222981.
(33) Katsounaros, I.; Ipsakis, D.; Polatides, C.; Kyriacou, G. Efficient Electrochemical Reduction of Nitrate to Nitrogen on Tin Cathode at Very High Cathodic Potentials. *Electrochim Acta* **2006**, *52* (3). https://doi.org/10.1016/j.electacta.2006.07.034.
(34) Mattarozzi, L.; Cattarin, S.; Comisso, N.; Guerriero, P.; Musiani, M.; Vázquez-Gómez, L.; Verlato, E. Electrochemical Reduction of Nitrate and Nitrite in Alkaline Media at CuNi Alloy Electrodes. *Electrochim Acta* **2013**, *89*. https://doi.org/10.1016/j.electacta.2012.11.074.
(35) Reyter, D.; Bélanger, D.; Roué, L. Optimization of the Cathode Material for Nitrate Removal by a Paired Electrolysis Process. *J Hazard Mater* **2011**, *192* (2). https://doi.org/10.1016/j.jhazmat.2011.05.054.
(36) Comisso, N.; Cattarin, S.; Guerriero, P.; Mattarozzi, L.; Musiani, M.; Vázquez-Gómez, L.; Verlato, E. Study of Cu, Cu-Ni and Rh-Modified Cu Porous Layers as Electrode Materials for the Electroanalysis of Nitrate and Nitrite Ions. *Journal of Solid State Electrochemistry* **2016**, *20* (4). https://doi.org/10.1007/s10008-015-2915-7.
(37) Mattarozzi, L.; Cattarin, S.; Comisso, N.; Gerbasi, R.; Guerriero, P.; Musiani, M.; Vázquez-Gómez, L.; Verlato, E. Electrodeposition of Cu-Ni Alloy Electrodes with Bimodal Porosity and Their Use for Nitrate Reduction. *ECS Electrochemistry Letters* **2013**, *2* (11). https://doi.org/10.1149/2.004311eel.
(38) MácOvá, Z.; Bouzek, K.; Šerák, J. Electrocatalytic Activity of Copper Alloys for NO3- Reduction in a Weakly Alkaline Solution : PPPart 2: Copper-Tin. *J Appl Electrochem* **2007**, *37* (5). https://doi.org/10.1007/s10800-006-9287-8.
(39) Mácová, Z.; Bouzek, K. Electrocatalytic Activity of Copper Alloys for NO3- Reduction in a Weakly Alkaline Solution Part 1: Copper-Zinc. *J Appl Electrochem* **2005**, *35* (12). https://doi.org/10.1007/s10800-005-9028-4.
(40) Li, M.; Feng, C.; Zhang, Z.; Lei, X.; Chen, R.; Yang, Y.; Sugiura, N. Simultaneous Reduction of Nitrate and Oxidation of By-Products Using Electrochemical Method. *J Hazard Mater* **2009**, *171* (1–3). https://doi.org/10.1016/j.jhazmat.2009.06.066.
(41) Mattarozzi, L.; Cattarin, S.; Comisso, N.; Gerbasi, R.; Guerriero, P.; Musiani, M.; Vázquez-Gómez, L.; Verlato, E. Electrodeposition of Compact and Porous Cu-Zn Alloy Electrodes and Their Use in the Cathodic Reduction of Nitrate. *J Electrochem Soc* **2015**, *162* (6). https://doi.org/10.1149/2.1041506jes.
(42) Su, J. F.; Ruzybayev, I.; Shah, I.; Huang, C. P. The Electrochemical Reduction of Nitrate over Micro-Architectured Metal Electrodes with

Stainless Steel Scaffold. *Appl Catal B* **2016**, *180*. https://doi.org/10.1016/j.apcatb.2015.06.028.

(43) Anastasopoulos, A.; Hannah, L.; Hayden, B. E. High Throughput Optimisation of PdCu Alloy Electrocatalysts for the Reduction of Nitrate Ions. *J Catal* **2013**, *305*. https://doi.org/10.1016/j.jcat.2013.04.010.

(44) Ghodbane, O.; Sarrazin, M.; Roué, L.; Bélanger, D. Electrochemical Reduction of Nitrate on Pyrolytic Graphite-Supported Cu and Pd–Cu Electrocatalysts. *J Electrochem Soc* **2008**, *155* (6). https://doi.org/10.1149/1.2900094.

(45) Reyter, D.; Bélanger, D.; Roué, L. Elaboration of Cu-Pd Films by Coelectrodeposition: Application to Nitrate Electroreduction. *Journal of Physical Chemistry C* **2009**, *113* (1). https://doi.org/10.1021/jp805484t.

(46) Birdja, Y. Y.; Yang, J.; Koper, M. T. M. Electrocatalytic Reduction of Nitrate on Tin-Modified Palladium Electrodes. *Electrochim Acta* **2014**, *140*. https://doi.org/10.1016/j.electacta.2014.06.011.

(47) Tada, K.; Kawaguchi, T.; Shimazu, K. High Electrocatalytic Performance of Pd/Sn/Au Electrodes for Nitrate Reduction. *Journal of Electroanalytical Chemistry* **2004**, *572* (1). https://doi.org/10.1016/j.jelechem.2004.06.004.

(48) Motahar Hossain, M.; Nakata, K.; Kawaguchi, T.; Shimazu, K. Reduction of Nitrate on Electrochemically Pre-Reduced Tin-Modified Palladium Electrodes. *Journal of Electroanalytical Chemistry* **2013**, *707*. https://doi.org/10.1016/j.jelechem.2013.08.015.

(49) Shimazu, K.; Goto, R.; Piao, S.; Kayama, R.; Nakata, K.; Yoshinaga, Y. Reduction of Nitrate Ions on Tin-Modified Palladium Thin Film Electrodes. *Journal of Electroanalytical Chemistry* **2007**, *601* (1–2). https://doi.org/10.1016/j.jelechem.2006.11.005.

(50) Ma, X.; Li, M.; Feng, C.; Hu, W.; Wang, L.; Liu, X. Development and Reaction Mechanism of Efficient Nano Titanium Electrode: Reconstructed Nanostructure and Enhanced Nitrate Removal Efficiency. *Journal of Electroanalytical Chemistry* **2016**, *782*. https://doi.org/10.1016/j.jelechem.2016.10.047.

(51) Su, L.; Li, K.; Zhang, H.; Fan, M.; Ying, D.; Sun, T.; Wang, Y.; Jia, J. Electrochemical Nitrate Reduction by Using a Novel Co3O4/Ti Cathode. *Water Res* **2017**, *120*. https://doi.org/10.1016/j.watres.2017.04.069.

(52) Wang, L.; Yang, Z.; Xu, L.; Yang, Y. NCVCS: Network-Coding-Based Video Conference System for Mobile Devices in Multicast Networks. *Ad Hoc Networks* **2016**, *45*. https://doi.org/10.1016/j.adhoc.2016.03.002.

(53) Wang, L.; Li, M.; Liu, X.; Feng, C.; Chen, N.; Ma, X.; Ding, G. Electrochemical Behavior of Ti-Based Nano-Electrode for Highly

Efficient Denitrification in Synthetic Groundwater. *J Electrochem Soc* **2017**, *164* (12). https://doi.org/10.1149/2.0821712jes.

(54) Kim, D. E.; Pak, D. Ti Plate with TiO2 Nanotube Arrays as a Novel Cathode for Nitrate Reduction. *Chemosphere* **2019**, *228*. https://doi.org/10.1016/j.chemosphere.2019.04.071.

(55) Jia, R.; Wang, Y.; Wang, C.; Ling, Y.; Yu, Y.; Zhang, B. Boosting Selective Nitrate Electroreduction to Ammonium by Constructing Oxygen Vacancies in TiO2. *ACS Catal* **2020**, *10* (6). https://doi.org/10.1021/acscatal.9b05260.

(56) Ma, X.; Li, M.; Meng, F.; Wang, L.; Feng, C.; Chen, N.; Liu, X. Efficient Nano Titanium Electrode via a Two-Step Electrochemical Anodization with Reconstructed Nanotubes: Electrochemical Activity and Stability. *Chemosphere* **2018**, *202*. https://doi.org/10.1016/j.chemosphere.2018.03.063.

(57) Li, C.; Li, K.; Chen, C.; Tang, Q.; Sun, T.; Jia, J. Electrochemical Removal of Nitrate Using a Nanosheet Structured Co3O4/Ti Cathode: Effects of Temperature, Current and PH Adjusting. *Sep Purif Technol* **2020**, *237*. https://doi.org/10.1016/j.seppur.2019.116485.

(58) Rao, X.; Shao, X.; Xu, J.; Yi, J.; Qiao, J.; Li, Q.; Wang, H.; Chien, M.; Inoue, C.; Liu, Y.; Zhang, J. Efficient Nitrate Removal from Water Using Selected Cathodes and Ti/PbO2 Anode: Experimental Study and Mechanism Verification. *Sep Purif Technol* **2019**, *216*. https://doi.org/10.1016/j.seppur.2019.02.009.

(59) Ghazouani, M.; Akrout, H.; Bousselmi, L. Efficiency of Electrochemical Denitrification Using Electrolysis Cell Containing BDD Electrode. *Desalination Water Treat* **2015**, *53* (4). https://doi.org/10.1080/19443994.2014.884473.

(60) Ghazouani, M.; Akrout, H.; Jomaa, S.; Jellali, S.; Bousselmi, L. Enhancing Removal of Nitrates from Highly Concentrated Synthetic Wastewaters Using Bipolar Si/BDD Cell: Optimization and Mechanism Study. *Journal of Electroanalytical Chemistry* **2016**, *783*. https://doi.org/10.1016/j.jelechem.2016.10.048.

(61) Kuang, P.; Natsui, K.; Einaga, Y. Comparison of Performance between Boron-Doped Diamond and Copper Electrodes for Selective Nitrogen Gas Formation by the Electrochemical Reduction of Nitrate. *Chemosphere* **2018**, *210*. https://doi.org/10.1016/j.chemosphere.2018.07.039.

(62) Kamiya, K.; Hashimoto, K.; Nakanishi, S. Graphene Defects as Active Catalytic Sites That Are Superior to Platinum Catalysts in Electrochemical Nitrate Reduction. *ChemElectroChem* **2014**, *1* (5). https://doi.org/10.1002/celc.201300237.

(63) Weinberg, N. L.; Weinberg, H. R. Electrochemical Oxidation of Organic Compounds. *Chem Rev* **1968**, *68* (4). https://doi.org/10.1021/cr60254a003.

(64) Ajmal, A.; Majeed, I.; Malik, R. N.; Idriss, H.; Nadeem, M. A. Principles and Mechanisms of Photocatalytic Dye Degradation on TiO 2 Based Photocatalysts: A Comparative Overview. *RSC Advances*. 2014. https://doi.org/10.1039/c4ra06658h.

(65) Wang, H.; Zhang, L.; Chen, Z.; Hu, J.; Li, S.; Wang, Z.; Liu, J.; Wang, X. Semiconductor Heterojunction Photocatalysts: Design, Construction, and Photocatalytic Performances. *Chemical Society Reviews*. 2014. https://doi.org/10.1039/c4cs00126e.

(66) Etacheri, V.; Michlits, G.; Seery, M. K.; Hinder, S. J.; Pillai, S. C. A Highly Efficient TiO2-XCx Nano-Heterojunction Photocatalyst for Visible Light Induced Antibacterial Applications. *ACS Appl Mater Interfaces* **2013**, *5* (5). https://doi.org/10.1021/am302676a.

(67) Tang, J. X.; Lee, C. S.; Lee, S. T. Electronic Structures of Organic/Organic Heterojunctions: From Vacuum Level Alignment to Fermi Level Pinning. *J Appl Phys* **2007**, *101* (6). https://doi.org/10.1063/1.2710297.

(68) Anwer, H.; Mahmood, A.; Lee, J.; Kim, K. H.; Park, J. W.; Yip, A. C. K. Photocatalysts for Degradation of Dyes in Industrial Effluents: Opportunities and Challenges. *Nano Research*. Tsinghua University Press May 1, 2019, pp 955–972. https://doi.org/10.1007/s12274-019-2287-0.

(69) Zhang, W.; Hu, C.; Zhai, W.; Wang, Z.; Sun, Y.; Chi, F.; Ran, S.; Liu, X.; Lv, Y. Novel Ag3PO4/CeO2 p-n Hierarchical Heterojunction with Enhanced Photocatalytic Performance. *Materials Research* **2016**, *19* (3). https://doi.org/10.1590/1980-5373-MR-2016-0009.

(70) Tran, H. N.; You, S. J.; Hosseini-Bandegharaei, A.; Chao, H. P. Mistakes and Inconsistencies Regarding Adsorption of Contaminants from Aqueous Solutions: A Critical Review. *Water Research*. 2017. https://doi.org/10.1016/j.watres.2017.04.014.

(71) Singh, N. B.; Nagpal, G.; Agrawal, S.; Rachna. Water Purification by Using Adsorbents: A Review. *Environmental Technology and Innovation*. Elsevier B.V. August 1, 2018, pp 187–240. https://doi.org/10.1016/j.eti.2018.05.006.

(72) Wang, L.; Shi, C.; Pan, L.; Zhang, X.; Zou, J. J. Rational Design, Synthesis, Adsorption Principles and Applications of Metal Oxide Adsorbents: A Review. *Nanoscale*. Royal Society of Chemistry February 28, 2020, pp 4790–4815. https://doi.org/10.1039/c9nr09274a.

(73) Theiss, F. L.; Couperthwaite, S. J.; Ayoko, G. A.; Frost, R. L. A Review of the Removal of Anions and Oxyanions of the Halogen Elements from Aqueous Solution by Layered Double Hydroxides. *J Colloid Interface Sci* **2014**, *417*. https://doi.org/10.1016/j.jcis.2013.11.040.

(74) Tang, D.; Zhang, G. Efficient Removal of Fluoride by Hierarchical Ce-Fe Bimetal Oxides Adsorbent: Thermodynamics, Kinetics and

Mechanism. *Chemical Engineering Journal* **2016**, *283*. https://doi.org/10.1016/j.cej.2015.08.019.

(75) Qasem, N. A. A.; Mohammed, R. H.; Lawal, D. U. Removal of Heavy Metal Ions from Wastewater: A Comprehensive and Critical Review. *npj Clean Water*. Nature Research December 1, 2021. https://doi.org/10.1038/s41545-021-00127-0.

(76) Anastopoulos, I.; Kyzas, G. Z. Agricultural Peels for Dye Adsorption: A Review of Recent Literature. *Journal of Molecular Liquids*. 2014. https://doi.org/10.1016/j.molliq.2014.11.006.

(77) Bethke, K.; Palantöken, S.; Andrei, V.; Roß, M.; Raghuwanshi, V. S.; Kettemann, F.; Greis, K.; Ingber, T. T. K.; Stückrath, J. B.; Valiyaveettil, S.; Rademann, K. Functionalized Cellulose for Water Purification, Antimicrobial Applications, and Sensors. *Adv Funct Mater* **2018**, *28* (23). https://doi.org/10.1002/adfm.201800409.

(78) Bhatnagar, A.; Sillanpää, M.; Witek-Krowiak, A. Agricultural Waste Peels as Versatile Biomass for Water Purification - A Review. *Chemical Engineering Journal*. 2015. https://doi.org/10.1016/j.cej.2015.01.135.

(79) Karim, Z.; Georgouvelas, D.; Svedberg, A.; Monti, S.; Mathew, A. P. Upscaled Engineered Functional Microfibrillated Cellulose Flat Sheet Membranes for Removing Charged Water Pollutants. *Sep Purif Technol* **2022**, *289*. https://doi.org/10.1016/j.seppur.2022.120745.

(80) Karim, Z.; Svedberg, A.; Lee, K. Y.; Khan, M. J. Processing-Structure-Property Correlation Understanding of Microfibrillated Cellulose Based Dimensional Structures for Ferric Ions Removal. *Sci Rep* **2019**, *9* (1). https://doi.org/10.1038/s41598-019-46812-6.

(81) Liu, P.; Sehaqui, H.; Tingaut, P.; Wichser, A.; Oksman, K.; Mathew, A. P. Cellulose and Chitin Nanomaterials for Capturing Silver Ions (Ag+) from Water via Surface Adsorption. *Cellulose* **2014**, *21* (1). https://doi.org/10.1007/s10570-013-0139-5.

(82) Li, X.; Zhang, J.; Xie, H.; Pan, Y.; Liu, J.; Huang, Z.; Long, X.; Xiao, H. Cellulose-Based Adsorbents Loaded with Zero-Valent Iron for Removal of Metal Ions from Contaminated Water. *Environmental Science and Pollution Research* **2020**, *27* (26). https://doi.org/10.1007/s11356-020-09390-z.

(83) Ma, Z.; Thersleff, T.; Görne, A. L.; Cordes, N.; Liu, Y.; Jakobi, S.; Rokicinska, A.; Schichtl, Z. G.; Coridan, R. H.; Kustrowski, P.; Schnick, W.; Dronskowski, R.; Slabon, A. Quaternary Core-Shell Oxynitride Nanowire Photoanode Containing a Hole-Extraction Gradient for Photoelectrochemical Water Oxidation. *ACS Appl Mater Interfaces* **2019**, *11* (21). https://doi.org/10.1021/acsami.9b02483.

(84) Ma, Z.; Jaworski, A.; George, J.; Rokicinska, A.; Thersleff, T.; Budnyak, T. M.; Hautier, G.; Pell, A. J.; Dronskowski, R.; Kuśtrowski, P.; Slabon, A. Exploring the Origins of Improved Photocurrent by

Acidic Treatment for Quaternary Tantalum-Based Oxynitride Photoanodes on the Example of CaTaO2N. *Journal of Physical Chemistry C* **2020**, *124* (1). https://doi.org/10.1021/acs.jpcc.9b09838.

(85) Bondeson, D.; Mathew, A.; Oksman, K. Optimization of the Isolation of Nanocrystals from Microcrystalline Cellulose by Acid Hydrolysis. *Cellulose* **2006**, *13* (2). https://doi.org/10.1007/s10570-006-9061-4.

(86) Camarero Espinosa, S.; Kuhnt, T.; Foster, E. J.; Weder, C. Isolation of Thermally Stable Cellulose Nanocrystals by Phosphoric Acid Hydrolysis. *Biomacromolecules* **2013**, *14* (4). https://doi.org/10.1021/bm400219u.

(87) Mathew, A. P.; Oksman, K.; Karim, Z.; Liu, P.; Khan, S. A.; Naseri, N. Process Scale up and Characterization of Wood Cellulose Nanocrystals Hydrolysed Using Bioethanol Pilot Plant. *Ind Crops Prod* **2014**, *58*. https://doi.org/10.1016/j.indcrop.2014.04.035.

(88) Davi, M.; Schultze, T.; Kleinschmidt, D.; Schiefer, F.; Hahn, B.; Slabon, A. Gold Nanocrystal Arrays as Electrocatalysts for the Oxidation of Methanol and Ethanol. *Zeitschrift fur Naturforschung - Section B Journal of Chemical Sciences* **2016**, *71* (7). https://doi.org/10.1515/znb-2016-0032.

(89) Robarge, W. P.; Edwards, A.; Johnson, B. Water and Waste Water Analysis for Nitrate via Nitration of Salicylic Acid. *Commun Soil Sci Plant Anal* **1983**, *14* (12). https://doi.org/10.1080/00103628309367444.

(90) Zhao, Y.; Shi, R.; Bian, X.; Zhou, C.; Zhao, Y.; Zhang, S.; Wu, F.; Waterhouse, G. I. N.; Wu, L. Z.; Tung, C. H.; Zhang, T. Ammonia Detection Methods in Photocatalytic and Electrocatalytic Experiments: How to Improve the Reliability of NH 3 Production Rates? *Advanced Science* **2019**, *6* (8). https://doi.org/10.1002/advs.201802109.

(91) Onwumere, J.; Piątek, J.; Budnyak, T.; Chen, J.; Budnyk, S.; Karim, Z.; Thersleff, T.; Kuśtrowski, P.; Mathew, A. P.; Slabon, A. CelluPhot: Hybrid Cellulose-Bismuth Oxybromide Membrane for Pollutant Removal. *ACS Appl Mater Interfaces* **2020**, *12* (38), 42891–42901. https://doi.org/10.1021/acsami.0c12739.

(92) Hwang, T. L.; van Zijl, P. C. M.; Garwood, M. Fast Broadband Inversion by Adiabatic Pulses. *Journal of Magnetic Resonance*. 1998. https://doi.org/10.1006/jmre.1998.1441.

(93) Kervern, G.; Pintacuda, G.; Emsley, L. Fast Adiabatic Pulses for Solid-State NMR of Paramagnetic Systems. *Chem Phys Lett* **2007**, *435* (1–3). https://doi.org/10.1016/j.cplett.2006.12.056.

(94) Handy, N. C.; Cohen, A. J. Left-Right Correlation Energy. *Mol Phys* **2001**, *99* (5). https://doi.org/10.1080/00268970010018431.

(95) Lee Chengteh; Weitao, Y.; Robert, P. G. Development of the Colle-Salvetti Correlation-Energy Formula into a Functional of the Electron Density. *Phys Rev B* **1988**, *37*.

(96) Grimme, S.; Antony, J.; Ehrlich, S.; Krieg, H. A Consistent and Accurate Ab Initio Parametrization of Density Functional Dispersion Correction (DFT-D) for the 94 Elements H-Pu. *Journal of Chemical Physics* **2010**, *132* (15). https://doi.org/10.1063/1.3382344.

(97) Grimme, S.; Ehrlich, S.; Goerigk, L. Effect of the Damping Function in Dispersion Corrected Density Functional Theory. *J Comput Chem* **2011**, *32* (7). https://doi.org/10.1002/jcc.21759.

(98) Kozuch, S.; Martin, J. M. L. DSD-PBEP86: In Search of the Best Double-Hybrid DFT with Spin-Component Scaled MP2 and Dispersion Corrections. *Physical Chemistry Chemical Physics* **2011**, *13* (45). https://doi.org/10.1039/c1cp22592h.

(99) Rzepka, P.; Bacsik, Z.; Pell, A. J.; Hedin, N.; Jaworski, A. Nature of Chemisorbed CO2 in Zeolite A. *Journal of Physical Chemistry C* **2019**, *123* (35). https://doi.org/10.1021/acs.jpcc.9b04142.

(100) Szewczyk, I.; Rokicińska, A.; Michalik, M.; Chen, J.; Jaworski, A.; Aleksis, R.; Pell, A. J.; Hedin, N.; Slabon, A.; Kuśtrowski, P. Electrochemical Denitrification and Oxidative Dehydrogenation of Ethylbenzene over N-Doped Mesoporous Carbon: Atomic Level Understanding of Catalytic Activity by 15N NMR Spectroscopy. *Chemistry of Materials* **2020**, *32* (17), 7263–7273. https://doi.org/10.1021/acs.chemmater.0c01666.

(101) Inagaki, M.; Toyoda, M.; Soneda, Y.; Morishita, T. Nitrogen-Doped Carbon Materials. *Carbon*. Elsevier Ltd June 1, 2018, pp 104–140. https://doi.org/10.1016/j.carbon.2018.02.024.

(102) Qiang, Z.; Xia, Y.; Xia, X.; Vogt, B. D. Generalized Synthesis of a Family of Highly Heteroatom-Doped Ordered Mesoporous Carbons. *Chemistry of Materials* **2017**, *29* (23). https://doi.org/10.1021/acs.chemmater.7b04061.

(103) Deng, D.; Pan, X.; Yu, L.; Cui, Y.; Jiang, Y.; Qi, J.; Li, W. X.; Fu, Q.; Ma, X.; Xue, Q.; Sun, G.; Bao, X. Toward N-Doped Graphene via Solvothermal Synthesis. *Chemistry of Materials* **2011**, *23* (5). https://doi.org/10.1021/cm102666r.

(104) Cao, Y.; Mao, S.; Li, M.; Chen, Y.; Wang, Y. Metal/Porous Carbon Composites for Heterogeneous Catalysis: Old Catalysts with Improved Performance Promoted by N-Doping. *ACS Catalysis*. 2017. https://doi.org/10.1021/acscatal.7b02335.

(105) Wang, X. Y.; Yao, X.; Narita, A.; Müllen, K. Heteroatom-Doped Nanographenes with Structural Precision. *Acc Chem Res* **2019**, *52* (9). https://doi.org/10.1021/acs.accounts.9b00322.

(106) Schiros, T.; Nordlund, D.; Pálová, L.; Prezzi, D.; Zhao, L.; Kim, K. S.; Wurstbauer, U.; Gutiérrez, C.; Delongchamp, D.; Jaye, C.; Fischer, D.; Ogasawara, H.; Pettersson, L. G. M.; Reichman, D. R.; Kim, P.; Hybertsen, M. S.; Pasupathy, A. N. Connecting Dopant Bond Type

with Electronic Structure in N-Doped Graphene. *Nano Lett* **2012**, *12* (8). https://doi.org/10.1021/nl301409h.

(107) Luo, W.; Wang, B.; Heron, C. G.; Allen, M. J.; Morre, J.; Maier, C. S.; Stickle, W. F.; Ji, X. Pyrolysis of Cellulose under Ammonia Leads to Nitrogen-Doped Nanoporous Carbon Generated through Methane Formation. *Nano Lett* **2014**, *14* (4). https://doi.org/10.1021/nl500859p.

(108) Yang, H.; Ye, S.; Zhou, J.; Liang, T. Biomass-Derived Porous Carbon Materials for Supercapacitor. *Frontiers in Chemistry*. 2019. https://doi.org/10.3389/fchem.2019.00274.

(109) Zhang, Z.; Yu, L.; Tu, Y.; Chen, R.; Wu, L.; Zhu, J.; Deng, D. Unveiling the Active Site of Metal-Free Nitrogen-Doped Carbon for Electrocatalytic Carbon Dioxide Reduction. *Cell Rep Phys Sci* **2020**, *1* (8). https://doi.org/10.1016/j.xcrp.2020.100145.

(110) Wang, H.; Jia, J.; Song, P.; Wang, Q.; Li, D.; Min, S.; Qian, C.; Wang, L.; Li, Y. F.; Ma, C.; Wu, T.; Yuan, J.; Antonietti, M.; Ozin, G. A. Efficient Electrocatalytic Reduction of CO2 by Nitrogen-Doped Nanoporous Carbon/Carbon Nanotube Membranes: A Step Towards the Electrochemical CO2 Refinery. *Angewandte Chemie - International Edition* **2017**, *56* (27). https://doi.org/10.1002/anie.201703720.

(111) Gong, K.; Du, F.; Xia, Z.; Durstock, M.; Dai, L. Nitrogen-Doped Carbon Nanotube Arrays with High Electrocatalytic Activity for Oxygen Reduction. *Science (1979)* **2009**, *323* (5915). https://doi.org/10.1126/science.1168049.

(112) Sharma, P. P.; Wu, J.; Yadav, R. M.; Liu, M.; Wright, C. J.; Tiwary, C. S.; Yakobson, B. I.; Lou, J.; Ajayan, P. M.; Zhou, X. D. Nitrogen-Doped Carbon Nanotube Arrays for High-Efficiency Electrochemical Reduction of CO2: On the Understanding of Defects, Defect Density, and Selectivity. *Angewandte Chemie - International Edition* **2015**, *54* (46). https://doi.org/10.1002/anie.201506062.

(113) Ferrari, A. C. Raman Spectroscopy of Graphene and Graphite: Disorder, Electron-Phonon Coupling, Doping and Nonadiabatic Effects. *Solid State Commun* **2007**, *143* (1–2). https://doi.org/10.1016/j.ssc.2007.03.052.

(114) Song, Y.; Liu, G.; Yuan, Z. Y. N-, P- and B-Doped Mesoporous Carbons for Direct Dehydrogenation of Propane. *RSC Adv* **2016**, *6* (97). https://doi.org/10.1039/c6ra20726j.

(115) Kelemen, S. R.; Afeworki, M.; Gorbaty, M. L.; Kwiatek, P. J.; Solum, M. S.; Hu, J. Z.; Pugmire, R. J. XPS and 15N NMR Study of Nitrogen Forms in Carbonaceous Solids. *Energy and Fuels* **2002**, *16* (6). https://doi.org/10.1021/ef0200828.

(116) Kuroki, S.; Hosaka, Y.; Yamauchi, C. A Solid-State NMR Study of the Carbonization of Polyaniline. *Carbon N Y* **2013**, *55*. https://doi.org/10.1016/j.carbon.2012.12.022.

(117) Wu, G.; Santandreu, A.; Kellogg, W.; Gupta, S.; Ogoke, O.; Zhang, H.; Wang, H. L.; Dai, L. Carbon Nanocomposite Catalysts for Oxygen Reduction and Evolution Reactions: From Nitrogen Doping to Transition-Metal Addition. *Nano Energy*. 2016. https://doi.org/10.1016/j.nanoen.2015.12.032.

(118) Sing, K. S. W.; Everett, D. H.; Haul, R. A. W.; Moscou, L.; Pierotti, R. A.; Rouquerol, J.; Siemieniewska, T. Reporting Physisorption Data for Gas/Solid Systems with Special Reference to the Determination of Surface Area and Porosity. *Pure and Applied Chemistry* **1985**, *57* (4). https://doi.org/10.1351/pac198557040603.

(119) Wang, H.; Shao, Y.; Mei, S.; Lu, Y.; Zhang, M.; Sun, J. K.; Matyjaszewski, K.; Antonietti, M.; Yuan, J. Polymer-Derived Heteroatom-Doped Porous Carbon Materials. *Chemical Reviews*. 2020. https://doi.org/10.1021/acs.chemrev.0c00080.

(120) Liu, Y.; Su, Y.; Quan, X.; Fan, X.; Chen, S.; Yu, H.; Zhao, H.; Zhang, Y.; Zhao, J. Facile Ammonia Synthesis from Electrocatalytic N2 Reduction under Ambient Conditions on N-Doped Porous Carbon. *ACS Catal* **2018**, *8* (2). https://doi.org/10.1021/acscatal.7b02165.

(121) Chen, Z.; Chen, J.; Barcaro, G.; Budnyak, T. M.; Rokicińska, A.; Dronskowski, R.; Budnyk, S.; Kuśtrowski, P.; Monti, S.; Slabon, A. Reaction Pathways on N-Substituted Carbon Catalysts during the Electrochemical Reduction of Nitrate to Ammonia. *Catal Sci Technol* **2022**, *12* (11), 3582–3593. https://doi.org/10.1039/d2cy00050d.

(122) Jiang, H.; Gu, J.; Zheng, X.; Liu, M.; Qiu, X.; Wang, L.; Li, W.; Chen, Z.; Ji, X.; Li, J. Defect-Rich and Ultrathin N Doped Carbon Nanosheets as Advanced Trifunctional Metal-Free Electrocatalysts for the ORR, OER and HER. *Energy Environ Sci* **2019**, *12* (1). https://doi.org/10.1039/c8ee03276a.

(123) Zhou, N.; Wang, N.; Wu, Z.; Li, L. Probing Active Sites on Metal-Free, Nitrogen-Doped Carbons for Oxygen Electroreduction: A Review. *Catalysts*. 2018. https://doi.org/10.3390/catal8110509.

(124) Zhang, L.; Ding, L. X.; Chen, G. F.; Yang, X.; Wang, H. Ammonia Synthesis Under Ambient Conditions: Selective Electroreduction of Dinitrogen to Ammonia on Black Phosphorus Nanosheets. *Angewandte Chemie - International Edition* **2019**, *58* (9). https://doi.org/10.1002/anie.201813174.

(125) Budnyak, T. M.; Slabon, A.; Sipponen, M. H. Lignin–Inorganic Interfaces: Chemistry and Applications from Adsorbents to Catalysts and Energy Storage Materials. *ChemSusChem*. 2020. https://doi.org/10.1002/cssc.202000216.

(126) Huang, J.; Shen, J.; Li, S.; Cai, J.; Wang, S.; Lu, Y.; He, J.; Carmalt, C. J.; Parkin, I. P.; Lai, Y. TiO2 Nanotube Arrays Decorated with Au and Bi2S3 Nanoparticles for Efficient Fe3+ Ions Detection and Dye

Photocatalytic Degradation. *J Mater Sci Technol* **2020**, *39*. https://doi.org/10.1016/j.jmst.2019.04.043.

(127) Leung, D. Y. C.; Fu, X.; Wang, C.; Ni, M.; Leung, M. K. H.; Wang, X.; Fu, X. Hydrogen Production over Titania-Based Photocatalysts. *ChemSusChem*. 2010. https://doi.org/10.1002/cssc.201000014.

(128) Cheng, X.; Shang, Y.; Cui, Y.; Shi, R.; Zhu, Y.; Yang, P. Enhanced Photoelectrochemical and Photocatalytic Properties of Anatase-TiO2(B) Nanobelts Decorated with CdS Nanoparticles. *Solid State Sci* **2020**, *99*. https://doi.org/10.1016/j.solidstatesciences.2019.106075.

(129) Zou, R.; Zhang, Z.; Yu, L.; Tian, Q.; Chen, Z.; Hu, J. A General Approach for the Growth of Metal Oxide Nanorod Arrays on Graphene Sheets and Their Applications. *Chemistry - A European Journal* **2011**, *17* (49). https://doi.org/10.1002/chem.201101981.

(130) Nair, S. S.; Chen, J.; Slabon, A.; Mathew, A. P. Converting Cellulose Nanocrystals into Photocatalysts by Functionalisation with Titanium Dioxide Nanorods and Gold Nanocrystals. *RSC Adv* **2020**, *10* (61), 37374–37381. https://doi.org/10.1039/d0ra05961g.

(131) Sharma, P. R.; Sharma, S. K.; Antoine, R.; Hsiao, B. S. Efficient Removal of Arsenic Using Zinc Oxide Nanocrystal-Decorated Regenerated Microfibrillated Cellulose Scaffolds. *ACS Sustain Chem Eng* **2019**, *7* (6). https://doi.org/10.1021/acssuschemeng.8b06356.

(132) Anirudhan, T. S.; Rejeena, S. R. Photocatalytic Degradation of Eosin Yellow Using Poly(Pyrrole-Co-Aniline)-Coated TiO 2 /Nanocellulose Composite under Solar Light Irradiation . *J Mater* **2015**, *2015*. https://doi.org/10.1155/2015/636409.

(133) Zhang, Q.; Zhang, L.; Wu, W.; Xiao, H. Methods and Applications of Nanocellulose Loaded with Inorganic Nanomaterials: A Review. *Carbohydrate Polymers*. 2020. https://doi.org/10.1016/j.carbpol.2019.115454.

(134) Ingram, D. B.; Linic, S. Water Splitting on Composite Plasmonic-Metal/Semiconductor Photoelectrodes: Evidence for Selective Plasmon-Induced Formation of Charge Carriers near the Semiconductor Surface. *J Am Chem Soc* **2011**, *133* (14). https://doi.org/10.1021/ja200086g.

(135) Gellé, A.; Moores, A. Plasmonic Nanoparticles: Photocatalysts with a Bright Future. *Current Opinion in Green and Sustainable Chemistry*. 2019. https://doi.org/10.1016/j.cogsc.2018.10.002.

(136) Plodinec, M.; Grčić, I.; Willinger, M. G.; Hammud, A.; Huang, X.; Panžić, I.; Gajović, A. Black TiO2 Nanotube Arrays Decorated with Ag Nanoparticles for Enhanced Visible-Light Photocatalytic Oxidation of Salicylic Acid. *J Alloys Compd* **2019**, *776*. https://doi.org/10.1016/j.jallcom.2018.10.248.

(137) Shi, H.; Zhang, S.; Zhu, X.; Liu, Y.; Wang, T.; Jiang, T.; Zhang, G.; Duan, H. Uniform Gold-Nanoparticle-Decorated {001}-Faceted

Anatase TiO2 Nanosheets for Enhanced Solar-Light Photocatalytic Reactions. *ACS Appl Mater Interfaces* **2017**, *9* (42). https://doi.org/10.1021/acsami.7b12470.

(138) Duan, H.; Fernández-Domínguez, A. I.; Bosman, M.; Maier, S. A.; Yang, J. K. W. Nanoplasmonics: Classical down to the Nanometer Scale. *Nano Lett* **2012**, *12* (3). https://doi.org/10.1021/nl3001309.

(139) Hu, H.; Duan, H.; Yang, J. K. W.; Shen, Z. X. Plasmon-Modulated Photoluminescence of Individual Gold Nanostructures. *ACS Nano* **2012**, *6* (11). https://doi.org/10.1021/nn3039066.

(140) Tauc, J.; Grigorovici, R.; Vancu, A. Optical Properties and Electronic Structure of Amorphous Germanium. *physica status solidi (b)* **1966**, *15* (2). https://doi.org/10.1002/pssb.19660150224.

(141) Murphy, A. B. Band-Gap Determination from Diffuse Reflectance Measurements of Semiconductor Films, and Application to Photoelectrochemical Water-Splitting. *Solar Energy Materials and Solar Cells* **2007**, *91* (14). https://doi.org/10.1016/j.solmat.2007.05.005.

(142) Ohtani, B. Photocatalysis A to Z-What We Know and What We Do Not Know in a Scientific Sense. *Journal of Photochemistry and Photobiology C: Photochemistry Reviews*. 2010. https://doi.org/10.1016/j.jphotochemrev.2011.02.001.

(143) Furube, A.; Du, L.; Hara, K.; Katoh, R.; Tachiya, M. Ultrafast Plasmon-Induced Electron Transfer from Gold Nanodots into TiO2 Nanoparticles. *J Am Chem Soc* **2007**, *129* (48). https://doi.org/10.1021/ja076134v.

(144) Shi, H.; Wang, X.; Zheng, M.; Wu, X.; Chen, Y.; Yang, Z.; Zhang, G.; Duan, H. Hot-Electrons Mediated Efficient Visible-Light Photocatalysis of Hierarchical Black Au–TiO2 Nanorod Arrays on Flexible Substrate. *Adv Mater Interfaces* **2016**, *3* (22). https://doi.org/10.1002/admi.201600588.

(145) Sułek, A.; Pucelik, B.; Kuncewicz, J.; Dubin, G.; Dąbrowski, J. M. Sensitization of TiO2 by Halogenated Porphyrin Derivatives for Visible Light Biomedical and Environmental Photocatalysis. *Catal Today* **2019**, *335*. https://doi.org/10.1016/j.cattod.2019.02.070.

(146) Li, B.; Hao, Y.; Shao, X.; Tang, H.; Wang, T.; Zhu, J.; Yan, S. Synthesis of Hierarchically Porous Metal Oxides and Au/TiO2 Nanohybrids for Photodegradation of Organic Dye and Catalytic Reduction of 4-Nitrophenol. *J Catal* **2015**, *329*. https://doi.org/10.1016/j.jcat.2015.05.015.

(147) Ansari, S. A.; Khan, M. M.; Ansari, M. O.; Cho, M. H. Gold Nanoparticles-Sensitized Wide and Narrow Band Gap TiO2 for Visible Light Applications: A Comparative Study. *New Journal of Chemistry* **2015**, *39* (6). https://doi.org/10.1039/c5nj00556f.

(148) Yin, M.; Li, Z.; Kou, J.; Zou, Z. Mechanism Investigation of Visible Light-Induced Degradation in a Heterogeneous TiO2/Eosin Y/Rhodamine B System. *Environ Sci Technol* **2009**, *43* (21). https://doi.org/10.1021/es902011h.

(149) Xu, J.; Mao, Y. G.; Liu, T.; Peng, Y. Synthesis of a Novel One-Dimensional BiOBr-Bi4O5Br2 Heterostructure with a High Quality Interface and Its Enhanced Visible-Light Photocatalytic Activity. *CrystEngComm* **2018**, *20* (16). https://doi.org/10.1039/c8ce00157j.

(150) Liu, D.; Yao, W.; Wang, J.; Liu, Y.; Zhang, M.; Zhu, Y. Enhanced Visible Light Photocatalytic Performance of a Novel Heterostructured Bi4O5Br2/Bi24O31Br10/Bi2SiO5 Photocatalyst. *Appl Catal B* **2015**, *172–173*. https://doi.org/10.1016/j.apcatb.2015.01.037.

(151) Alansi, A. M.; Al-Qunaibit, M.; Alade, I. O.; Qahtan, T. F.; Saleh, T. A. Visible-Light Responsive BiOBr Nanoparticles Loaded on Reduced Graphene Oxide for Photocatalytic Degradation of Dye. *J Mol Liq* **2018**, *253*. https://doi.org/10.1016/j.molliq.2018.01.034.

(152) Ao, Y.; Wang, K.; Wang, P.; Wang, C.; Hou, J. Synthesis of Novel 2D-2D p-n Heterojunction BiOBr/La2Ti2O7 Composite Photocatalyst with Enhanced Photocatalytic Performance under Both UV and Visible Light Irradiation. *Appl Catal B* **2016**, *194*. https://doi.org/10.1016/j.apcatb.2016.04.050.

(153) Huo, Y.; Zhang, J.; Miao, M.; Jin, Y. Solvothermal Synthesis of Flower-like BiOBr Microspheres with Highly Visible-Light Photocatalytic Performances. *Appl Catal B* **2012**, *111–112*. https://doi.org/10.1016/j.apcatb.2011.10.016.

(154) Ahmad, A. Synthesis and Evaluation of Photocatalytic Properties of BiOBr for Wastewater Treatment Applications By. *Tesis doctoral, Universidad de Ottawa* **2013**.

(155) Davi, M.; Schrader, F.; Scholz, T.; Ma, Z.; Rokicinska, A.; Dronskowski, R.; Kustrowski, P.; Slabon, A. SrTaO2N Nanowire Photoanode Modified with a Ferrihydrite Hole-Storage Layer for Photoelectrochemical Water Oxidation. *ACS Appl Nano Mater* **2018**, *1* (2). https://doi.org/10.1021/acsanm.7b00269.

(156) Deng, J.; Su, Y.; Liu, D.; Yang, P.; Liu, B.; Liu, C. Nanowire Photoelectrochemistry. *Chemical Reviews*. 2019. https://doi.org/10.1021/acs.chemrev.9b00232.

(157) Ma, Z.; Konze, P.; Küpers, M.; Wiemer, K.; Hoffzimmer, D.; Neumann, S.; Kunz, S.; Simon, U.; Dronskowski, R.; Slabon, A. Elucidation of the Active Sites for Monodisperse FePt and Pt Nanocrystal Catalysts for P-WSe2Photocathodes. *Journal of Physical Chemistry C* **2020**, *124* (22). https://doi.org/10.1021/acs.jpcc.0c01288.

(158) Lu, C.; Jothi, P. R.; Thersleff, T.; Budnyak, T. M.; Rokicinska, A.; Yubuta, K.; Dronskowski, R.; Kuśtrowski, P.; Fokwa, B. P. T.; Slabon, A. Nanostructured Core-Shell Metal Borides-Oxides as Highly

Efficient Electrocatalysts for Photoelectrochemical Water Oxidation. *Nanoscale* **2020**, *12* (5). https://doi.org/10.1039/c9nr09818f.

(159) Lu, C.; Ma, Z.; Jäger, J.; Budnyak, T. M.; Dronskowski, R.; Rokicińska, A.; Kuśtrowski, P.; Pammer, F.; Slabon, A. NiO/Poly(4-Alkylthiazole) Hybrid Interface for Promoting Spatial Charge Separation in Photoelectrochemical Water Reduction. *ACS Appl Mater Interfaces* **2020**, *12* (26). https://doi.org/10.1021/acsami.0c03975.

(160) Mao, D.; Ding, S.; Meng, L.; Dai, Y.; Sun, C.; Yang, S.; He, H. One-Pot Microemulsion-Mediated Synthesis of Bi-Rich Bi4O5Br2 with Controllable Morphologies and Excellent Visible-Light Photocatalytic Removal of Pollutants. *Appl Catal B* **2017**, *207*. https://doi.org/10.1016/j.apcatb.2017.02.010.

(161) Di, J.; Ji, M.; Xia, J.; Li, X.; Fan, W.; Zhang, Q.; Li, H. Bi4O5Br2 Ultrasmall Nanosheets in Situ Strong Coupling to MWCNT and Improved Photocatalytic Activity for Tetracycline Hydrochloride Degradation. *J Mol Catal A Chem* **2016**, *424*. https://doi.org/10.1016/j.molcata.2016.08.029.

(162) Su, X.; Wu, D. Facile Construction of the Phase Junction of BiOBr and Bi4O5Br2 Nanoplates for Ciprofloxacin Photodegradation. *Mater Sci Semicond Process* **2018**, *80*. https://doi.org/10.1016/j.mssp.2018.02.034.

(163) Li, R.; Xie, F.; Liu, J.; Wang, Y.; Wang, Y.; Zhang, X.; Fan, C. Synthesis of Bi4O5Br2 from Reorganization of BiOBr and Its Excellent Visible Light Photocatalytic Activity. *Dalton Transactions* **2016**, *45* (22). https://doi.org/10.1039/c6dt00997b.

(164) Di, J.; Xia, J.; Ji, M.; Yin, S.; Li, H.; Xu, H.; Zhang, Q.; Li, H. Controllable Synthesis of Bi4O5Br2 Ultrathin Nanosheets for Photocatalytic Removal of Ciprofloxacin and Mechanism Insight. *J Mater Chem A Mater* **2015**, *3* (29). https://doi.org/10.1039/c5ta02388b.